DECLARATION

I hereby declare that the matter embodied in the thesis entitled "**Trends in Activity and Selectivity in Catalytic Energy Conversion Processes : A First Principles Study**" is the result of investigations carried out by me at the New Chemistry Unit, Jawaharlal Nehru Centre for Advanced Scientific Research, Bangalore, India under the supervision of Prof. Swapan K. Pati and that it has not been submitted elsewhere for the award of any degree or diploma.

In keeping with the general practice in reporting scientific observations, due acknowledgement has been made whenever the work described is based on the findings of other investigators.

Pallavi Bothra

CERTIFICATE

I hereby certify that the matter embodied in this thesis entitled "**Trends in Activity and Selectivity in Catalytic Energy Conversion Processes : A First Principles Study**" has been carried out by Ms. Pallavi Bothra at the New Chemistry Unit, Jawaharlal Nehru Centre for Advanced Scientific Research, Bangalore, India under my supervision and that it has not been submitted elsewhere for the award of any degree or diploma.

Prof. Swapan K. Pati
(Research Supervisor)

Acknowledgements

First, I would like to thank my research supervisor, Prof. Swapan K. Pati. I am thankful for his aspiring guidance, invaluably constructive criticism and friendly advice during my research life. I am sincerely grateful to him for sharing his illuminating views on a number of issues related to the research. Thank you Sir!

I must thank Anusooya Ma'am and Sohan for their love and affection.

I would like to thank my collaborators for fruitful discussions, Prof. Xiao Cheng Zeng, Prof. Michail Stamatakis, Lei Li, Prof. Sebastian Peter, Dr. Mohnish Pandey, Rajkumar Jana and Dr. Sumanta Sarkar.

I thank all my course instructors in JNCASR for the useful courses.

I would like to acknowledge all my past and present lab-mates Dr. Sudipta Dutta, Dr. Sasmita Mohakud, Alex, Dr. Siam, Dr. Arun, Dr. Prakash, Ershaad, Dr. Madhuri, Dibyajyoti, Somananda, Swastika, Arkamita, Bradraj, Asvini, Shubhajit, Abhiroop, Dr. Sharma, Silvia, Nisheal and Neha.

I would also like to thank all the visiting students, Francesco, Francesca, Nabanita, Cristina, Divya, Anisha and Elizabeth for their company.

I will always be indebted to Mighfar Bhaiya, Sudeshna, Vasudevan, Sananda di and Nisha for all the academic helps.

I am thankful to all the administrative, technical, security, Complab, TUE-CMS and Dhanvantari staffs who try their best to make our life smooth at the campus.

Finally and most importantly, I would like to thank my family for their constant support.

Synopsis

There are seven chapters in this thesis. In the introduction (first) chapter, we have briefly described about recent concerns about global warming, green house gas emission and depletion of fossil fuels, which has created an urge for finding alternative resources. An overview of different possible solutions, namely, renewable, clean and cost-effective energy resources have been discussed. The catalysts used for various energy conversion reactions from both experimental as well as theoretical point of view is depicted. Different pathways, depending upon the activation energy barriers have been reviewed briefly. The theoretical models and computational approaches which we have used extensively in the thesis have been discussed in detail.

In second chapter, we have studied the electrocatalytic activity of $(Pt)_n$ (n = 1, 2, 3, 5, 7, 10 and 12) adsorbed on 2H and 1T MoS_2 monolayers, using first principles density functional theory for oxygen reduction reaction (ORR): $O_2 + 4H^+ + 4e \rightarrow 2H_2O$. We have considered four elementary reactions involved in ORR, within a unified electrochemical thermodynamic framework and the corresponding Gibbs adsorption free energies of the key intermediates (*OOH, *O, *OH) associated with each step have been calculated. The results indicate that the reduction of adsorbed hydroxyl (*OH) to water, ($*OH + H^+ + e \rightarrow H_2O$) is the bottleneck step in the ORR process. The adsorption free energy of *OH (Δ G_{OH*}) is found to be the thermodynamic descriptor. Eventually, the ORR activity has been described as a function of Δ G_{OH*} and that establishes a volcano plot predicting $(Pt)_7$ /2H-MoS_2 as the best ORR catalyst amongst $(Pt)_n/MoS_2$ heterosystems with overpotential value of 0.33 V. We propose a new and promising electrocatalyst towards better activity for ORR with very less amount of Pt loading.

In the third chapter, a comparative study of the electrochemical behaviour of pure and metal doped cobalt oxides, Co_3O_4 and $M_xCo_{3x}O_4$,(M = Fe, Ni, Cu) have been performed in order to elucidate the effect of the cation distribution in the surface of crystal lattice. We have studied the oxygen evolution reaction (OER) on these surfaces and the substantial work has been targeted to understand the relation between structure, mechanism, and activity. The activity of the substituted spinels increases relative to that of pure Co_3O_4, with considerable decrease in overpotential values. This agrees well with the experimental findings. It has also been found that catalytic activity directly depends on the dopant concentration. We find that 25 % substitution of Cu in Co_3O_4 has highest electrocatalytic activity with a reduced overpotential value of 0.41 V for OER.

In the third chapter, a comparative study of the electrochemical behaviour of pure and metal doped cobalt oxides, Co_3O_4 and $M_xCo_{3x}O_4$,(M = Fe, Ni, Cu) have been performed in order to elucidate the effect of the cation distribution in the surface of crystal lattice. We have studied the oxygen evolution reaction (OER) on these surfaces and the substantial work has been targeted to understand the relation between structure, mechanism, and activity. The activity of the substituted spinels increases relative to that of pure Co_3O_4, with considerable decrease in overpotential values. This agrees well with the experimental findings. It has also been found that catalytic activity directly depends on the dopant concentration. We find that 25 % substitution of Cu in Co_3O_4 has highest electrocatalytic activity with a reduced overpotential value of 0.41 V for OER.

We have studied the complete hydrogenation mechanisms of CO_2 on Ni(110) surface using density functional theory in Chapter four. The possible hydrogenation mechanism to form product methane from the stable adsorptionco-adsorption intermediates of CO_2 and H_2 on Ni(110) surface have been explored. Our computations clearly elucidate the mechanism for the formation of methyl, methoxy and methane moieties from carbon dioxide on the nickel surface. Moreover, our studies clearly show that the methane formation via hydroxyl intermediate requires a lower energy barrier than via carbon monoxide and formate intermediates on the Ni(110) surface.

In chapter five, we have studied steam methane reforming reaction (SMR) on pure Ni (110) and single Rh layer deposited Ni (110) surface, using first-principles density functional theory and micro-kinetic modelling. For the preliminary study, we have investigated the complete dehydrogenation of methane by means of gradient-corrected periodic density functional theory. A detailed kinetic study, based on the analysis of the optimal reaction pathway for the transformation of CH_4 to C and H through four elementary steps ($CH_4 \rightarrow CH_3 + H$; $CH_3 \rightarrow CH_2 + H$; $CH_2 \rightarrow CH + H$; $CH \rightarrow C + H$) is presented for pure Ni (110) and Rh/Ni (110) surfaces. Through systematic examination of adsorbed geometries and transition states, we show that single layer deposition of Rh on Ni(110) surface has a striking influence on lowering the activation energy barrier of the dehydrogenation reaction. Moreover, it is found that a pure Ni (110) surface has a tendency for coke (C) deposition on the catalytic surface during the methane dissociation reaction which decreases the stability of the catalyst. However, the deposition of carbon is largely suppressed by the addition of a Rh overlayer on the pure Ni (110) surface. Considering the balance in both the catalytic activity as well as the catalyst stability, we propose that the Rh/Ni (110) surface possesses much improved catalytic property compared to pure Ni(110) and pure Rh(110) surfaces. Further, we have carried out the micro-kinetic modelling on SMR reactions and found that conversion of CH_4 is higher on Rh/Ni(110) surface (32%) in comparison to pure Ni(110) surface (27%).

In Chapter six, we thoroughly investigate the formation mechanism of the methanol from the hydrogenation of CO_2 on Ir clusters (Ir_7, Ir_{13} and Ir_{55}) using density functional theory (DFT). Our theoretical results suggest that the methanol synthesis follows the formic acid ($HCOOH^*$) pathway which involves the direct hydrogenation of CO_2 via Langmuir-Hinshelwood (L-H) mechanism and that eventually forms $HCO^* + OH^*$ via C-O bond cleavage. The sequential hydrogenation of HCO^* results in the final product as follows, $HCO^* \rightarrow H_2CO^* \rightarrow H_2COH^* \rightarrow CH_3OH$, with feasible activation energy barriers. Notably, the barrier of the final step via methoxy intermediate (H_3CO^*

+ H^* CH_3OH) can be reduced by 0.6 eV in the presence of water, where the reduction takes place via water mediated proton transfer to the surface methoxy, ($H_3CO^* + H_2O^* \rightarrow CH_3OH + OH^*$). Moreover, our study strongly recommends that the transformation of CO_2 to CH_3OH on Ir clusters is highly influenced by the size of the cluster. Interestingly, Ir_7 cluster is expected to be the most potential candidate with more number of active sites which scales down the barrier height for the elementary reaction steps of CO_2 to CH_3OH conversion in comparison to Ir_{13} and Ir_{55} clusters.

Chapter seven has two parts, part(a) and part(b). In part(a), we have studied the formation of formic acid (HCOOH) from CO_2 on Ni(100) surface. The detailed mechanism for these reactions have been clearly demonstrated. We find that formate pathway is more energetically feasible than carboxylic pathway. In part(b), the reverse reaction (i.e., CO_2 to HCOOH) on bare $AgPd_{13}$, graphene supported $AgPd_{13}$ and BN supported $AgPd_{13}$ cluster has been investigated using density functional theory. We find that HCOOH to CO_2 formation is kinetically more favoured on BN supported $AgPd_{13}$ cluster in comparison to other systems.

List of Publications

Publications Related to the Thesis Work

1. *"Methane formation from the hydrogenation of carbon dioxide on Ni(110) surface a density functional theoretical study"*
   Pallavi Bothra, Ganga Periyasamy and Swapan K. Pati,
   Phys. Chem. Chem. Phys, **15**, 5701- 5706 (2013).

2. *"Improved catalytic activity of rhodium monolayer modified nickel (110) surface for the methane dehydrogenation reaction: a first-principles study"*
   Pallavi Bothra and Swapan K. Pati,
   Nanoscale, **6**, 6738 - 6744 (2014).

3. *"Towards Methanol Synthesis from CO_2 and H_2 on Iridium clusters- A Theoretical Study "*
   Pallavi Bothra, Lei Li, Xiao Cheng Zeng and Swapan K. Pati, *(Submitted)*

4. *"Size-selective Electrocatalytic Activity of $(\mathrm{Pt})_n/MoS_2$ for Oxygen Reduction Reaction"*
   Pallavi Bothra, *Mohnish Pandey and Swapan K. Pati (Submitted)*

5. *"Effect of Doping on the Electrocatalytic Activity of Co_3O_4 for Water Oxidation Reaction"*
Pallavi Bothra *and Swapan K. Pati (Submitted)*

6. *"Effect of Support for the Conversion of HCOOH to CO_2 on $AgPd_{13}$ cluster"*
Pallavi Bothra *and Swapan K. Pati (Submitted)*

7. *"Conversion of CO_2 to HCOOH on Ni(100) Surface"*
Pallavi Bothra *and Swapan K. Pati (Submitted)*

Other Publications by the Author

8. *"Phase Transition of MoS_2 Bilayer Structures"*
Mohnish Pandey, **Pallavi Bothra** *and Swapan K. Pati,*
J. Phys. Chem. C (Just accepted).

9. *"Electrochemically Dealloyed $PdCu_3$ Nanoparticle with Enhanced Activity Equivalent to Pt for Hydrogen Evolution Reaction"*
R. Jana, A. Bhim, **Pallavi Bothra** *, Swapan K. Pati and S. C. Peter (Submitted).*

10. *"Shape controlled synthesis of supportless $PdCu_3$ nanoparticles as Pt-free catalyst for the oxygen reduction reaction with activity and durability better than commercial platinum on carbon."*
R. Jana, A. Bhim, V. G. Anju, **P. Bothra**, *B. Joseph, M. Balasubramnian, S. Sampath, S. Pati, S. C. Peter (Submitted)*

11. *"The role of metal deficiency in Ni_2Sn as non-noble metal catalyst with enhanced activity in electrochemical hydrogen evolution reaction."*
R. Jana, S. Sarkar, D. Mumbaraddi, A. P. Chandran, **P. Bothra**, *S. Pati, S. C. Peter (Submitted)*

12. *"Effect of crystallographic facets in $PdCu_3$ nanoparticles towards enhanced catalytic activity and durability for ethanol electro-oxidation."*
R. Jana, A. Bhim, **P. Bothra***, S. Pati, S. C. Peter (Submitted)*

List of Figures

List of Tables

Contents

Chapter 1

Introduction

Contents

1.1 Energy and Environment

The continuous progress in the field of science and technology have given human race to a convenient and modern lifestyle. Towards the end of the last century, almost every other region on the earth began experiencing industrialization to some extent or the other to come first in the race of modern civilization. As a consequence, energy has become the most essential ingredient for the existence of life in a myriad of ways. The need for energy is ever-increasing and to satisfy our appetite for better life, fossil fuels (coal, natural gas, and oil) stand by us for more than a century now. More than three quarters of the world's energy consumption comes directly from burning of fossil fuels. As of 2013, the primary energy supply of the world comes from following three major energy sources (Fig. 1.1); oil (33%), coal (30%) and natural gas (24%) with a combined fuel share of 87%. In fact, all our modern transportation and industrial development processes have been made possible due to the discovery and extraction of fossil fuels. For example, (i) Coal supplies the majority of power generation. Electricity is one of the essential necessity for any nations economy and most of the nations are still entirely dependent on coal based power plants to meet their energy demands. (ii) Oil continues to be the king of transportation. Petroleum is widely used for powering the internal combustion engines inside vehicles either in the form of petrol or in the form of gasoline. Even, many food and packaging industries are also dependent on

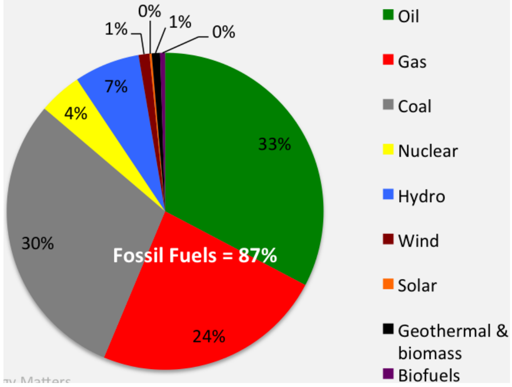

Figure 1.1: Fuel shares of total primary energy supply (image taken from:http://euanmearns.com/global-energy-trends-bp-statistical-review-2015/)

it. (iii) Natural gas is probably the best known source of energy at homes. In addition, from fabric industries to fertilizer industries, all make use of this economical form of power, obtained from natural gas.

It is clear that our energy supply heavily depends on fossil fuels, but these are finite and non-renewable energy sources. The massive demand for energy has resulted in depletion of finite deposits of fossil fuels millions of times faster than they are formed. This gives rise to a situation that cannot continue for long time and eventually, the world is heading towards a large global energy crisis at an alarming fast rate. As of International Energy Outlook 2013 (IEO2013), with societys current level of energy consumption, total energy consumption of the world is estimated to increase by 56%, i.e., from 524 quadrillion Btu (Britsh thermal unit) in 2010 to 820 quadrillion Btu, by year 2040. Moreover, the challenge to deal with the limited resources of fossil fuels is accompanied by a major environmental threat, which is manifested all over the globe now, called global warming induced by the greenhouse gas effect. Since the fossil fuels are made up of hydrogen and carbon; hence while burning of these fuels, the carbon combines with oxygen to create carbon dioxide, a major greenhouse gas. In fact, the amount of carbon dioxide emitted depends on the carbon content of the fuel; for example, for each unit of energy produced, natural gas emits about half and petroleum fuels about three-quarters of the carbon dioxide produced by coal.

CO_2 is known as the fourth abundant gas naturally present in the atmosphere of the earth. However, there is continuous rise in the concentration of CO_2 in the atmosphere and today there is an excess of 1 teraton of carbon dioxide in the atmosphere. Furthermore, there is inclusion of 24 gigaton of carbon dioxide into the atmosphere annually, which is man-made and unlikely to reduce in significant amount in the next decades. The natural carbon cycle equilibrates the carbon flow between the atmosphere and oceans and the fixation of CO_2 by plants and microorganisms; this is nicely balanced by emission of CO_2 from plants, animals and volcanoes. But, as of current research, there is an excess of approximately 3.9 % CO_2 with respect to the natural carbon cycle. Such excess of carbon dioxide is not balanced over the period of time and, consequently, there is a steady increase in concentration of CO_2 in the atmosphere over the last few hundreds of years. Since the industrial revolution, the concentration of CO_2 has been increased by 40 %. According to The IPCC (Intergovernmental Panel on Climate Change) prediction, by the year 2100, the atmosphere may include up to 570 ppm of CO_2, resulting a rise of mean global temperature of around 1.9C. Furthermore, it is also predicted that this will lead to an increase in mean sea level of up to 38 cm, increased desert formation and the extinction of various species. Fig. 1.2 shows the projected atmospheric greenhouse gas concentration as a function of the years (2000-2100). In a nutshell,

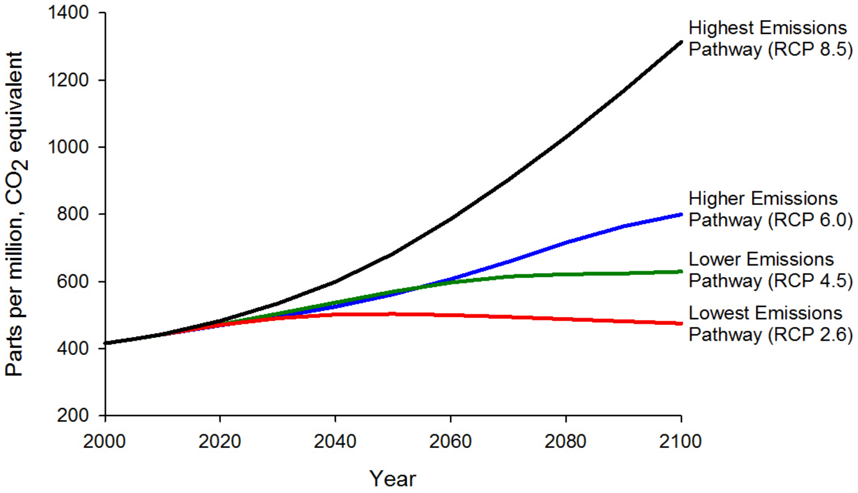

Figure 1.2: Projected Atmospheric Greenhouse Gas Concentration (taken from:http://www.iiasa.ac.at/web-apps/tnt/RcpDb)

the crux of our problem is the increase in the use of fossil fuels. This clearly calls for replacement of fossil fuels with alternative new energy strategy that could be economically and environmentally sustainable as well as that meets the demands for wide range of services (industry, transportation, household).

1.2 Renewable Energy Resources

Renewable energy is generally defined as energy that comes from resources which are naturally replenished on a human timescale. For example, the electric energy that is generated from the sun (solar), the wind, waste (biomass), the earth (geothermal), hydrogen energy etc. are, in general, considered to be renewable energy. In contrast to fossil fuels, they restore themselves more rapidly than they are consumed. Most importantly, these sources are available free of cost and do not tax the environment for their usage. So, power generation through renewable sources of energy is clean and green.

1.2.1 Solar Energy

Solar Energy is the energy which is produced by the sun in the form of heat and light. It is one of the most renewable and clean source of energy. Solar radiation gets converted into DC electricity directly through Solar Photovoltaic (SPV) cells.

1.2.2 Wind Energy

Wind energy is one of the most clean and effective alternative source of energy in areas where the velocity of wind flow is high. The power of the wind is harnessed to propel the blades of wind turbine attached to an electric generator which forms electric current to generate wind energy.

1.2.3 Biomass Energy

This is an environmental friendly way of production of energy in which biological mass is recycled and re-used. Since, the biomass will keep generating and decomposing as part of the natural biological cycle, hence, it can be considered as a renewable source of energy.

1.2.4 Geothermal Energy

Similar to the other alternative energy sources, geothermal energy source is free of cost. This energy is tapped from the heat inside the earth. If power generation system in placed properly, no harmful by-products are produced.

1.2.5 Hydrogen Energy

One of the most promising alternative to fossil fuels is hydrogen, which is completely renewable and is available in abundant amount. More importantly, hydrogen, when burnt does not leave any toxic emissions in the atmosphere, hence it is clean energy. It has the highest energy content by weight amongst all the common fuels. 2.2 pounds (1 kilogram) of hydrogen gas contains almost similar energy as in 1 gallon of gasoline. So, hydrogen is considered as a highly efficient and low polluting fuel that can be employed for transportation, heating, and power generation in places where it is difficult to get electricity. Renewable energy sources, like the sun and wind, may not provide energy all the time. On the other hand, if properly maintained, hydrogen can be stored and used at all the time. That is why, hydrogen economy has turned out to be major interest nowadays.

1.2.5.1 How Hydrogen Produces Energy

Hydrogen is considered as a secondary source of energy, commonly known as an energy carrier. It has been proposed that fuel cells can be one of the good ways in utilizing hydrogen as an energy carrier. Hydrogen fuel cell is promising technology which combines hydrogen and oxygen to produce electricity, heat, and water. It converts the energy produced by a chemical reaction into usable electric power. Typical reactants used in a fuel cell are hydrogen on the anode side and oxygen or air on the cathode side. Hydrogen-powered fuel cells are not only pollution-free, but a two to three fold more efficient, in comparison to traditional combustion technologies. Fuel cells can power almost any portable devices which normally use batteries. Even, it can also power transportation such as vehicles, trucks, buses, and marine vessels, as well as supply auxiliary power to traditional transportation technologies. Accordingly, hydrogen can play a very important role in the future by replacing the imported petroleum, we currently use in our daily lives.

However, one of the major technical problem with fuel cell is sluggish kinetics of cathode reaction (oxygen reduction reaction) which eventually reduces the complete efficiency of fuel cell. To expedite the rate of the reaction, suitable catalyst is needed. The other challenge of using hydrogen as a fuel also comes from being able to efficiently extract hydrogen from these compounds.

1.2.5.2 How Hydrogen can be Produced

Since hydrogen does not exist on earth as a gas, it must be separated from other compounds. Hydrogen is found to be locked up in enormous quantities in water (H_2O), hydrocarbons (such as methane, CH_4), and other organic matter. Two of the most common methods used for the production of hydrogen are (i) electrolysis or water splitting and (ii) extracting it from hydrogen rich organic compounds.

(i) Electrolysis involves passing an electric current through water to separate it into its basic elements, hydrogen and oxygen. Hydrogen is then collected at the negatively charged cathode and oxygen at the positive anode. Hydrogen produced by electrolysis is extremely pure, and results in no emissions since electricity from renewable energy sources can be used. An electrolyser cell is much like a fuel cell, but run in reverse direction, i.e., it uses electricity instead of generating it. Hence, fuel cells and electrolysers are complementary technologies. In contrast to the fuel cell, the efficiency of an electrolyzer is retarded by slow kinetics of anode reaction, i.e., oxygen evolution reaction. However, in the presence of an appropriate catalyst, the corresponding reaction can occur at an appreciable rate.

(ii) Besides water, hydrogen can also be found in many organic compounds, notably the hydrocarbons that make up many of fuels, such as natural gas, methane, formic acid etc. Hydrogen can be produced in a number of ways from these hydrogen rich sources. Among many pathways, steam methane reforming reaction is one of the most efficient route for production of H_2 from methane; hence plays a key role in hydrogen generation process. In addition, H_2 stored in formic acid can be acquired via dehydrogenation reaction on a suitable catalyst and recently has drawn the attention of many industries, seeking for pure hydrogen. In terms of hydrogen economy, in this thesis, we have searched for the promising catalyst for oxygen reduction reaction, oxygen evolution reaction, steam methane reforming reaction and formic acid decomposition reaction. The associated activity and selectivity trends of the proposed catalysts have been discussed in detail in the corresponding chapters.

1.3 Strategies for Carbon Dioxide Mitigation

In last few decades, there has been growing scientific consensus to design the strategy to level off the atmospheric CO_2 concentration. Nature has its own CO_2 fixation process which is extraordinarily selective in converting CO_2 into organic compounds. However, this natural process is not simply fast enough to cope up with the ever-increasing rate of CO_2 emission in today's industrialized world. Hence, there is an urgent need for finding out an effective solution towards this issue. In principle, there are three major strategies or technological options for mitigation of CO_2:

(i) Carbon-Free and Reduced-Carbon Energy Sources: The first strategy can be addressed by changing in the primary energy source to reduce the amount of CO_2 emitted. The best possible way is to shift towards CO_2 free energy resources such as hydrogen, wind, geothermal or solar which are already discussed in detail in the previous section.

(ii) Capture and Storage: The next strategy involves the development of novel technologies for capture and sequestration of CO_2. However, the capture of carbon dioxide from the power plants or industrial processes is a well established and commercially viable technology. The captured and separated CO_2 can be confined in natural sites such as: aquifers, deep geological cavities, spent oil or gas fields, coal mines or the ocean.

(iii) Usage of CO_2 as Chemical Feedstock by Chemical Transformation: The relatively modern strategy, which deserves research attention, is to utilize CO_2 as a source in the synthesis of chemicals, fuels, intermediates and/or fine chemicals. Interestingly, the chemical transformation of CO_2 for producing chemicals and fuels not only contributes to alleviating global climate changes caused by the increasing CO_2 emissions, but also helps in maintaining the "carbon cycle". Hence, it is one of the most promising strategies which can simultaneously tackle the two major problems of the century, namely, the global warming and fossil fuel depletion, for sustainable development in the future. However, since CO_2 is thermodynamically very stable, that is why, it requires high energy substances to transform it into other chemicals.

In this regard, hydrogenation reaction is found to have promising opportunities towards sustainable development in energy and environment. It is an important representative route amongst all the possible processes for the chemical conversions of CO2. More importantly, as hydrogen is a high energy material and thus, can be used as a very effective reagent for CO_2 transformation during hydrogenation process. The possible ways for the generation of pure hydrogen for chemical recycling of CO_2 has been discussed in the previous section. The major products of CO_2 hydrogenation fall into two categories: fuels and chemicals. The products obtained from CO_2 hydrogenation such as methanol, dimethyl ether (DME), hydrocarbons and formic acid are excellent fuels in internal combustion engines, and also are easy for storage and transportation. Furthermore, methanol and formic acid are raw materials and intermediates, widely used in many chemical industries. There exist several pathways for its activation and conversion to desired chemicals. However, scaling up of the complete CO_2 hydrogenation process to industrial levels demands satisfactory catalysts with desirable cost, activity, selectivity, stability, recovery, reuse, and handling.

1.4 Catalysis

The term ‘Catalysis ’originates from the Greek word loosen. It was first introduced by J.J. Berzelius in 1835. It was used to describe the property of substances which can facilitate chemical reactions without being consumed or reacted during the reaction. Depending on the state of catalyst and reactants and products, catalysis can be classified into two types, homogeneous and heterogeneous catalysis. Homogeneous catalysis involves catalyst in the same phase as reactants and products, whereas in heterogeneous catalysis, the catalysts are present in a different phase from that of the reactant. Though, homogeneous catalysts show desirable activity and selectivity, but the recovery and regeneration are quite troublesome. Alternatively, heterogeneous catalysts are preferable in terms of stability, separation, handling, and reuse, as well as reactor design and that results in lower costs for large-scale productions. These are indeed very vital for the development of future energy technologies. For example, production of transportation fuel, petrochemical products, pollution control, building more efficient batteries or enabling the direct use of sunlight are just some of the fields where heterogeneous catalysis is extensively adopted. This thesis deals with heterogeneous catalysis, where the reactants exist in the gas phase but reacts on the surface of a solid catalyst. Such catalysis depends on adsorption process which is a phenomenon where molecules from the gaseous phase sits onto the solid surface. The fundamental principles behind adsorption originates from the thermodynamic driving force to reduce surface free energy. Strong adsorption involves molecular bond breakage when the new bonds between the reactants and the solid surface are formed. This is called chemisorption, while the opposite, i.e. weaker form of adsorption without any of bond breakage called physisorption.

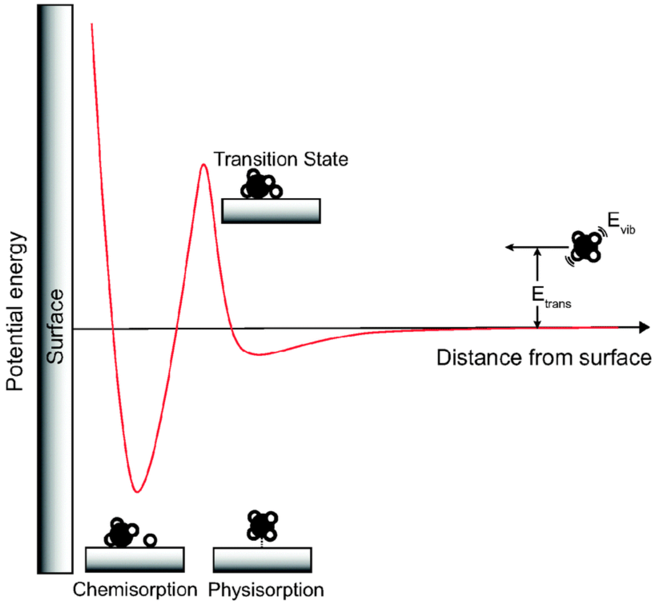

Figure 1.3: Schematic diagram of the potential energy as a function of the distance from the surface (image taken from Ref. [1])

In Fig. 1.3 displays the difference between the two types of adsorption as a plot of the potential energy against the distance from a surface for two atoms and one molecule. As expected, the potential energy for a molecule is zero, far from the surface, as it is not affected by the attractive Van der Waals forces. However, upon approaching the surface, it reaches a minimum due to increased electronic repulsion. In this dwell the molecule is physisorbed on the surface and can diffuse over long distances if the temperature is not too low. If the physisorbed molecule gains enough energy to approach the surface sufficiently close it can, depending on internal bond strength, either dissociate into atoms or chemisorb molecularly. A good catalyst should adsorb the reactant molecules strongly enough for them to react, but not so strongly that the product molecules stick more or less permanently to the surface. The chemical reaction efficiency can be improved by using an appropriate catalyst that lowers the barrier for the reaction (activation energy, Ea).

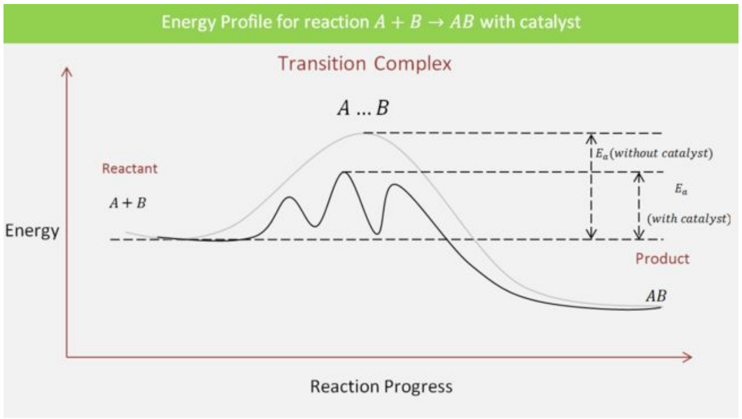

Figure 1.4: Plot of activation energy barrier with and without catalyst. (image taken from (https://brilliant.org/wiki/activation-energy/)

In Fig. 1.4 the activation energy for a gas phase reaction is compared to that of a catalytic reaction. Evidently, the required energy to cross the barrier is lower in the presence of an appropriate catalyst. In general, a catalytic reaction follows a cycle which starts with adsorption of a reactant, followed by a surface diffusion and reaction and consequently desorption of products into the gas phase. The reason behind the surface reaction as being much efficient than a gas phase reaction is that the probability of the adsorbed species to collide while diffusing around onto the catalyst surface (two dimensional) is higher compared to gas molecules free to move in three dimensions. Consequently, the result is production of new molecules that might be either desired products, unwanted products or intermediates.

Recent developments in Density Functional Theory (DFT) calculations can provide atomic-scale insight into the nature of active sites and fundamental understanding of chemical reactions

1.5 Theoretical Formulation

The in-depth understanding of unconventional, surprising properties of materials have been the subject of a great deal of theoretical and numerical investigation. The standard model of physics and chemistry deal with nuclei and electrons which forms many-body problem. The Hamiltonian of this many-body problem can be written as

$$\hat{\mathcal{H}} = -\sum_I \frac{\hbar^2}{2M_I}\nabla_I^2 - \frac{\hbar^2}{2m_e}\sum_i \nabla_i^2 + \frac{1}{2}\sum_{I\neq J}\frac{Z_I Z_J e^2}{|R_I - R_J|} - \sum_{i,I}\frac{Z_I e^2}{r_i - R_I} + \frac{1}{2}\sum_{i\neq j}\frac{e^2}{|r_i - r_j|} \tag{1.1}$$

Where r_i specifies the position of the i^{th} electron having mass m_e and charge e; R_I represents the position of the I^{th} nucleus of mass M_I with atomic number Z_I; $\hbar$ is the universal Planck's constant, and the indices i,j run over all electrons present in the system.

The first two-terms on the right-hand side of eq(1.1) correspond to nuclear and the electrostatic kinetic energies, respectively. The third, fourth and fifth term on the right-hand side represent the nuclear-nuclear repulsion, electron-nuclei attraction and the electron-electron repulsion, respectively.

However, it is easy to write down Hamiltonian as given in eq (1.1), but difficult to solve. For N particle system, the Schrodinger equation corresponding to the Hamiltonian is a partial differential equation in 3N degrees of freedom. For example, to express the wave function on a grid, consisting of 100 points along each spatial direction taking into account two spin states for each electron, huge ($2^{14}100^{3\times16} \sim 10^{100}$) complex numbers are needed.

As a solution of this problem, here comes Density Functional Theory (DFT). It is one of the most popular method which is extensively used in all the branches of science including condensed-matter physics, chemistry, material science, biology for atoms, molecules etc. Realizing complicated nature of the Hamiltonian as given in eq(1.1), the first approximation of DFT is Born-Oppenheimer Approximation.

1.5.1 Born-Oppenheimer Approximation

Born-Oppenheimer approximation, also known as adiabatic approximation shows a way of separating out the nuclear and electronic degrees of motion. Since the mass of nuclei is much heavier than the electrons ($M_I >> m_e$), eventually, nuclei have much smaller velocities compared to electrons. Hence, we can consider nuclei, as effectively stationary in the electronic time scale. As a result, electronic Hamiltonian can be solved using time-independent schrodinger equation for electrons present in this stationary external nuclear potential. Within this approximation, the many-body Hamiltonian in eq(1.1) can now be written as

$$\hat{\mathcal{H}}_e = -\sum_i \frac{\hbar^2}{2m_e}\nabla_i^2 + \frac{1}{2}\sum_{i\neq j}\frac{e^2}{|r_i - r_j|} - \sum_{i,I}\frac{Z_I e^2}{|r_i - R_I|} \tag{1.2}$$

The electronic wave function $\psi(r_i; R_I)$ can be obtained by solving the time-independent schrodinger equation which is given in eq(1.3),

$$\Big[-\sum_i \frac{\hbar^2}{2m_e}\nabla_i^2 + \frac{1}{2}\sum_{i\neq j}\frac{e^2}{|r_i - r_j|} - \sum_{i.I}\frac{Z_I e^2}{|r_i - R_I|}\Big]\Psi(r_i, R_I) = E(R_I)\Psi(r_i, R_I) \tag{1.3}$$

Where $E(R_I)$ represents the set of electronic energy eigenvalues which are the function of nuclear positions. Observe that the first two terms in eq(1.2) and eq(1.3) are only the function of electronic position and basically same for all N-electron system. Thus, if we have the knowledge of external nuclear potential (V_{ext}), it would be sufficient to determine the ground state of many electron system. However, as we have discussed previously, the solution for the wave functions of this many particle equation is turned out to be a impossible task even for a small number of electron system. In DFT, instead of solving many-particle wave function, electronic density is considered as basic variable. This dramatically simplifies the problem. Before we are moving to two basic theorem of DFT, we define electronic density as following way:

$$\hat{n}(r) = \sum_{i=1}^{N} \delta(r - r_i) \tag{1.4}$$

The electronic density can be computed from the many-electron wave function by the following relation,

$$n(r) = \frac{\langle \Psi | n(r) | \Psi \rangle}{\langle \Psi | \Psi \rangle} = \frac{\int dr_1 dr_2 ....dr_N \sum_i^N \delta(r - r_i) |\Psi(r_1, r_2, ..., r_N)|^2}{\int dr_1 dr_2 ....dr_N \sum_i^N |\Psi(r_1, r_2, ..., r_N)|^2} \tag{1.5}$$

Thus one can calculate total energy of the system which can be given as

$$E = \langle \hat{H}_e \rangle = \left\langle -\sum_i \frac{\hbar^2}{2m_e} \nabla_i^2 + \frac{1}{2} \sum_{i \neq j} \frac{e^2}{|r_i - r_j|} + \int de V_{ext}(r) n(r) \right\rangle \tag{1.6}$$

Observe that first term within angular brackets is universal for all eletronic system for a given number of electrons N. Thus, material specific information can be obtained from second term which contains both external potential V_{ext}

and the electronic density n(r). Next, we have given two major theorem of DFT, named as Hohenberg-Kohn Theorems [2, 3].

1.5.2 Hohenberg-Kohn Theorems

Hohenberg-Kohn proposed two theorems based on which DFT is formulated:

1.5.2.1 Theorem-I

'For any system of interacting particles in the presence of an external potential V_{ext}(r), the potential $V_{ext}(r)$ can be uniquely determined, up to an additive constant, by the ground state density n_0(r).'

1.5.2.2 Theorem-II

'A functional which is universal for the energy E[n] in terms of density n(r)can be defined, valid for for any external potential $V_{ext}(r)$. For any particular V_{ext}(r), the exact ground state energy of the system defines the global minimum value for this functional, and the density which minimizes the functional is the exact ground state density n_0(r).'

1.5.3 Approximation for exchange-Correlation functional

The exchange energy is the energy due to fermionic anti-symmetric nature of the wave-function under the exchange of any pair of electrons. The correlation energy can be defined as the difference between the exact total energy and collectively the kinetic, Hartree and exchange energy of the system. In principle, correlation energy takes care of complicated many-body interactions between the electrons. It is important to note that the exact-functional form of the exchange-correlation energy is not known, and hence one has to rely on approximate exchange-correlation functional to calculate various properties of the system. Next, we have described two approximation scheme for exchange-correlation functional.

1.5.3.1 Local density approximation

Within this scheme, the effect of the exchange and correlation is treated locally, such that exchange-correlation term solely depends on density at each point in space and independent of the other points. The exchange-correlation energy density is considered to be similar to that of a homogeneous electron gas.

$$E_{xc}^{LDA}[n] = \int drn(r)\epsilon_{xc}^{hom}(n(r)) \tag{1.7}$$

Where $\epsilon_{xc}^{hom}(n(r))$ defines the exchange-correlation energy density in homogeneous electron gas for density $n(r)$. The average exchange energy density of the homogeneous electron gas can be given as

$$\epsilon_{x}^{hom}(n) = -\frac{3}{4}(\frac{6}{\pi})^{1/3} \tag{1.8}$$

The correlation energy of a homogeneous electron gas was determined by quantum Monte-Carlo simulations [4] and analytical forms were formulated. One of the most commonly used forms were proposed by Perdew and Zunger[5].

Though LDA is a very crude approximation, it works reasonably well for most of the solid system. In general, LDA underestimate certain quantity for lattice parameters.

1.5.4 Generalized Gradient Approximation

Generalized Gradient Approximation(GGA) is an extension of LDA for taking into account inhomogeneous nature of the density in real system including gradient of density as correction factor. Many ways [6–8] were proposed to include the gradient of density. Within GGA scheme, functional form of exchange correlation can be given as

$$E_{xc}^{GGA}[n] = \int drn(r)\epsilon_{xc}([n], |\Delta n(r)|) \tag{1.9}$$

Where $\epsilon_{xc}([n], |\Delta n(r)|)$ corresponds to the exchange-correlation energy per electron which is a function of local density $n(r)$ and also magnitude of the gradient of the density $|\Delta n(r)|$.

Thus exchange correlation potential has the form

$$V_{xc}^{GGA}(r) = \left[\epsilon_{xc} + n\frac{\partial \epsilon_{xc}}{\partial n} - \Delta(n\frac{\partial \epsilon_{xc}}{\partial \Delta n}\right] \tag{1.10}$$

In general, GGA has tendency to underbind. As a result, GGA predicted lattice parameters are too large. However, properties like magnetic moment are estimated better using GGA compared to LDA.

1.6 Basis set

In order to solve the KS equation, the KS orbitals needs to be expanded in terms of suitable choice of basis function. A variety of basis functions are proposed such as plane waves [9], gaussians, Muffin Tin Orbitals, localized atomic orbitals etc. In this thesis, we have mainly used plane wave basis set.

1.7 Force calculation: Hellmann-Feynman Theorem

To obtain optimized geometries of systems, one has to calculate and minimize the forces on each atom present in the system. In this thesis, we have used Hellmann-Feynman (HF) theorem [10] to calculate the forces. According to Hellmann-Feynman (HF) theorem, the force (F_I) on ion I can be calculated as following:

$$
\begin{aligned}
F_I &= -\frac{\partial\langle E(\mathbf{R}_I)\rangle}{\partial \mathbf{R}_I} \\
&= -\frac{\partial}{\partial \mathbf{R}_I}\Big\langle \Psi(R)|H|\Psi(R)\Big\rangle \\
&= -\Big\langle \frac{\partial \Psi}{\partial R_I}|H|\Psi\rangle - \Big\langle \Psi|\frac{\partial H}{\partial R_I}|\Psi\Big\rangle - \langle\psi|H|\frac{\partial \Psi}{\partial R_I}\Big\rangle \\
&= -\Big\langle \Psi|\frac{\partial H}{\partial R_I}|\Psi\Big\rangle - E\Big[\langle\frac{\partial \Psi}{\partial R_I}|\Psi\rangle + \langle\Psi|\frac{\partial \Psi}{\partial R_I}\rangle\Big] \\
&= -\Big\langle \Psi|\frac{\partial H}{\partial R_I}|\Psi\Big\rangle - E\Big[\frac{\partial}{\partial R_I}\langle\Psi|\Psi\rangle\Big] \\
&= -\Big\langle \Psi|\frac{\partial H}{\partial R_I}|\Psi\Big\rangle \qquad (1.11)
\end{aligned}
$$

Where $\Psi(R)$specifies the electronic eigenfunction of Hamiltonian H and $\langle\Psi|\Psi\rangle = 1$. The main advantage of HF theorem is that force can be calculated from a DFT calculation at one given configuration alone. Hence, one does not need to calculate the total energy at a set of configurations and then computing derivative. It is also important to note that HF theorem is based on the assumption that the basis set is complete. But in realistic calculations, the basis set is actually truncated. It originates an additional force called the Pulay force [11, 12].

1.7.1 Pseudopotential Approximation

It is well known fact that physical and chemical properties of many systems are primarily affected by the number of valance electrons and less dependent on the core electrons. Pseudopotential (PP) approximation [13, 14]is based on this idea. Since core electrons are bound tightly and highly localized in nature, it is necessary to utilize a large plane-wave basis set to do all-electron calculation which is computationally very costly. To reduce this computational cost, within Pseudo potential approximation, the strong ionic potential are replaced by a weaker pseudo potential which can be assumed as pseudo wavefunction of only the valance electrons. Hence, effectively core electrons are removed and their effect is taken into account as pseudo potential of ions. It is interesting to note that the oscillations of valance electrons in the core region are discarded. This approximation also ensure that pseudo wave functions also match well with the actual valance wave function beyond a certain distance from the nucleus. This critical distance also named as 'cut-off 'radius. If this cut-off radius is large, pseudopotential are said to be softer. A good quality of PP approximation mainly depend on smoothness and transferability properties. In principle, PP should be universal in nature in the sense same PP can be used in several different kind of chemical and structural environments. The PP approximation dramatically reduces the required E_{cut} for the plane wave basis.

There exist two common form of pseudopotential, named as norm-conserving[15–17] and ultrasoft pseudopotential [18]. In the norm-conserving pseudopotential, construction is done in such a way that the integrated charge densities (squared amplitudes of wave function) of the real and pseudo wavefunctions are exactly same in both the core and valance regions. In the ultrasoft pseudopotential, norm-conserving criterion is relaxed. It basically chooses smoother core region and thus reduces the computational cost. However, one need to take extra care to make sure that error because of reducing charge density in the core region is not significant.

1.7.2 k-point Sampling

One of the most difficult task in DFT calculation is to perform integration over all the wave vectors in the first Brillouin zone (BZ). Since there are infinite number of k-points, one should do integration over infinite number of k-points which lead to infinite computational time. But in realistic calculation, the summation is done over a finite number of k-points instead of integration. For example, in the density $n(r)$ calculation, the integration is approximated as follows:

$$n(r) = \frac{V}{(2\pi)^3} \int n_k(r) dk \approx \sum_{k \in IBZ} n_k(r) \omega_k \tag{1.12}$$

Where V stands for unit cell volume and ω_k specifies the weight corresponding to each k-point and $n_k(r)$ can be given as

$$n_k(r) = \sum_i \Psi^*_{i,k}(r) \Psi_{i,k}(r) \tag{1.13}$$

Here k is the k-points in the irreducible part of the Brillouin zone (IBZ) and the sum run over occupied states i. There are various scheme such as suggested by Monkhorst and Pack [19] or by Chadi and Cohen [20] for selecting the k-points in the BZ as needed to perform these sum. However, error can be introduced in the discretization of k-points which can be reduced by taking large number of k-points in the calculations.

Since for the metallic systems energy level are filled upto Fermi level, one does not need to sum over entire bands. If i is the band index, then total occupation can be considered as the weighted sum over the IBZ of occupancies $f_i(k)$ at each k-point, and given as

$$\bar{f}_i(k) = \sum_{k \in IBZ} \omega_k f_i(k) \theta_i\big(E_i(k) - E_f\big) \tag{1.14}$$

Where $\theta_i\big(E_i(k) - E_f\big)$ stands for the step function. This function makes sure that the occupation is one(zero) for each levels lying below (above) the Fermi level. In realistic calculation, this function needs a very fine sampling in the reciprocal space (a large number of k-points) to be resolved completely. But this is computationally expensive. That is why, one should find out a strategy where sharp step function is substituted by a smooth function $F_i\big(E_i(k)\big)$. In this case, total occupation can be written as

$$\bar{f}_i(k) = \sum_{k \in IBZ} \omega_k f_i(k) F_i\big(E_i(k)\big) \tag{1.15}$$

Thus, smearing technique makes it possible to use fewer k-points.

There exist various smearing technique such as Gaussian smearing[21], Methfessel-Paxton smearing [22] and Marzari-Vanderbilt smearing [23].

1.8 Nudged Elastic Band Method

One of the central problem in theoretical chemistry is to find out lowest energy path in which a group of atoms rearrange themselve by going from one configuration to another configuration. Such path is called as ‘minimum energy path ’(MEP) along which potential energy maximum corresponds to saddle-point energy. Finding out saddle-points and reaction paths are the key questions in Transition state theory [24]. In order to find out these quantities, many different methods have been employed. Some of the methods adopts local minimum on the potential energy surface as initial state and search of a path of slowest ascent [25, 26]. However, such ascent paths does not necessarily yield to saddle points. Another common strategy [27, 28] is to compute normal modes with in harmonic approximation of potential energy surface and follow each of these modes until saddle point is achieved. But within this scheme, each step involves with evaluation and diagonalization of second derivative matrix and turns out be computationally expensive. As an alternative, other methods such as ‘drag method ’or ‘reaction coordinate method ’are proposed that need only computation of first derivative. In this scheme, two point boundary condition is utilized where both the initial and final configuration for the transition are given. Within this methods, linear interpolation between the initial and final configuration is done by assigning some subset of coordinates as progress variable parameter. This degree of freedom is varied in equal interval from initial to final state and minimization is done over remaining degrees of freedom. For example, at each step, minimization is performed over (3N-1) degrees of freedom if we are interested in a system consisting of N number of atoms in 3 dimension. These approaches are successful in many simple cases.

Unfortunately, it fails for complicated ones. Mainly, it goes through difficulties like the generated path can be discontinuous and depending on the direction of ‘drag’, some atomic coordinates may ‘slip ’in the neighborhood region of the saddle point. As a result, correct solution of saddle point configuration can not be obtained [29, 30]. Another two-point method, named as ’Chain-of-States methods’ is also introduced which is described in the next section.

In the ‘Chain-of-state method ’, it is assumed that images of the systems are connected with each other by spring. If natural length of the spring is zero, object function can be written as

$$S^{PEB}(\vec{R}_1, \vec{R}_2, ..., \vec{R}_{P-1}) = \sum_{i=0}^{P} V(\vec{R}_i) + \sum_{i=1}^{P} \frac{P_k}{2}(\vec{R}_i - \vec{R}_{i-1})^2 \qquad (1.16)$$

This chain can be thought of as Feynman Path integral corresponding to off-diagonal element of the density matrix which describes a quantum particle. To find out MEPs for classical system, one can think of minimizing the object function as given in eq(1.16) with respect to the intermediate images, keeping end-point images fixed. This procedure can be termed as ‘plain elastic band’(PEB) method. However, in reality, it fails to predict the MEP in most of the time. Hence, modification of eq(1.16) is needed. Before we go to that discussion, first observe this object function more carefully.

In the continuum limit, object function, as given in eq(1.16) reduces to

$$S^{PEB} = P \int d\lambda \Bigg(VR(\lambda) + \frac{k(p)}{2p} |\frac{dr}{d\lambda}|^2 \Bigg) \qquad (1.17)$$

Where P is the number of images and $k(P)$ specify spring constant. Here two cases can occur.

- $\frac{k(P)}{2P}$ →finite (non-zero). In this limit, stiffness of the band yield to ‘corner-cutting ’
- $\frac{k(P)}{2P} \to 0$. In this limit, it may happen the path will not go through the saddle point.

All of these difficulties are overcome in the Nudged Elastic Band method (NEB). In the NEB method, optimization of an elastic band is performed by projecting perpendicular component of the spring force and the parallel component of the true force. Within this scheme, the force acting on the i^{th} image can be written as

$$\vec{F}_i^0 = -\vec{\nabla}V(\vec{R}_i)|_\perp + \vec{R}_i^s.\hat{\tau}_\parallel\hat{\tau}_\parallel \tag{1.18}$$

The advantage of this force projection is that now the dynamics of the path is decoupled from the particular distribution of images, given in the discrete representation of the path. This decoupling scheme and discrete representation of the path are two key ingredients to make sure the convergence to the MEP.

NEB has been employed successfully to a wide-range of problems, such as diffusion process at metal surface [31], multiple-atom exchange process [32], dissociative adsorption of a molecule on a surface [33], contact formation between metal tip and a surface [34]. In this thesis, we have also extensively used this method.

Bibliography

[1] H. Chadwick and R. D. Beck, *Chem. Soc. Rev.*, 2016, –.

[2] P. Hohenberg and W. Kohn, *Phys. Rev.*, 1964, **136**, B864–B871.

[3] W. Kohn and L. J. Sham, *Phys. Rev.*, 1965, **140**, A1133–A1138.

[4] D. M. Ceperley and B. J. Alder, *Phys. Rev. Lett.*, 1980, **45**, 566–569.

[5] J. P. Perdew and A. Zunger, *Phys. Rev. B*, 1981, **23**, 5048–5079.

[6] A. D. Becke, *Phys. Rev. A*, 1988, **38**, 3098–3100.

[7] J. P. Perdew and Y. Wang, *Phys. Rev. B*, 1992, **45**, 13244–13249.

[8] J. P. Perdew, K. Burke and M. Ernzerhof, *Phys. Rev. Lett.*, 1996, **77**, 3865–3868.

[9] P. Giannozzi, S. Baroni, N. Bonini, M. Calandra, R. Car, C. Cavazzoni, D. Ceresoli, G. L. Chiarotti, M. Cococcioni, I. Dabo, A. Dal Corso, S. de Gironcoli, S. Fabris, G. Fratesi, R. Gebauer, U. Gerstmann, C. Gougoussis, A. Kokalj, M. Lazzeri, L. Martin-Samos, N. Marzari, F. Mauri, R. Mazzarello, S. Paolini, A. Pasquarello, L. Paulatto, C. Sbraccia, S. Scandolo, G. Sclauzero, A. P. Seitsonen, A. Smogunov, P. Umari and R. M. Wentzcovitch, *Journal of Physics: Condensed Matter*, 2009, **21**, 395502 (19pp).

[10] R. P. Feynman, *Phys. Rev.*, 1939, **56**, 340–343.

[11] P. Pulay, *Molecular Physics*, 1969, **17**, 197–204.

[12] M. Scheffler, J. P. Vigneron and G. B. Bachelet, *Phys. Rev. B*, 1985, **31**, 6541–6551.

[13] J. C. Phillips, *Phys. Rev.*, 1958, **112**, 685–695.

[14] M. T. Yin and M. L. Cohen, *Phys. Rev. B*, 1982, **25**, 7403–7412.

[15] D. R. Hamann, M. Schlüter and C. Chiang, *Phys. Rev. Lett.*, 1979, **43**, 1494–1497.

[16] A. Zunger and M. L. Cohen, *Phys. Rev. B*, 1979, **20**, 4082–4108.

[17] G. B. Bachelet, D. R. Hamann and M. Schlüter, *Phys. Rev. B*, 1982, **26**, 4199–4228.

[18] D. Vanderbilt, *Phys. Rev. B*, 1990, **41**, 7892–7895.

[19] H. J. Monkhorst and J. D. Pack, *Phys. Rev. B*, 1976, **13**, 5188–5192.

[20] D. J. Chadi and M. L. Cohen, *Phys. Rev. B*, 1973, **8**, 5747–5753.

[21] C. L. Fu and K. M. Ho, *Phys. Rev. B*, 1983, **28**, 5480–5486.

[22] M. Methfessel and A. T. Paxton, *Phys. Rev. B*, 1989, **40**, 3616–3621.

[23] N. Marzari, D. Vanderbilt, A. De Vita and M. C. Payne, *Phys. Rev. Lett.*, 1999, **82**, 3296–3299.

[24] G. H. Vineyard, *Journal of Physics and Chemistry of Solids*, 1957, **3**, 121–127.

[25] C. J. Cerjan and W. H. Miller, *The Journal of Chemical Physics*, 1981, **75**, year.

[26] W. Quapp, *Chemical Physics Letters*, 1996, **253**, 286–292.

[27] H. Taylor and J. Simons, *J. Phys. Chem.*, 1985, **89**, 685.

[28] J. Baker, *Journal of Computational Chemistry*, 1986, **7**, 385–395.

[29] T. A. Halgren and W. N. Lipscomb, *Chemical Physics Letters*, 1977, **49**, 225–232.

[30] M. J. Rothman and L. L. Lohr, *Chemical Physics Letters*, 1980, **70**, 405–409.

[31] M. Villarba and H. Jónsson, *Surface Science*, 1994, **317**, 15–36.

[32] M. Villarba and H. Jónsson, *Surface Science*, 1995, **324**, 35–46.

[33] G. Mills and H. Jónsson, *Phys. Rev. Lett.*, 1994, **72**, 1124–1127.

[34] M. R. Sørensen, K. W. Jacobsen and H. Jónsson, *Phys. Rev. Lett.*, 1996, **77**, 5067–5070.

Chapter 2

Size-selective Electrocatalytic Activity of $(\mathrm{Pt})_n/\mathrm{MoS}_2$ for Oxygen Reduction Reaction

Contents

Fuel cells have been deemed to be one of the most potential and renewable energy resources that may take the place of fossil fuels in future. It can convert the chemical energy from a fuel into electricity via a chemical reaction in the presence of oxygen or other oxidizing agents. However, the conversion efficiency is controlled by the reaction that takes place at the cathode, known as oxygen reduction reaction (ORR), which is found to be a critical process in producing electricity. [1] In fact, the sluggish kinetics of ORR accounts for the major portion of the voltage drop. For example, the current system operates at voltage of only 0.7 V, which is far from the equilibrium potential of 1.23 V and thus significantly limits the performance of the fuel cells for the practical purpose. To date, Pt has been represented to be one of the best cathode electrocatalyst and widely applied in fuel cells because of its relatively better catalytic reactivity; [2–5] but the large-scale commercialization is held back due to its high cost, limited supply and insufficient efficiency. Hence, reducing the Pt content and improving the rate of ORR at the cathode have become the primary targets in the research of fuel cells for the last few decades. [6–10] Toward this end, subnanometer Pt nanoparticles anchored on two-dimensional (2D) naomaterials [11–13] distinguished themselves as a promising electrocatalyst for ORR. Depositing Pt nanoparticle on a substrate is indeed a very useful strategy to reduce the loading and at the same time increase the specificity and mass activity of Pt. Interestingly, Pt nanoparticles supported on the various 2D nanomaterials, such as defective graphene,[14–18] graphene oxide,[19] functionalized graphene,[20, 21] BN sheet[22, 23] etc. are found to exhibit superior catalytic activity and durability in ORR, compared to commercial Pt/C. This is clearly attributed to the change in the mechanical and electronic properties of Pt, when it transforms to nanoparticle form from the bulk phase. This evidently has direct impact on the stability and catalytic activity of a material. Among various materials explored, metal dichalcogenides have also emerged as novel templates for the formation of functional composites in recent years. [24–26] Recent experimental study indicated that MoS_2 nanosheets can be employed to direct the epitaxial growth of Pd, Pt and Ag nanostructures under ambient condition using wet-chemical synthetic approach.[27] Moreover, the favourable interaction between small $(Pt)_n$ islands with $n \leq 12$ and a monolayer of $MoS_2(001)$ substrate as determined by density functional theory approach [28] is a positive signature, which indicates that Pt/MoS_2 hybrid composite might be a durable cathode catalyst in fuel cells. However, to the best of our knowledge, we lack the detailed investigation of synergistic effect of $(Pt)_n/MoS_2$ combination towards ORR, which might be very important strategy for the design of better electrocatalyst for the fuel cell.

In the present chapter, we have systematically studied the ORR activity of a series of $(Pt)_n$ sub-nanoclusters, $(Pt)_1$, $(Pt)_2$, $(Pt)_3$, $(Pt)_5$, $(Pt)_7$, $(Pt)_{10}$ and $(Pt)_{12}$ on the two different types of MoS_2 substrates, semiconducting MoS_2 ($2H\text{-}MoS_2$) and metallic MoS_2 ($1T\text{-}MoS_2$), using first principles density functional theory. The adsorption of the most likely oxygenated species, $^*O_2$, $^*OOH$, $^*O$, $^*OH$, OH_2 involved in ORR on all the $(Pt)_n/MoS_2$ systems have been examined. (throughout the chapter * represents adsorbed species) The complete conversion of O_2 to H_2O (ORR) consists of four elementary reaction steps. The associated free energies for all the steps are then computed. The ORR activity of all the $(Pt)_n/MoS_2$ heterosystems have been described with the Gibbs adsorption free energy of an oxygenated species, namely, $^*OH$ ($\Delta G_{^*OH}$) and that gives rise to a volcano plot. These results would be helpful as guidance for designing new electrocatalysts for ORR with minimal amount of Pt loading.

2.1 Computational Details

Geometry optimization and total energy calculations have been carried out with density functional theory (DFT) framework as implemented in Quantum Espresso [29] code. Throughout the work, we employed generalized gradient approximation (GGA) using PW91.[30] functional. The ionic cores were described by the ultrasoft pseudopotentials taken from the publicly available repository of the Quantum Espresso distribution. Brillouin zone sampling was performed with Monkhorst-Pack scheme [31] and the k-point grid of 3×3×1 have been used for all the calculations. The Kohn-Sham wave-functions were expanded with a plane wave basis sets with a kinetic energy cutoff of 30 Ryd. Electronic occupancies were allowed by using an energy smearing of 0.01 Ryd of Marzari-Vanderbilt scheme. The MoS_2 substrates in the present study were modeled as periodic (3×3) and (5×5) unit cells to place different sizes of the clusters. To describe the isolated metallic nanoparticles, the distance between two periodic images of the clusters have been maintained 10 Åwith vacuum of 15 Åin the direction perpendicular to the slab for avoiding any fictitious interactions among the nighbouring images. Adsorption calculations have been performed with adsorbate species adsorbed on only one side of the system. To account for any van der Waal interactions, dispersion corrections have been considered. All of the atomic coordinates in $(Pt)_n/MoS_2$ were optimized until the forces on each atom become less than 0.001 eV/Ang. To compute the

Gibbs free energy of the electrochemical reactions involving electron/proton transfer, the computational hydrogen electrode (CHE) model was used. [3] In this model, the reference potential is set to be the standard hydrogen electrode (SHE). This makes the reaction free energy of 1/2 H_2 (g) $\leftrightarrow$ H^+ (aq) + e^- reaction is zero at zero electrode potential (U=0) at the standard conditions, that is 298 K, 1 bar of H_2 and at pH 0. At $U \neq 0$, the free energy of a particular reaction changes as a function of the applied potential which is included upto first order as follows:

$$\Delta G_n(U) = \Delta G^0 + neU \tag{2.1}$$

where, ΔG^0 is the free energy at U=0, U is the applied electrode potential, e is the elementary charge and n is the number of electron-proton pairs transferred with respect to O_2. The change in the free energy of the complete reaction O_2 + $2H_2 \rightarrow 2H_2O$ is fixed at the experimental value of 4.92 eV. The model is based on the thermochemistry of the electrochemical reactions including the effects of zero point energy corrections (ZPE) and entropy contributions ($T\Delta S$). ZPE values for the adsorbed species are estimated by performing normal-mode vibrational analysis considering all 3N degrees of freedom while for the gaseous molecules, the ZPE values are obtained from standard table. The entropy values of gaseous molecules are taken from the standard table and the same for the adsorbed species have been ignored in the present study.

2.2 Results and Discussions

2.2.1 Adsorption of Key Intermediates

We have studied the deposition of a series of Pt clusters (Pt_1, Pt_2, Pt_3, Pt_5, Pt_7, Pt_{10} and Pt_{12}) on two different MoS_2 surfaces, namely, 2H-MoS_2 and 1T-MoS_2, denoted as $(Pt)_n$/2H-MoS_2 and $(Pt)_n$/1T-MoS_2 respectively. Due to fluxional character, metal nanocluster can exhibit in several structurally different configurations within a narrow energy window and thereby, computationally it is quite challenging to ascertain the global minima structures of nanoclusters. However, in the present study, we have considered the initial geometries of supported Pt clusters as discussed in the recent study by Wissam. [28] We have carried out the relaxation of different initial configurations of supported Pt clusters which can be reliably predicted as found in the previous studies. Among them, we chose the lowest-energy configurations (Fig. 2.1 and Fig. 2.2) to carry out further study.

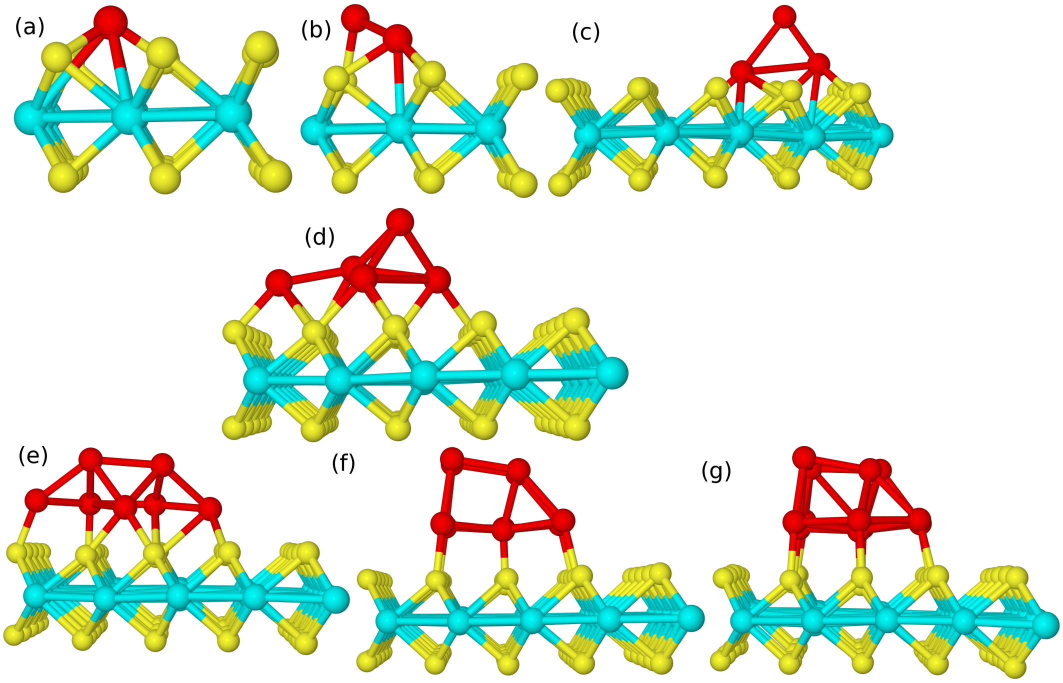

Figure 2.1: Optimized structures of $(\mathrm{Pt})_n$/2H-MoS$_2$ systems with (a) n=1, (b) n=2, (c) n=3, (d) n=5, (e) n=7, (f) n=10 and (g) n=12. S, Mo and Pt atoms are shown as yellow, cyan and red spheres respectively.

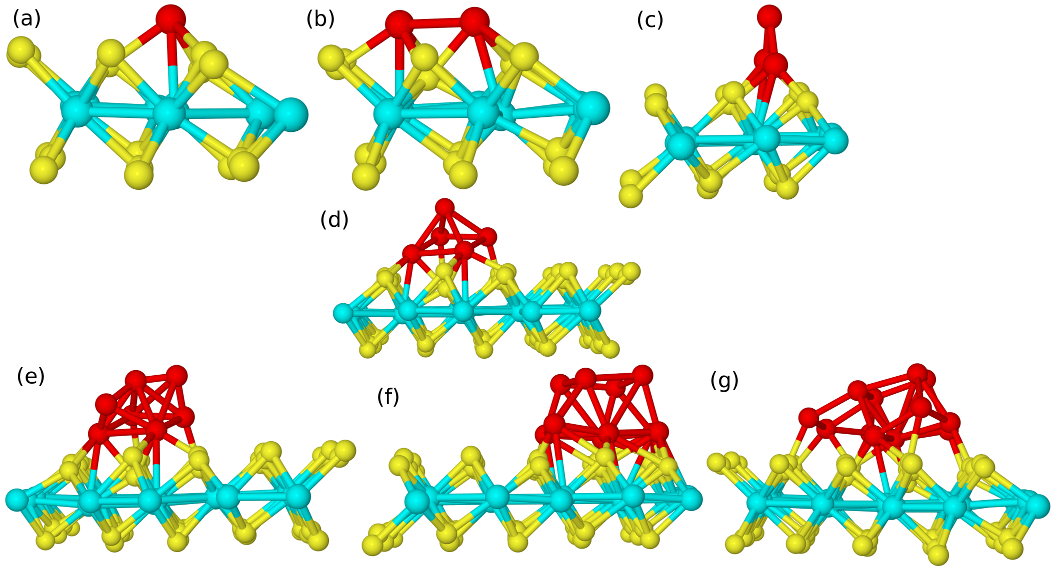

Figure 2.2: Optimized structures of $(\mathrm{Pt})_n$/1T-MoS$_2$ systems with (a) n=1, (b) n=2, (c) n=3, (d) n=5, (e) n=7, (f) n=10 and (g) n=12. S, Mo and Pt atoms are shown as yellow, cyan and red spheres respectively.

The binding energy per Pt for $(\mathrm{Pt})_n$ cluster on $\mathrm{MoS_2}(001)$ substrates is calculated using the following equation (eq 2.2):

$$E_{BE} = \frac{1}{n}[E_{(Pt)_n/MoS_2} - E_{MoS_2} - nE_{Pt}] \tag{2.2}$$

where $E_{(Pt)_n/MoS_2}$ is the total energy of the optimized $(\mathrm{Pt})_n/\mathrm{MoS_2}$ heterostructure, E_{MoS_2} is the total energy of the pristine $\mathrm{MoS_2}$ monolayer and E_{Pt} is the energy of the isolated Pt atom. In this convention, negative values of E_{BE} indicate energetically favourable interaction between Pt clusters and $\mathrm{MoS_2}$ surfaces.

Table 2.1: Total Binding energies Δ E_{BE} (eV) of the Pt nanoparticles on 2H and 1T MoS_2 Surfaces

Model structure	Energy (eV)
Pt_1/2H-MoS_2	-2.78
Pt_2/2H-MoS_2	-2.90
Pt_3/2H-MoS_2	-3.19
Pt_5/2H-MoS_2	-3.45
Pt_7/2H-MoS_2	-3.68
Pt_{10}/2H-MoS_2	-3.92
Pt_{12}/2H-MoS_2	-4.09
Pt_1/1T-MoS_2	-2.92
Pt_2/1T-MoS_2	-3.15
Pt_3/1T-MoS_2	-3.42
Pt_5/1T-MoS_2	-3.80
Pt_7/1T-MoS_2	-3.98
Pt_{10}/1T-MoS_2	-4.12
Pt_{12}/1T-MoS_2	-4.25

We find that our computed binding energies (Table 2.1) are in good agreement with the previous study.[28] Moving to the ORR investigations, the essential first step is to elucidate the behavior of key adsorbates ($^*O_2$, *OOH, *O, *OH) involved in ORR on the Pt-MoS_2 heterostructures. The corresponding adsorbed structures have been shown in Fig. 2.3.

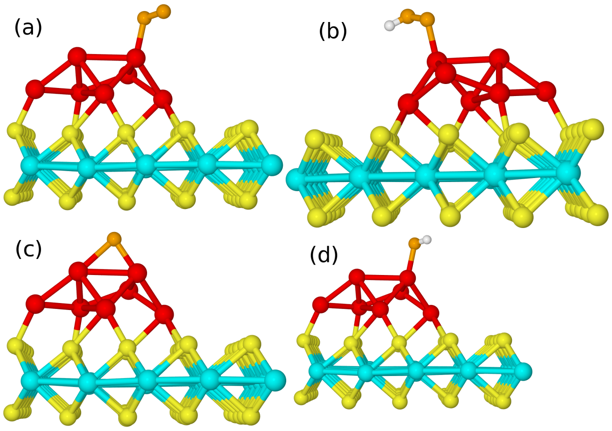

Figure 2.3: Lowest energy configurations of (a)$^*O_2$, (b)$^*OOH$, (c)$^*O$ and (d)$^*OH$ on $(Pt)_7$/2H-MoS_2. S, Mo, Pt, O and H atoms are shown as yellow, cyan, red, orange and white spheres respectively.

The reaction free energies are calculated from the Gibbs free-energy at standard conditions (T = 298 K, pH_2 = 1 bar and pH = 0) through

$$\Delta G = \Delta G_0 + \Delta G(U) \tag{2.3}$$

where, $\Delta G_0 = \Delta E + \Delta E_{ZPE} - T\Delta S$. Here ΔE is the reaction energy calculated from DFT, ΔE_{ZPE} denotes the difference in zero-point energies and $T\Delta S$ is the entropic contribution. The Gibbs adsorption free energy values for all the oxygenated adsorbates, i.e., ΔG_{*O2}, ΔG_{*OOH}, ΔG_{*O} ΔG_{*OH}, have been computed through the following reactions, where H_2 and H_2O are taken as references:

$$^* + 2H_2O \longleftrightarrow ^* O_2 + 2H_2 \tag{2.4}$$

$$^* + 2H_2O \longleftrightarrow ^* OOH + 3/2H_2 \tag{2.5}$$

$$^* + H_2O \longleftrightarrow ^* O + H_2 \tag{2.6}$$

Table 2.2: Gibbs Adsorption Free Energy Values (eV) of the Key Oxygenated Intermediates adsorbed on Pt nanoparticles on 2H and 1T MoS_2 Surfaces.(T(atop); B(bridge); H(hollow))

Model structure	ΔG_{*OOH}	ΔG_{*O}	ΔG_{*OH}
$Pt_1/2H\text{-}MoS_2$	3.86 (T)	2.20 (T)	0.71 (T)
$Pt_2/2H\text{-}MoS_2$	3.49 (T)	1.41 (B)	0.09 (B)
$Pt_3/2H\text{-}MoS_2$	3.965 (T)	1.47 (T)	0.85 (T)
$Pt_5/2H\text{-}MoS_2$	3.98 (T)	1.85 (T)	0.85 (T)
$Pt_7/2H\text{-}MoS_2$	3.94 (T)	1.80 (B)	0.90 (T)
$Pt_{10}/2H\text{-}MoS_2$	3.92 (T)	1.63 (B)	0.76 (T)
$Pt_{12}/2H\text{-}MoS_2$	3.90 (T)	1.63 (H)	0.76 (B)
$Pt_1/1T\text{-}MoS_2$	3.79 (T)	1.87 (T)	0.59 (T)
$Pt_2/1T\text{-}MoS_2$	3.69 (B)	1.29 (B)	0.42 (B)
$Pt_3/1T\text{-}MoS_2$	3.65 (T)	1.71 (B)	0.44 (T)
$Pt_5/1T\text{-}MoS_2$	3.73 (T)	1.64 (T)	0.52 (T)
$Pt_7/1T\text{-}MoS_2$	3.75 (T)	1.62 (T)	0.57 (T)
$Pt_{10}/1T\text{-}MoS_2$	3.80 (T)	1.58 (B)	0.63 (T)
$Pt_{12}/1T\text{-}MoS_2$	3.74 (T)	1.67 (H)	0.61 (T)

$$^* + H_2O \longleftrightarrow ^* OH + 1/2H_2 \tag{2.7}$$

respectively. The values are tabulated in Table 2.2. It should be pointed out here that the adsorption free energy values thus calculated do not signify the absolute strength of adsorption for each species. The calculated adsorption free energies for *OOH and *O (ΔG_{*OOH} and ΔG_{*O}) has been plotted as a function of *OH (ΔG_{*OH}) for all the $(Pt)_n/MoS_2$ heterostructures Fig. 2.4.

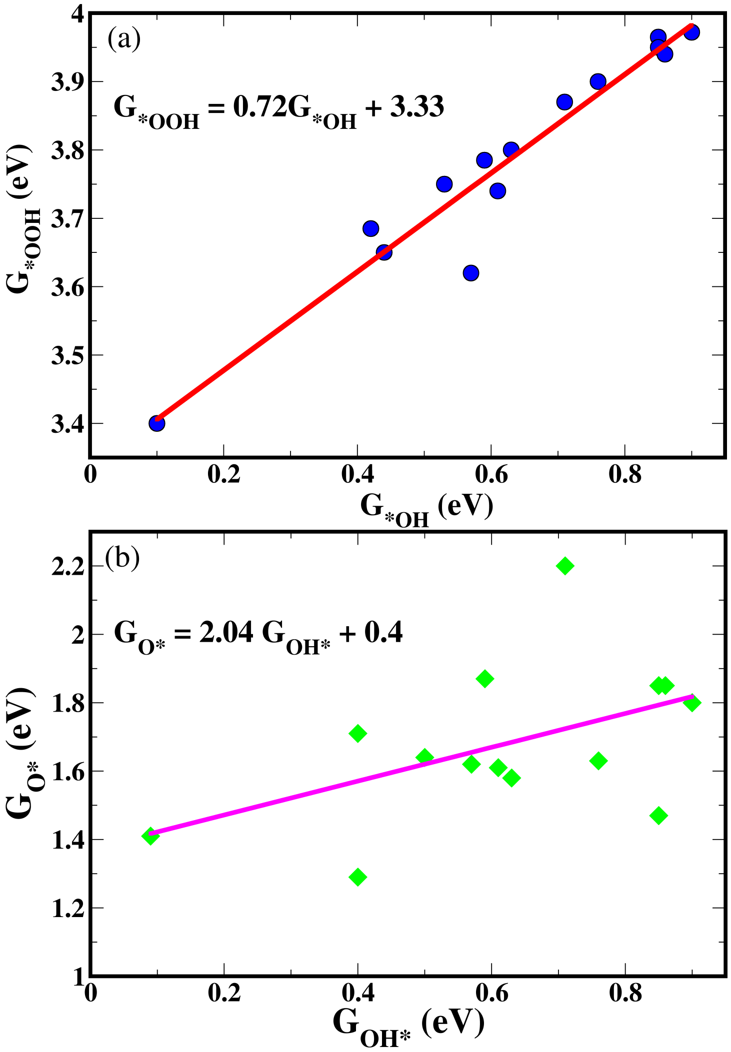

Figure 2.4: Scaling relations between adsorption free energy values of (a) *OOH and *OH and (b) *O and *OH associated with various $(\mathrm{Pt})_n$ clusters adsorbed on 2H and 1T $\mathrm{MoS_2}$ monolayers

Using these data, the following linear relationships can be fitted,

$$\Delta G_{*OOH} = 0.72\Delta G_{*OH} + 3.33eV \tag{2.8}$$

$$\Delta G_{*O} = 2.04\Delta G_{*OH} + 0.40eV \tag{2.9}$$

From Fig. 2.4, it is clear that data points of ΔG_{*OOH} vs ΔG_{*OH} plot fall along the fitted linear line with the free energy intercept, which is quite comparable with the previously found intercept for metal surfaces ($\Delta G_{*OOH} \approx \Delta G_{*OH}$ + 3.2 eV). However, there is discrepancy in the slope value which is believed to be due to the difference in adsorption sites (atop, bridge or hollow) of *OH intermediate on different $(Pt)_n/MoS_2$ systems, while for all the cases, *OOH adsorbs atop with a single bond between O and Pt atom. In comparison, Figure 2.4(b) shows very weak linear correlation between ΔG_{*O} and ΔG_{*OH} data points. There is large deviation in intercept values from that on the metal-based materials ($\Delta G_{*O} = 2\ \Delta G_{*OH}$ - 0.08 eV) and this is understandable from the different binding modes of *OH and *O for each systems as discussed for the previous case. These relations allow to describe the ORR activity of different electrocatalysts with the adsorption free energy of single oxygenated species. However, the scaling relationship between the adsorption free energies of the oxygenated species is considered to be the origin of the higher overpotential of the ORR on the electrocatalysts.[32]

2.2.2 ORR pathway

In general, ORR takes place either through associative or dissociative pathway, or both of them for the conversion of O_2 into H_2O. The number of electrons and protons responsible for the complete reduction process are same in both the cases, however, the two paths basically differ from each other in the very initial step.[33] The associative path is initiated by the direct reduction of O_2 to *OOH, known as peroxo path; while in the dissociative path, O_2 dissociates into 2O* on the catalytic surface, followed by the further reduction reactions. Associative path commences through the concerted proton-electron transfer (PET)-coupled adsorption to form *OOH and basically goes through the following overall reaction:

$$O_2 + (H^+ + e^-) \rightarrow^* OOH \tag{2.10}$$

$$^*OOH + (H^+ + e^-) \rightarrow^* O + H_2O \tag{2.11}$$

$$^*O + (H^+ + e^-) \rightarrow^* OH \tag{2.12}$$

$$^*OH + (H^+ + e^-) \rightarrow^* + H_2O \tag{2.13}$$

However, in the present study, as will be shown later on, steps prior to *OH are relatively facile and hence play a minor role in determining the rate of ORR. Thereby, it is not important, in the present study, to find whether *O$_2$ undergoes an associative or dissociative pathway for assessing the ORR activity.

2.2.3 Activity Volcano Plot and Activity-Determining step

To find out the efficiency of the ORR process, the reaction free-energies of the four elementary steps (eq2.10-2.13) are examined on all the Pt-MoS$_2$ heterostructures, which can be expressed in terms of adsorption free energies of the oxygenated species as follows,

$$\Delta G_1 = \Delta G_{^*OOH} - 4.92 + eU \tag{2.14}$$

$$\Delta G_2 = \Delta G_{^*O} - \Delta G_{^*OOH} + eU \tag{2.15}$$

$$\Delta G_3 = \Delta G_{*OH} - \Delta G_{*O} + eU \tag{2.16}$$

$$\Delta G_4 = -\Delta G_{*OH} + eU \tag{2.17}$$

The reaction step with the smallest value (most negative) is considered as rate-limiting step (RLS) as it represents the thermodynamically least favourable reaction in the complete ORR process and mainly determines the activity of the fuel cell. By using the adsorption free energy values tabulated in Table 2.1, the standard equilibrium potentials of each elementary step, U_i^0 (i = 1, 2, 3, or 4) have been estimated under the condition $\Delta G_i = 0$. The U_i^0 values thus obtained for all the $(Pt)_n/MoS_2$ systems are displayed in Fig. 2.5.

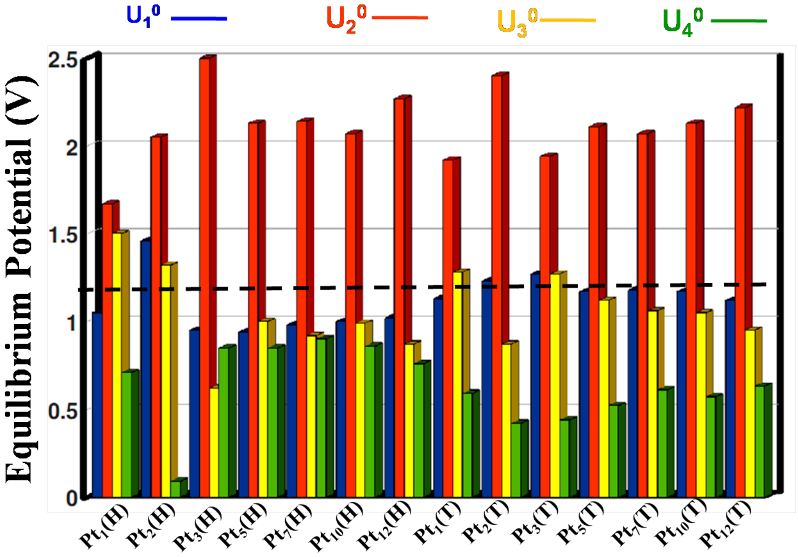

Figure 2.5: Standard equilibrium potential for reaction steps of 2.10-2.13 on the $(Pt)_n/MoS_2$ systems. U_1^0, U_2^0, U_3^0, U_4^0 are represented as blue, orange, yellow, and green bars respectively.

It is evidently seen that for all the systems considered here, $U_2{}^0$ values (Orange bars) are found to be more positive than the equilibrium potential (1.23 V) indicating eq2.11 as a very facile step in the ORR. On the other hand, except $(Pt)_3/2H\text{-}MoS_2$, eq2.13 has the lowest standard equilibrium potential values for all the $(Pt)_n/MoS_2$ heterosystems which means that the reduction of *OH limits the rate and eventually dictate the overall performance of ORR process. This is precisely the reason that ΔG_{*OH} has been considered as a thermodynamic descriptor of ORR activity in the present study. It is important to note that the elementary step which is highly exothermic (eq2.11) impacts the other step(s) to be endothermic and hence retards the overall fuel cell performance. Certainly, in order to have the most efficient fuel cell with all the elementary steps downhill, the free energies of each of the individual steps should be ideally at equilibrium potential, 1.23 V. To visualize this, we have presented free energy diagram for ORR on $(Pt)_5/H\text{-}MoS_2$ system at different U values in Fig. 2.6. It can be clearly seen that on $(Pt)_5/H\text{-}MoS_2$ system, oxygen reduction should run at potentials between 0 and 0.84 V. Hence, for this particular system, 0.84 V is the minimum potential at which all the reaction steps are downhill in free energy. However,

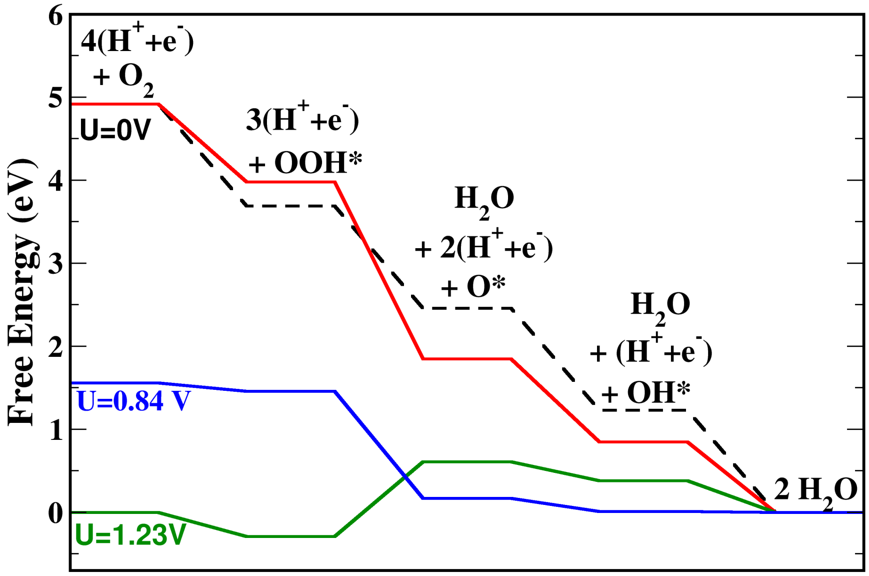

Figure 2.6: Free energy diagram for ORR on $(Pt)_5$/H-MoS_2 system at U = 0 V (red line), U = 1.23 V (green line) and U = 0.84 V (blue line). The optimal ORR catalyst at U = 0 V (black dashed line) is shown for comparison respectively.

Using the scaling relationships between the adsorption free energies of the key intermediates fitted in Figure 2.4(a) and (b), U_i^0 can be expressed in terms of ΔG_{*OH}. This results in thermodynamic activity volcano plot for the ORR as shown in Fig. 2.7.

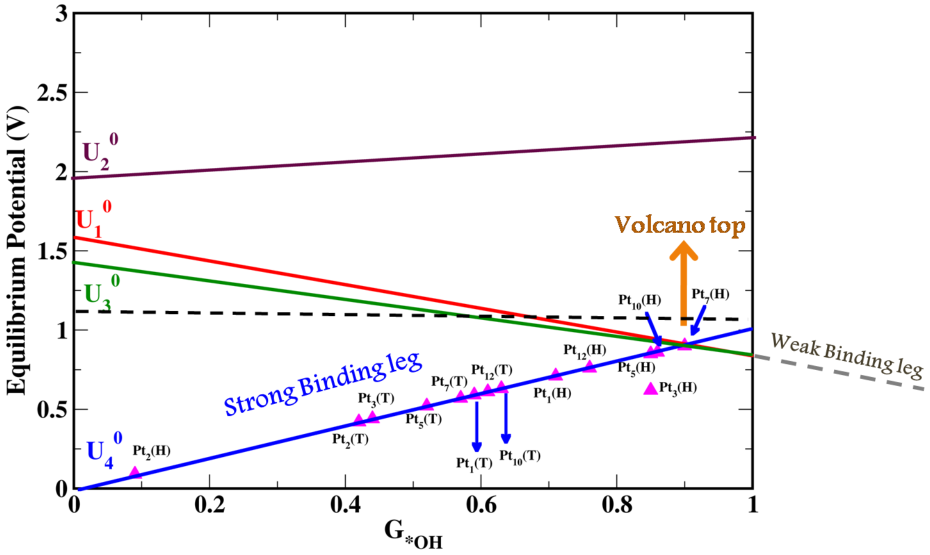

Figure 2.7: Thermodynamic volcano relation for ORR activity as a function of Gibbs adsorption energy of *OH. Magenta data points are the estimated standard equilibrium potentials for the potential-determining step of each system. No system has been detected with weak *OH binding; hence grey dotted line represents guide to the eye to complete the volcano shape.

Interestingly, model relations derived from U_i^0 vs ΔG_{*OH} as given by equations also indicate eq2.13 to be the rate-limiting step in the present case. It can be seen that the system with strong *OH adsorption energy (with relatively less positive ΔG_{*OH}), would have the lowest U_4^0 value. In fact, heterosystems which fall in the strong bonding branch are too oxophilic to act as ORR catalytic centers, e.g., $(Pt)_2$/2H-MoS_2. However, we have not detected any surface site where *OH is very weakly bound. The appearance of a maximum (a volcano) can be related to the Sabatier Principles which states that the binding of the adsorbate to the surface should be optimum for the sake of better catalytic activity. Hence, in principle, the best activity will be achieved at an intermediate *OH adsorption strength where the $U_4{}^0$ vs ΔG_{*OH} and $U_1{}^0/U_3{}^0$ vs ΔG_{*OH} curves cross with each other. In the present study, the volcano top has been appeared at ΔG_{*OH} value around 0.9 V. Interestingly, $(Pt)_7/2H\text{-}MoS_2$, $(Pt)_5/2H\text{-}MoS_2$, $(Pt)_{12}/2H\text{-}MoS_2$ are at or lie close to the volcano top implying these are the potential candidate for ORR with favourable binding strength for *OH. It should be emphasized that in terms of equilibrium potentials, the systems at(near) the top region are found to exhibit better(similar) electrocatalytic activity with respect to that of pure Pt electrocatalyst. This suggests that these systems are quite efficient and economical as well to be electrocatalyst for ORR process. In addition, it should be pointed out that, at ΔG_{*OH} value at which the ORR activity reaches to the volcano top, $U_1{}^0$(0.98 V), $U_3{}^0$(0.92 V) and $U_4{}^0$ (0.90 V) are comparable in values. This indicates that ORR activity should be simultaneously determined by all the three steps, rather than by a single step.

To put our results in firm perspective, we have calculate overpotential η, an experimentally measurable quantity, of the fuel cell as a difference between the equilibrium of the ORR process for each step ($4.92/4 = 1.23$ V) and the lowest potential (RLS) where all the elementary steps are downhill.(Table 2.3) However, this definition is based on the assumption that the binding energies are independent of the applied voltage which is generally an well-established approximation. It can be seen from the Table 2.3 that $Pt_7/H\text{-}MoS_2$ exhibits the lowest overpotential value of 0.33 V, which suggests that it might be the best electrocatalyst with highest efficiency amongst all the systems studied here.

Table 2.3: Calculated Overpotential η (V) of the Pt nanoparticles on 2H and 1T-MoS_2 Surfaces

Model Structure	Overpotential (V)
Pt_1/H-MoS_2	0.52
Pt_2/H-MoS_2	1.14
Pt_3/H-MoS_2	0.61
Pt_5/H-MoS_2	0.38
Pt_7/H-MoS_2	0.33
Pt_{10}/H-MoS_2	0.37
Pt_{12}/H-MoS_2	0.47
Pt_1/T-MoS_2	0.64
Pt_2/T-MoS_2	0.81
Pt_3/T-MoS_2	0.79
Pt_5/T-MoS_2	0.71
Pt_7/T-MoS_2	0.66
Pt_{10}/T-MoS_2	0.60
Pt_{12}/T-MoS_2	0.62

2.2.4 Electronic Structure

It is now evident that the ORR activity of $(Pt)_n/MoS_2$ heterosystems are basically controlled by the binding strength of oxygenated species. To understand the trend in ORR reactivity with the variation in binding of $^*OH$, we have carried out electronic structure calculations. It is found that the binding of $^*OH$ intermediate is directly correlated with the density of d states at the Fermi level. Accordingly, the system with a higher density of d states binds $^*OH$ strongly and vice versa.

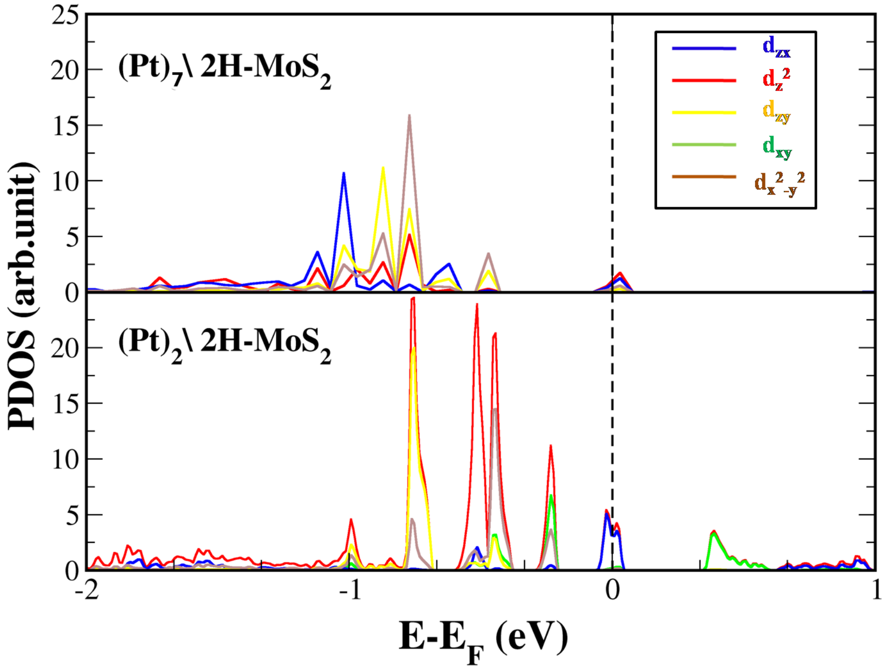

Figure 2.8: Partial density of states (PDOS) of the Pt atom at which *OH is adsorbed.

Fig. 2.8 shows the calculated partial density of states (PDOS) of the Pt atom at which *OH is adsorbed for Pt_2/2H-MoS_2 and Pt_7/2H-MoS_2. It is manifested that Pt_2/2H-MoS_2, which binds *OH strongly, exhibits the higher DOS near the Fermi level in comparison to Pt_7/2H-MoS_2; this explains the moderate oxophilicity of Pt_7/2H-MoS_2 and the corresponding higher ORR activity.

2.3 Conclusion

In summary, this chapter explores a thorough calculations of the ORR pathways on various $(Pt)_n$ clusters (n = 1, 2, 3, 5, 7, 10 and 12) supported on 2H and 1T MoS_2. The final path of ORR, i.e., reduction of *OH to H_2O is identified as the rate-limiting step in the present study. These findings lead to describe the ORR activity of various $(Pt)_n/MoS_2$ systems in terms of single thermodynamic descriptor, namely, Gibbs adsorption free energy of an oxygenated species, *OH. Interestingly, the scaling relation gives rise to model volcano curve which suggests $(Pt)_5$/2H-MoS_2, $(Pt)_7$/2H-MoS_2 and $(Pt)_{12}$/2H-MoS_2 with optimized strength for oxygenated species might be the most promising ORR electrocatalyts amongst the present systems studied. The standard equilibrium potential value at the top region for the activity determining step corresponds to the best achievable ORR activity among the concerned systems in the thermodynamic point of view. Among all the heterosystems, $(Pt)_7$/2H-Mos_2 has been corroborated as the best electrocatalyst for ORR with the lowest overpotential value of 0.33 V. However, the overpotential value is highly dependent on the binding strength of the oxygenated species and that can be correlated with electronic structure of the corresponding systems. The Pt_n/MoS_2 system with a higher density of d states at/near the Fermi level bind oxygenated species stronger.

Our work gives a microscopic insight of ORR activity in a series of $(Pt)_n/Mos_2$ systems which might be helpful for rational material design in future. Overall, our study highlights a novel, highly active oxygen reduction catalyst; moreover, it provides an opportunity to use small Pt clusters, which have a significant economic impact by reducing the amount of precious metal required for an electrocatalytic reaction. To this end, synthetic strategies for controlling the size of the $(Pt)_n$ clusters on 2H-MoS_2 support are highly expected.

Bibliography

[1] H. A. Gasteiger and N. M. Markovi, *Science*, 2009, **324**, 48–49.

[2] H. A. Gasteiger, S. S. Kocha, B. Sompalli and F. T. Wagner, *Applied Catalysis B: Environmental*, 2005, **56**, 9 – 35.

[3] J. K. Norskov, J. Rossmeisl, A. Logadottir, L. Lindqvist, J. R. Kitchin, T. Bligaard and H. Jonsson, *The Journal of Physical Chemistry B*, 2004, **108**, 17886–17892.

[4] A. Fortunelli, W. A. Goddard, Y. Sha, T. H. Yu, L. Sementa, G. Barcaro and O. Andreussi, *Angewandte Chemie*, 2014, **126**, 6787–6790.

[5] V. Viswanathan, H. A. Hansen, J. Rossmeisl and J. K. Nrskov, *ACS Catalysis*, 2012, **2**, 1654–1660.

[6] V. R. Stamenkovic, B. Fowler, B. S. Mun, G. Wang, P. N. Ross, C. A. Lucas and N. M. Markovi, *Science*, 2007, **315**, 493–497.

[7] Y. Sha, T. H. Yu, B. V. Merinov and W. A. Goddard, *The Journal of Physical Chemistry C*, 2012, **116**, 6166–6173.

[8] Y. Sha, T. H. Yu, B. V. Merinov, P. Shirvanian and W. A. Goddard, *The Journal of Physical Chemistry C*, 2012, **116**, 21334–21342.

[9] R. F. de Morais, D. Loffreda, P. Sautet and A. A. Franco, Meeting Abstracts, 2011, pp. 1943–1943.

[10] A. D. Doyle, J. H. Montoya and A. Vojvodic, *ChemCatChem*, 2015, **7**, 738–742.

---

[11] H. D. Ozaydin, H. Sahin, R. T. Senger and F. M. Peeters, *Annalen der Physik*, 2014, **526**, 423–429.

[12] D. Hou, W. Zhou, X. Liu, K. Zhou, J. Xie, G. Li and S. Chen, *Electrochimica Acta*, 2015, **166**, 26 – 31.

[13] T. uk Park, Y. Tomita and T. Nakayama, *Surface Science*, 2014, **621**, 7 – 15.

[14] M. Kaukonen, A. V. Krasheninnikov, E. Kauppinen and R. M. Nieminen, *ACS Catalysis*, 2013, **3**, 159–165.

[15] D.-H. Lim and J. Wilcox, *The Journal of Physical Chemistry C*, 2011, **115**, 22742–22747.

[16] D.-H. Lim and J. Wilcox, *The Journal of Physical Chemistry C*, 2012, **116**, 3653–3660.

[17] Y. Song and S. Chen, *ACS Applied Materials & Interfaces*, 2014, **6**, 14050–14060.

[18] G. He, Y. Song, K. Liu, A. Walter, S. Chen and S. Chen, *ACS Catalysis*, 2013, **3**, 831–838.

[19] N. Jin, J. Han, H. Wang, X. Zhu and Q. Ge, *International Journal of Hydrogen Energy*, 2015, **40**, 5126 – 5134.

[20] Y. Tian, Y.-j. Liu, J.-x. Zhao and Y.-h. Ding, *RSC Adv.*, 2015, **5**, 34070–34077.

[21] C. Galeano, J. C. Meier, M. Soorholtz, H. Bongard, C. Baldizzone, K. J. J. Mayrhofer and F. Schth, *ACS Catalysis*, 2014, **4**, 3856–3868.

[22] D. Xu, Y.-j. Liu, J.-x. Zhao, Q.-h. Cai and X.-z. Wang, *The Journal of Physical Chemistry C*, 2014, **118**, 8868–8876.

[23] X. Chen, W. Zang, K. Vimalanathan, K. S. Iyer and C. L. Raston, *Chem. Commun.*, 2013, **49**, 1160–1162.

[24] J. Deng, H. Li, J. Xiao, Y. Tu, D. Deng, H. Yang, H. Tian, J. Li, P. Ren and X. Bao, *Energy Environ. Sci.*, 2015, **8**, 1594–1601.

[25] B. Xiao, P. Zhang, L. Han and Z. Wen, *Applied Surface Science*, 2014, –.

[26] T. Wang, D. Gao, J. Zhuo, Z. Zhu, P. Papakonstantinou, Y. Li and M. Li, *Chemistry A European Journal*, 2013, **19**, 11939–11948.

[27] Z. B. S. W. M. Q. X. F. Z. Z. H. Huang, Xiao Zeng, *Nat Commun*, 2013, **4**,.

[28] W. A. Saidi, *Crystal Growth & Design*, 2015, **15**, 642–652.

[29] P. Giannozzi, S. Baroni, N. Bonini, M. Calandra, R. Car, C. Cavazzoni, D. Ceresoli, G. L. Chiarotti, M. Cococcioni, I. Dabo, A. Dal Corso, S. de Gironcoli, S. Fabris, G. Fratesi, R. Gebauer, U. Gerstmann, C. Gougoussis, A. Kokalj, M. Lazzeri, L. Martin-Samos, N. Marzari, F. Mauri, R. Mazzarello, S. Paolini, A. Pasquarello, L. Paulatto, C. Sbraccia, S. Scandolo, G. Sclauzero, A. P. Seitsonen, A. Smogunov, P. Umari and R. M. Wentzcovitch, *Journal of Physics: Condensed Matter*, 2009, **21**, 395502 (19pp).

[30] J. P. Perdew, J. A. Chevary, S. H. Vosko, K. A. Jackson, M. R. Pederson, D. J. Singh and C. Fiolhais, *Phys. Rev. B*, 1992, **46**, 6671–6687.

[31] H. J. Monkhorst and J. D. Pack, *Phys. Rev. B*, 1976, **13**, 5188–5192.

[32] M. T. Koper, *Journal of Electroanalytical Chemistry*, 2011, **660**, 254 – 260.

[33] R. F. de Morais, A. A. Franco, P. Sautet and D. Loffreda, *ACS Catalysis*, 2015, **5**, 1068–1077.

Chapter 3

Effect of Doping on the Electrocatalytic Activity of Co_3O_4 for Water Oxidation Reaction

Contents

3.1 Introduction

The electrochemical splitting of water has been considered as an obvious means for producing a carbon-free source of hydrogen for decades. [1] The overall process consists of two reactions: oxygen evolution reaction (OER) at the anode and hydrogen evolution reaction (HER) at the cathode. The change in the Gibbs free energy (ΔG) of the complete process is 237 kJ/mol and the corresponding thermodynamic voltage (i.e. the energy consumption of the process) is 1.23 V, calculated from the well-known relationship, $\Delta G = nFE$, where n defines number of electrons involved, F is the Faraday constant and E stands for electrode potential. This is considered as the minimum voltage required for electrocatalytic decomposition of H_2O into H_2 and O_2. [2]

However, in practical application, the commercial electrolyzers operate between 1.8 to 2.1 V, which indicates the need of large overvoltages to drive the reactions at a sufficiently high rate. [3] The high overvoltage and eventual energy loss are mainly associated with the anodic reaction and apparently the anodic material has strong influence on the efficiency of the water oxidation reaction. Therefore, design of an effective electrocatalyst is highly desired to reduce the overvoltage and simultaneously expedite the sluggish kinetics of OER.

In recent years, first-row transition metal oxides[4, 5] have emerged as highly active, durable and economical options for OER catalyst and can be considered as promising replacement of rare and expensive transition metal oxides (e.g. Ru and Ir). Among many, cobalt-based oxides or complexes show outstanding performance as OER catalyst.[6–8] For example, Co(III/IV) centers [9] of Co-based catalysts are found to be important active sites for catalysis towards the OER, hence a variety of Co-based catalysts with different compositions and morphologies have been explored. It is known that the lattice of Co_3O_4 can host many other metallic cations by partial cobalt substitution. [10, 11] Interestingly, electrocatalytic activity of Co-oxides can be significantly improved by modifying it with other 3d transition metals, Fe, Ni, Cu. [12–14] For example, Li et al. proposed CoNi layered double hydroxides as an efficient OER electrocatalysts in neutral electrolytes.[15] Burke and co-workers have confirmed that incorporation of proper concentrations of Fe enhances the OER activity of Co-Fe (oxy)hydroxides.[16] Thus, extensive amount of experimental research have been dealt with the in-depth investigation of optimal metal ratios or structural phases which leads to the higher OER activities. However, the controversy over real active sites and the different aspects of its kinetics and mechanism of OER still remain to be solved.

In this work, we investigate the effect of different dopants (Fe, Ni and Cu) on the OER activity of Co_3O_4. The complete oxidation cycle is carried out using different intermediate species associated with one electron transfer at a time. We find that the efficiency of the electrochemical reaction is highly dependent on the dopant as well as on its concentration. Importantly, the strategy in this work would open a new route towards design and obtain low-cost, highly active and environmentally friendly OER catalysts.

3.2 Methods and Models

Spin-polarized density functional theory (DFT) have been carried out in the plane wave and ultrasoft pseudopotential framework as implemented in QUANTUM-

ESPRESSO [17]. The PBE[18] exchange-correlation functional functional with on-site coulomb repulsion U term (DFT+U method) was used to improve the description of localized Co d-electrons in Co-oxides with U = 3.52 eV as recommended by the previous studies.[19] The plane wave kinetic energy cut-offs were chosen at 35 and 350 Ryd for the wave functions and augmented densities, respectively. Surfaces were modeled by periodic slabs with 1×1 rectangular surface cell (8.08 ×5.72 $Å^2$) with vacuum width of 15 Å. Symmetric, non-stoichiometric slabs were considered with seven layers. For energy and structural calculations, we sample the surface Brillouin zone using 3×4×1 k-point grid. [20] The BFGS method were employed for ionic relaxation until all forces were smaller than 0.001 a.u. All the calculations were carried out on the ground magnetic state for avoiding the possible errors from various magnetic orderings.

The OER free energy profiles were obtained utilizing the same scheme proposed in the previous study. [21] The standard hydrogen electrode (SHE) has been used as a reference which allow to replace the free energies of proton (G [H^+]) and electron (G [e^-]) with the G [H_2 - eU], where G [H_2] is the free energy of H_2 and U is the electrode potential versus SHE (pH 0, p = 1 bar, T = 298.15 K). According to the OER equilibrium, the free energy of O_2 is expressed as G [O_2] = 4.92 eV + 2G [H_2O] - G [H_2] under standard condition.

3.3 Results and discussion

3.3.1 Structure of Co_3O_4

Co_3O_4 crystallizes in the cubic normal spinel structure (space group Fd3m) with two different types of Co ions in two different oxidation states; Co^{2+} in a tetrahedral coordination and Co^{3+} in an octahedral coordination. The equilibrium crystal shape of Co_3O_4 includes many facets, e.g. (100), (110), (111) etc. However, in this work, we have mainly focused on (110) surface since it has been recently found that it is not only possible to synthesize Co_3O_4 nanorods with predominately exposed (110) surfaces, these are also believed to play major role in the high catalytic activity of Co_3O_4. The Co_3O_4 (110) surface generally have two possible terminations with cationic and anionic characters. Either of the surfaces can be terminated by controlling the synthetic condition. However, it has been found that under Ultra High Vacuum (UHV) conditions, Co_3O_4 (110) cationic terminated surface is more stable than the anionic one. [22] Hence, in the present study, we focus mainly on the clean cationic terminated Co_3O_4 (110) surface. (see Fig. 3.1)

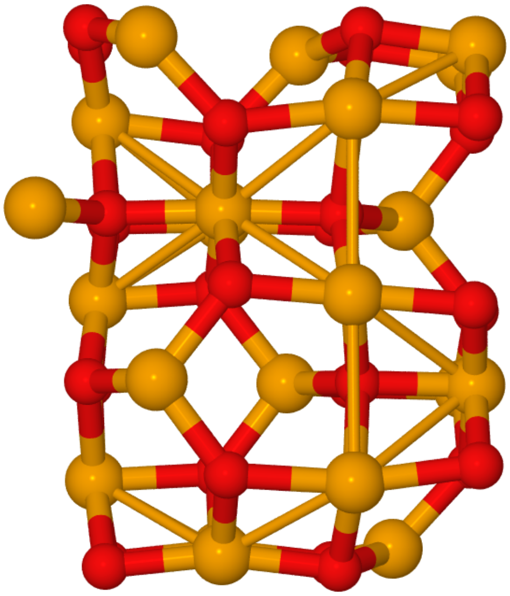

Figure 3.1: Side view of pure cationic terminated Co_3O_4 (110) surface. Orange: Co; Red: O

It exposes four Co ions and four oxygen ions per surface unit cell. There are two types of surface Co ions; they form bonds with two surface oxygen ions and one(two) oxygens in the second layer respectively, so the corresponding Co ions are 3-fold(4-fold) coordinated and designated as Co-3f (Co-4f) hereafter. On the clean Co_3O_4 (110) surface, we examined the substitutional doping of the surface Co ions with the Fe, Ni and Cu metal ions at varying concentrations of 25% and 50%.(Fig. 3.2)

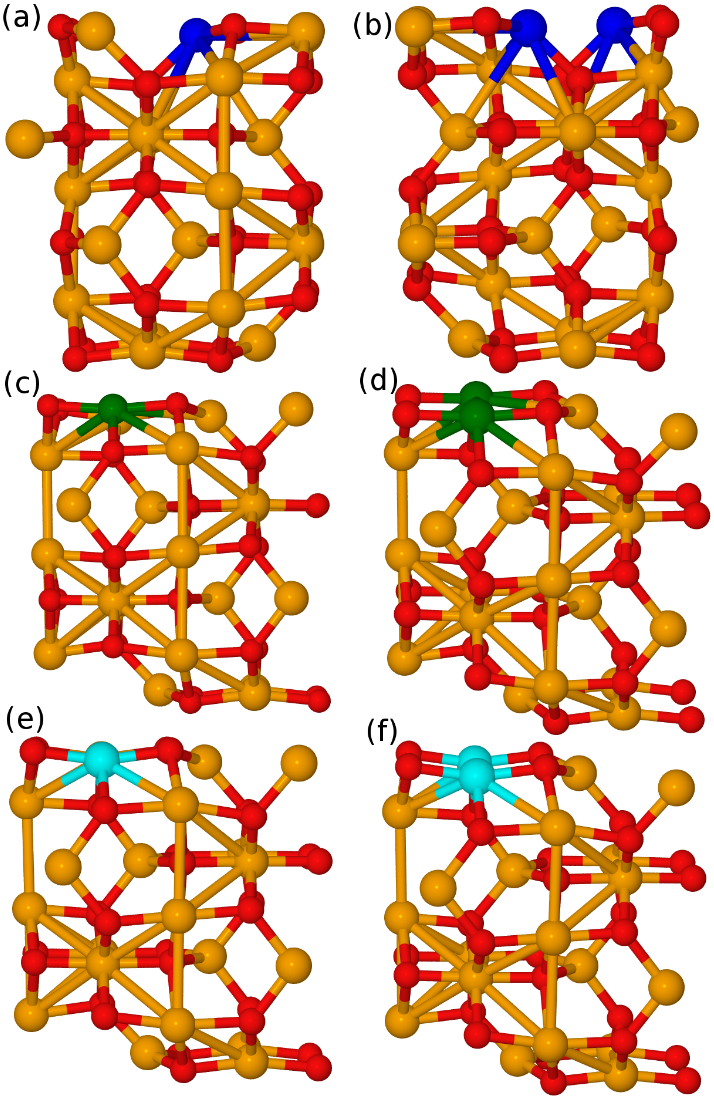

Figure 3.2: Optimised structures of transition metal (M) doped Co_3O_4 at different concentrations (a) M = Cu (25%); (b) M = Cu (50%); (c) M = Ni (25%); (d) M = Ni (50%); (e) M = Fe (25%); (f) M = Fe (50%). Orange: Co; Red: O; Blue: Cu ; Green: Ni ; Cyan: Fe

After investigating all the possible substitution sites, we find that Fe and Ni ions are found to be more stable for substituting with Co-4f ions by 0.19 eV and 0.23 eV respectively, while Cu ion prefers to be substituted with Co-3f ion of the surface Co ions by 0.12 eV. Henceforth, we consider the corresponding favourable sites for the OER.

3.3.2 Energetics of OER

The OER is assumed to comprise of four following elementary reaction steps, each involving the coupled transfer of a proton to water and electron to the electrode until water is completely oxidized to oxygen:

$$H_2O(l) \rightarrow HO * + H^+ + e^- \tag{3.1}$$

$$^*OH \rightarrow O * + H^+ + e^- \tag{3.2}$$

$$^*O + H_2O(l) \rightarrow HOO * + H^+ + e^- \tag{3.3}$$

$$^*OOH \rightarrow * + O_2(g) + H^+ + e^- \tag{3.4}$$

where * and X* denotes surface site and corresponding adsorbed X species respectively. The atomic scale mechanism of OER is found to be complicated and not yet completely established. Nevertheless, the thermodynamic approach, developed by Norskov and co-workers, is considered as first step towards a complete picture of the reaction pathway and is based on minimum set of requirements including binding energy of the intermediates.[23, 24] The additional kinetic barriers between the intermediates have been neglected and that can be justified through the Bronsted-Evans-Polanyi postulate, which states

Table 3.1: Adsorption Energies (eV) of the Key Oxygenated Intermediates adsorbed on pure and doped Co_3O_4 Surfaces. B and H represent bridge and hollow positions, respectively.

Model structure	E_{*OOH}	E_{*O}	E_{*OH}
Co_3O_4	4.20(B)	3.65(B)	1.55(B)
$Fe_xCo_{3-x}O_4$ (x = 25%)	4.28(B)	3.5(B)	1.48(B)
$Fe_xCo_{3-x}O_4$ (x = 50%)	4.40(B)	3.78(B)	1.56(B)
$Ni_xCo_{3-x}O_4$ (x = 25%)	4.02(B)	3.23(B)	1.32(B)
$Ni_xCo_{3-x}O_4$ (x = 50%)	4.13(B)	3.30(B)	1.40(B)
$Cu_xCo_{3-x}O_4$ (x = 25%)	3.96(B)	3.05(B)	1.20(H)
$Cu_xCo_{3-x}O_4$ (x = 50%)	4.07(B)	3.20(B)	1.35(H)

that there is linear correlation between activation energy and reaction free energy. In fact, it has been noted that these additional barriers are typically small for oxygen reduction reation (reverse of the OER) on Pt(111) surface. [21]

Table 3.1 lists the adsorption energies of the key oxygenated intermediates adsorbed on pure and doped Co_3O_4 surfaces. The corresponding structures of the adsorbates on $Fe_xCo_{3-x}O_4$ (x = 25%) has been shown in Fig. 3.3.

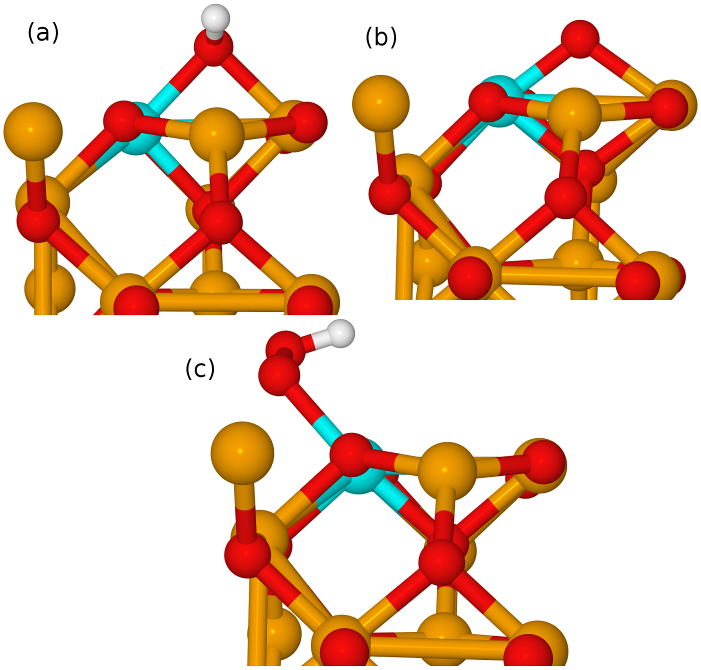

Figure 3.3: Optimised structures of adsorbates (a)*OH; (b)*O; (c)*OOH adsorbed on Fe$_x$Co$_{3-x}$O$_4$ (x = 25%). Orange: Co; Red: O; Cyan: Fe; White: H.

Next, we examined the changes in reaction free energy of the reactions (3.1-3.4) using DFT+U calculations of all the adsorbed intermediates on the considered systems (pure Co$_3$O$_4$ and Cu, Fe and Ni doped Co$_3$O$_4$). To ascertain the effect of dopant on OER, the O$_2$ evolution is assumed to occur mainly at the dopant site. In agreement with the previous study,[25] an approximately linear scaling relationship has been found between the adsorption free energies of *O, *OOH and *OH for both pure and doped surfaces (at different concentrations). Here, we have included the adsorption energies of the lowest energy configurations of the adsorbates. The calculated adsorption free energies for *OOH and *O (Δ G$_{*OOH}$ and Δ G$_{*O}$) is plotted as a function of that for *OH (Δ G$_{*OH}$) (Fig. 3.4).

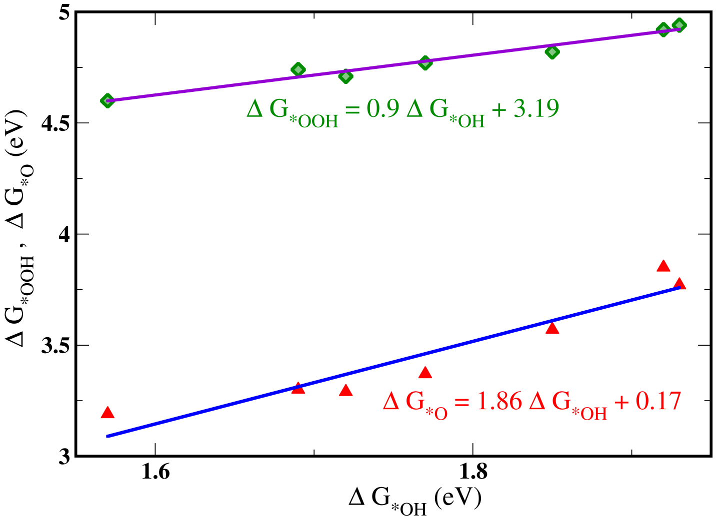

Figure 3.4: Scaling relations between adsorption free energy values of *OOH and *O and that of *OH at surface sites of Co_3O_4 and various doped Co_3O_4

The best fit lines for these energies are Δ G_{*OOH} = 0.9 Δ G_{*OH} + 3.19 and Δ G_{*O} = 1.86 Δ G_{*OH} + 0.17 respectively. The difference in adsorption energies between the *O, *OOH and *OH is in good agreement with the previous studies on metal oxides. [25] However, the small discrepencies in the slope values are due to the difference in binding sites of the adsorbate which varies for individual system. The applicability of this behaviour over a wide range of materials including metals, semiconductors, metal oxides, clusters, graphene analogues proves the universality of the scaling relationship.

3.3.3 Efficiency of OER

The efficiency of the OER process is determined by calculating the reaction free-energies of the individual elementary steps. To identify the activity determining step and the relative OER activity of considered surfaces, the reaction free-energies are computed from the Gibbs free-energy at standard conditions (T = 298 K, P_{H2} = 1 bar and pH = 0), and defined as

$\Delta G = \Delta G_0 + \Delta G(U)$

where $\Delta G_0 = \Delta E + \Delta E_{ZPE} - T\Delta S$ where ΔE, ΔE_{ZPE} and $T\Delta S$ are the DFT reaction energy (computed using H_2 and H_2O as reference), difference in the zero-point energies and entropic contribution obtained from standard tables for the gas phase molecules, respectively. With this approach, the reaction free energies of the four elementary reduction steps (3.1-3.4) can be readily computed (ΔG_1, ΔG_2, ΔG_3, ΔG_4). The corresponding standard equilibrium potential values of each step, U_i^0, is shown in Fig. 3.5 for the various considered surfaces.

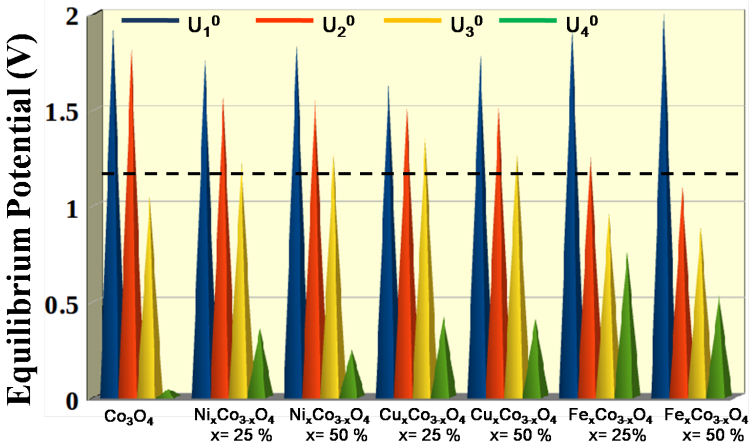

Figure 3.5: Standard equilibrium potential for reaction steps 3.1-3.4 at surface sites of pure and doped Co_3O_4 surfaces. The black dashed line is the equilibrium potential of the overall oxidation reaction (1.23 V)

Here it is important to note that total free energy of the OER process is kept fixed at ΔG = 4.92 eV. For the optimal catalyst, this energy is equally divided among the four charge transfer processes and ideally, the free energies of the individual step should be 1.23 eV. The reaction step with the highest (most positive) value for the standard equilibrium potential is the thermodynamically least favourable one in the OER process and termed as potential determining step. Assuming this definition, it can be seen from the Figure 3.4 that in all the investigated case, oxidation of H_2O to $^*OH$ requires largest free energy change among all the four elementary processes. Formation of O^* is found to the second elementary step with the highest change in free energy.

The theoretical overpotential of the fuel cell is defined as difference between the highest potential where all the steps become downhill in free energy and equilibrium potential of OER process per step (U_0 = 4.92/4 = 1.23 V). It is found that the overpotential is highly dependent on the dopant and the doping concentration in the following order: $Fe_xCo_{3-x}O_4$ (x = 50 %) (0.77 V) > Pure Co_3O_4 (0.76 V) $Fe_xCo_{3-x}O_4$ (x = 25 %) (0.69 V) > $Ni_xCo_{3-x}O_4$ (x = 50 %) (0.61 V) > $Cu_xCo_{3-x}O_4$ (x = 50 %) (0.56 V) > $Ni_xCo_{3-x}O_4$ (x = 25 %) (0.53 V) > $Cu_xCo_{3-x}O_4$ (x = 25 %) (0.41 V). Thus, from the trend in overpotential values, it can be seen that higher substitution shows little effect towards OER activity with respect to pure Co_3O_4. It is to be noted that, in consistent with the experimental finding, the theoretical overpotential of pure Co_3O_4 is approximately 0.3 V higher than that of RuO_2 (0.4 V), [26] one of the best OER catalyst so far. This also agrees well with the DFT+U study by Norskov et al. and validates our model.[19]

3.3.4 Activity Volcano Plot

The electrocatalytic activity of OER at zero bias can be measured as negative change of the free energy, -ΔG and that is directly related to the rate of the reaction, r(U) = exp[-(ΔG(0) - eU)/KT]. Fig. 3.6 shows the plotting of maximum rate or, equivalently, the minimum -ΔG(0), for each of the individual elementary steps as a function of the independent variable, ΔG_{*OH}.

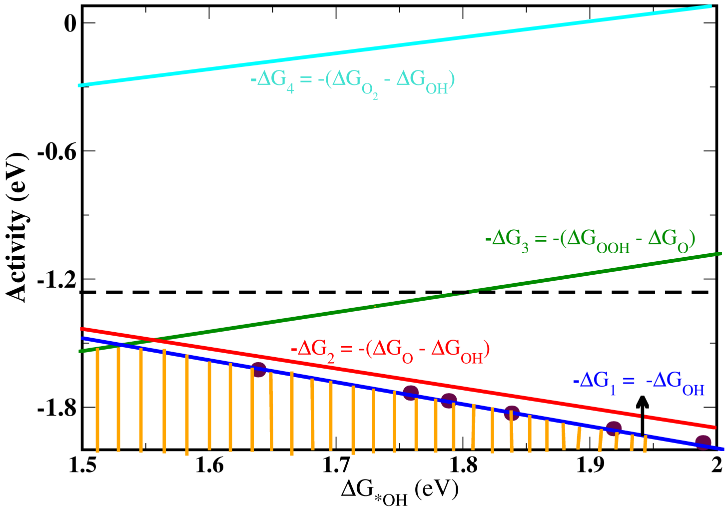

Figure 3.6: Activity volcano relation for OER activity as a function of binding energy of *OH at surface sites of various doped Co_3O_4 Magenta data points are the activity of the potential-determining steps. The resulting volcano is indicated with the hatched area.

As mentioned earlier, the activity volcano curve also predict the formation of *OH as potential determining step which is found at weak *OH binding leg. (with relatively positive $\Delta\ G_{*OH}$) (Figure 3.5) The comparable activity for the subsequent formation of *O from the oxidation of *OH implies that OER activity should not only be determined by single step. Evidently, according to the Sabbatier Principle, the lowest OER overpotential can be achieved at an intermediate *OH adsorption strength i.e., at the volcano top. However, in the present case, the 25% Cu doped Co_3O_4 is found to be the best achievable catalyst, close to the very top of the activity volcano curve. Our theoretical analysis indicates that material that binds *OH much stronger than the 25% Cu-doped Co_3O_4 is anticipated to have a better catalytic activity since it will reach closer to the volcano top. Correspondingly, the material would need lower potential for water splitting. Though more detailed models are required to reach the conclusion of the OER activity, our study gives a comparison among the pure and doped Co_3O_4 from the same frame of reference.

3.4 Conclusion

In summary, our results provide a systematic framework for predicting the reactivity of transition metal substituted Co_3O_4. An increase in the catalytic activity for OER of Co_3O_4 has been achieved by doping with Fe, Ni and Cu. For all the cases, first step, i.e., $H_2O \rightarrow {}^*OH$ is found to be the rate limiting step. According to our study, 25% Cu substituted Co_3O_4 shows the best catalytic activity. Moreover, we find that the reactivity of OER significantly depends on dopant concentration. On the basis of these findings, we would expect that our work will aid in the design of improved OER electrocatalysts.

Bibliography

[1] M. G. Walter, E. L. Warren, J. R. McKone, S. W. Boettcher, Q. Mi, E. A. Santori and N. S. Lewis, *Chem. Rev.*, 2010, **110**, 6446–6473.

[2] J. O. Bockris, *Int. J. Hydrogen Energy*, 2008, **33**, 2129 – 2131.

[3] T. R. Cook, D. K. Dogutan, S. Y. Reece, Y. Surendranath, T. S. Teets and D. G. Nocera, *Chem. Rev.*, 2010, **110**, 6474–6502.

[4] M. S. Burke, S. Zou, L. J. Enman, J. E. Kellon, C. A. Gabor, E. Pledger and S. W. Boettcher, *J. Phys. Chem. Lett.*, 2015, **6**, 3737–3742.

[5] A. Valdes, J. Brillet, M. Gratzel, H. Gudmundsdottir, H. A. Hansen, H. Jonsson, P. Klupfel, G.-J. Kroes, F. Le Formal, I. C. Man, R. S. Martins, J. K. Norskov, J. Rossmeisl, K. Sivula, A. Vojvodic and M. Zach, *Phys. Chem. Chem. Phys.*, 2012, **14**, 49–70.

[6] J. Chen and A. Selloni, *J. Phys. Chem. C*, 2013, **117**, 20002–20006.

[7] M. Bajdich, M. Garcia-Mota, A. Vojvodic, J. K. Norskóv and A. T. Bell, *J. Am. Chem. Soc.*, 2013, **135**, 13521–13530.

[8] J. Rosen, G. S. Hutchings and F. Jiao, *J. Am. Chem. Soc.*, 2013, **135**, 4516–4521.

[9] C. P. Plaisance and R. A. van Santen, *J. Am. Chem. Soc.*, 0, **0**, null.

[10] I. Nikolov, R. Darkaoui, E. Zhecheva, R. Stoyanova, N. Dimitrov and T. Vitanov, *J. Electroanal. Chem.*, 1997, **429**, 157 – 168.

[11] R. Singh, J. Pandey, N. Singh, B. Lal, P. Chartier and J.-F. Koenig, *Electrochim. Acta*, 2000, **45**, 1911 – 1919.

[12] I. Abidat, N. Bouchenafa-Saib, A. Habrioux, C. Comminges, C. Canaff, J. Rousseau, T. W. Napporn, D. Dambournet, O. Borkiewicz and K. B. Kokoh, *J. Mater. Chem. A*, 2015, **3**, 17433–17444.

[13] T. Grewe, X. Deng and H. Tysz, *Chem. Mater.*, 2014, **26**, 3162–3168.

[14] X. Tong, X. Xia, C. Guo, Y. Zhang, J. Tu, H. J. Fan and X.-Y. Guo, *J. Mater. Chem. A*, 2015, **3**, 18372–18379.

[15] Y. Zhang, B. Cui, C. Zhao, H. Lin and J. Li, *Phys. Chem. Chem. Phys.*, 2013, **15**, 7363–7369.

[16] M. S. Burke, M. G. Kast, L. Trotochaud, A. M. Smith and S. W. Boettcher, *J. Am. Chem. Soc.*, 2015, **137**, 3638–3648.

[17] P. Giannozzi, S. Baroni, N. Bonini, M. Calandra, R. Car, C. Cavazzoni, D. Ceresoli, G. L. Chiarotti, M. Cococcioni, I. Dabo, A. Dal Corso, S. de Gironcoli, S. Fabris, G. Fratesi, R. Gebauer, U. Gerstmann, C. Gougoussis, A. Kokalj, M. Lazzeri, L. Martin-Samos, N. Marzari, F. Mauri, R. Mazzarello, S. Paolini, A. Pasquarello, L. Paulatto, C. Sbraccia, S. Scandolo, G. Sclauzero, A. P. Seitsonen, A. Smogunov, P. Umari and R. M. Wentzcovitch, *J. Phys.: Condens. Matter*, 2009, **21**, 395502.

[18] J. P. Perdew, K. Burke and M. Ernzerhof, *Phys. Rev. Lett.*, 1996, **77**, 3865–3868.

[19] M. Garcia-Mota, M. Bajdich, V. Viswanathan, A. Vojvodic, A. T. Bell and J. K. N. rskov, *J. Phys. Chem. C*, 2012, **116**, 21077–21082.

[20] H. J. Monkhorst and J. D. Pack, *Phys. Rev. B*, 1976, **13**, 5188–5192.

[21] J. K. Norskov, J. Rossmeisl, A. Logadottir, , L. Lindqvist, J. R. Kitchin, T. Bligaard and H. Jonsson, *J. Phys. Chem. B*, 2004, **108**, 17886–17892.

[22] J. Chen and A. Selloni, *J. Phys. Chem. Lett.*, 2012, **3**, 2808–2814.

[23] J. Rossmeisl, A. Logadottir and J. Nrskov, *Chem. Phys.*, 2005, **319**, 178 – 184.

[24] J. Rossmeisl, Z.-W. Qu, H. Zhu, G.-J. Kroes and J. Nrskov, *J. Electroanal. Chem.*, 2007, **607**, 83 – 89.

[25] I. C. Man, H.-Y. Su, F. Calle-Vallejo, H. A. Hansen, J. I. Martnez, N. G. Inoglu, J. Kitchin, T. F. Jaramillo, J. K. Nrskov and J. Rossmeisl, *ChemCatChem*, 2011, **3**, 1159–1165.

[26] Y. Matsumoto and E. Sato, *Mater. Chem. Phys.*, 1986, **14**, 397 – 426.

Chapter 4

Methane formation from the hydrogenation of Carbon dioxide on Ni (110) surface - A Density Functional Theoretical Study

Contents

4.1 Introduction

The shrinking fossil fuel resources are one of the major problems in the current world, which are forcing us to re-evaluate the efficient utilization or finding alternative energy resources [1–3]. This has been a very active area of research since long, which indeed requires contributions from experimentalists as well as theorists [4–13]. CO_2 is one of the abundant gas present in earth atmosphere (390 ppm by volume) [14], which is produced in enormous quantity by natural (volcanic eruption, hot springs, geysers and during the respiration process of animals and humans, to name a few) and manmade resources (combustion of fuels and fermentation of liquids etc.). Hence, the development of proper strategies for the utilization of CO_2 could be the solution for the recent energy crisis. Much research has been devoted to explore the recycling process of carbon dioxide into either high energy content fuels [15–17] or industrially important compounds [16, 18–20].

Among these, hydrogenation processes have been proposed to be an effective method for the utilization of CO_2 [21–34]. Many products and intermediates are produced during this process, such as methanol, carbon monoxide, formic acid, methane or higher alkanes. Types of products can be chosen by tuning the reaction thermodynamics and kinetic parameters [35–37]. The direct hydrogenation of CO_2 without catalysis entails energy of -31.26 kcal mol^{-1} at 298 K, which is thermodynamically favorable. But, the requirement of eight electrons makes this process kinetically unfavorable. To overcome this kinetic hurdle, catalysts are generally used. In practice, the surface catalysts on the various VIIIA and IB group transition metal surfaces are considered to be appropriate for this reaction [38–40]. Among them, nickel is one of the most effective and cheapest surface catalysts for the hydrogenation reaction, due to the presence of easily transferable electrons in its frontier d orbital. A series of Ni surfaces such as (110), (100), (111), (211) have been used as catalysts for the hydrogenation reaction and it has been found that Ni(110) is more effective than other surfaces [41, 42]. This is due to the higher intensity of the occupied orbital in the Fermi level of Ni(110) than other nickel surfaces. To date, plenty of experimental [35–37] ,[42–48] and theoretical studies [49–53] have been proposed on the chemisorption of CO_2 on Ni(110) surface. However, formation of the various compounds in appreciable amounts is yet to be achieved and needs complete understanding of the underlying mechanism. Tracking the mechanism using the available experimental techniques would be very hard. Computational and theoretical studies may help in this regard.

Experimentally, CO_2 hydrogenation reactions have been studied on Ni surface using steady state kinetics (SSK), [36] chemical transient kinetics (CTK),[37] X-ray photoelectron spectroscopy (XPS) [35, 54] and high pressure temperature programmed reaction (TPR) techniques. Each study leads to different intermediates which suggest many pathways for a single reaction. The hydrogenation process after the decomposition of adsorbed CO_2 to CO + O had been proposed, based on the steady state kinetic studies. CTK study finds the H-assisted EleyRideal (ER) and Langmuir Hinshelwood (LH) CO_2 hydrogenation mechanism, where the intermediates can either be stable formate ion or active hydroxyl carbonyl. However, the technical difficulties in these experiments make them difficult to understand the complete pathway.

A few theoretical studies have been devoted to understand the binding modes of hydrogen, carbon dioxide (ER) or both together (LH) on the Ni(110) surface. Previous theoretical studies show that the CO_2 angle changes from $\angle 180^0$ by accepting an electron from nickel and forms maximum coordination with the Ni surface, whereas H_2 adsorbs dissociatively on the nickel surface. Moreover, the barrier for the formation of CO (13.84 kcal mol^{-1}), formate (9.92 kcal mol^{-1}) and hydroxyl carbonyl (2.77 kcal mol^{-1}) intermediates have been proposed theoretically. [35, 37, 51] However, though the intermediates occurring after the first hydrogenation reactions are reported [35, 37], their roles in the subsequent reaction steps have not been explored. The aim of this work is to systematically understand all possible reaction pathways for the complete hydrogenation reactions from the stable intermediates.

4.2 Computational methods

The hydrogenation mechanism on Ni(110) surface is studied using the PWSCF (Plane-Wave Self-Consistent Field) code within the generalized gradient approximation (GGA) and PerdewBurkeErnzerhof (PBE) functional as implemented in the QUANTUM ESPRESSO Package [55]. The plane wave basis set of 0.01 Ryd MarzariVanderbilt smearing was used to describe valence electrons with a kinetic energy cutoff up to 24 Ryd. Ionic cores are described by the ultrasoft pseudopotential. Surfaces are described as extended systems using 2×2 periodically repeated supercells with slab geometry. A $3 \times 3 \times 1$ k-point mesh is used. The vacuum between the slabs are set to span a range of 12 Åto make sure of no significant interaction between the slabs. The following convergence criteria are used for structure optimization and energy calculations: difference of the total energies of last two consecutive steps is less than 10^{-6} Ryd and total force is less than 0.002 Ryd Bohr^{-1}. The computations are carried out by considering Ni(110) slab thickness of four layers, where the top two layers were relaxed and the bottom two were kept fixed. Similarly, the computed lattice constant, 3.54 with $3 \times 3 \times 1$ k-point mesh is in good agreement with experimental value (3.52 Ang). These results validate our model. The Climbing Image Nudged Elastic Band method [56] has been used to determine the energy barrier of the transition state in the surface, which has been proven to be an appropriate technique for several complex chemical reactions. The binding energies (E$_{BE}$) are computed for the reaction, $A + B \rightarrow AB$ as follows,

$$E_{BE} = E_{AB} - (E_A + E_B) \tag{4.1}$$

Where E_{AB} and $E_{A/B}$ are the total energies of the product and reactants respectively. Relative energy barriers reported in this work are calculated with reference to the Ni(110) surface, free from CO_2 and H_2 entities in order to compare various pathways with one single reference.

4.3 Results and discussions

4.3.1 CO_2 hydrogenation mechanism

Though methanation of CO_2 apparently seems to be a simple reaction (see eqn (4.2)), there is more than one pathway that may lead to the product (eqn (4.3) and (4.4)), as given below,

$$CO_2 + 4H_2 \rightarrow CH_4 + 2H_2O \tag{4.2}$$

$$CO_2 \rightarrow CO + O \rightarrow CH_4 + 2H_2O \tag{4.3}$$

$$CO_2 + H_2 \rightarrow HCOOH \rightarrow HCOO + H \rightarrow CH_4 + 2H_2O \tag{4.4}$$

The reaction passes through many complicated intermediates and many paths. In order to simplify the mechanisms, step by step assessments of the various pathways have been given in the following section. Three starting intermediates have been evaluated depending upon the experimental conditions, which are given in Fig. 4.1.

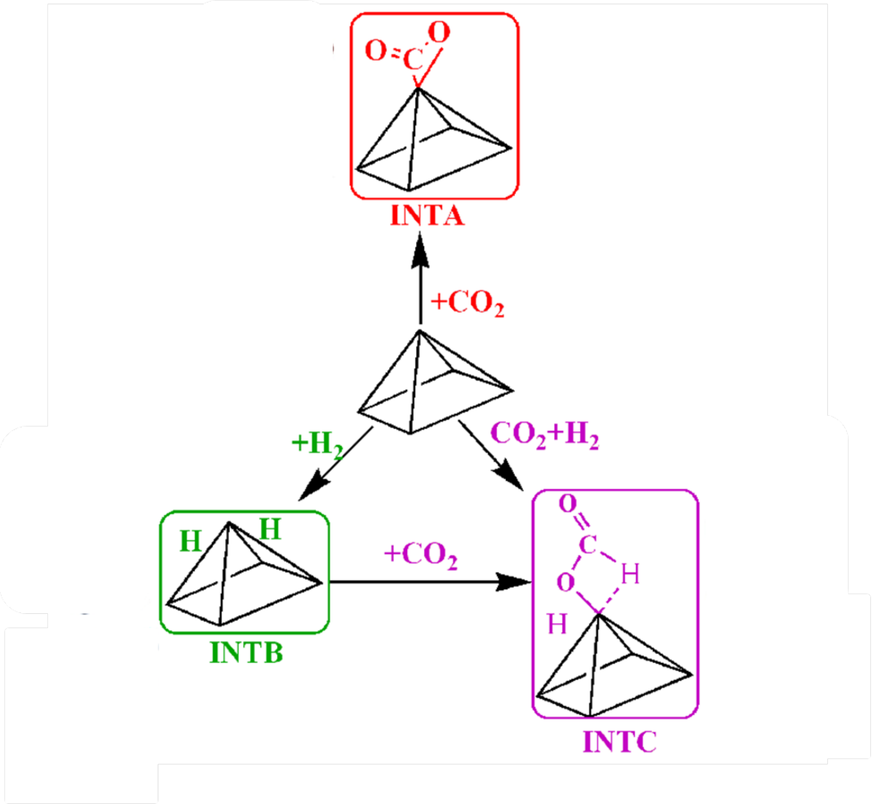

Figure 4.1: Schematic representation of chemisorptions of H_2 or/and CO_2 on Ni(110) surface

In this work, the possibilities of both ER and LH mechanistic pathways have been explored. The reaction starts by adsorbing either CO_2 or H_2 or both together on the Ni(110) surface and leads to three different intermediates, which are labeled as INTA, INTB and INTC. In INTA, CO_2 binds to Ni(110) surface with $\angle 121.51^0$ and is coordinated through oxygen and carbon atoms with the bond lengths of 2.00 Åand 1.87 Ådistances, respectively. In the second case (INTB), the hydrogen molecule is absorbed in a dissociative manner on the Ni(110) surface catalyst with NiH distances of 1.61Åand 1.72Å. In the final case, the co-adsorption of H_2 and CO_2 moieties is considered, which yields formate (INTC), and the other hydrogen atom is adsorbed on the surface (LH mechanism). The same intermediate is also obtained from the reaction between pre-adsorbed hydrogen molecule and CO_2 gas with the barrier of 9.33 kcal mol^{-1} (ER mechanism). This barrier is smaller than the barrier obtained for the formation of INTC from INTA and gas phase H_2 molecule (12.5 kcal mol^{-1}). The computed binding energies for co-adsorbed formate moiety (19.21 kcal mol^{-1}, INTC) is higher than for CO_2 (12.87 kcal mol^{-1}, INTA) and H_2 (9.12 kcal mol^{-1}, INTB) on the Ni(110) surface. And also the computed normal mode values for all the three intermediates on the smaller cluster are quite comparable with the corresponding High Resolution Electron Energy Loss (HREEL) spectroscopic values. [35] However, various experimental studies suggested the possibility of formation of both intermediates, INTA and INTC, in certain initial circumstances (kinetic and thermodynamic conditions). Hereafter, we have concentrated on the possible pathways starting from intermediates INTA and INTC. Note that the pre-adsorbed H_2 (INTB) reacts with CO_2 and results in the formate (INTC) intermediate.

4.3.2 Hydrogenation mechanism via INTA

DFT studies provide evidence that hydrogenation can occur only on the oxygen atoms of the CO_2 rather than the C atom in $Ni-CO_2$ (INTA) moiety as shown in Fig. 4.2.

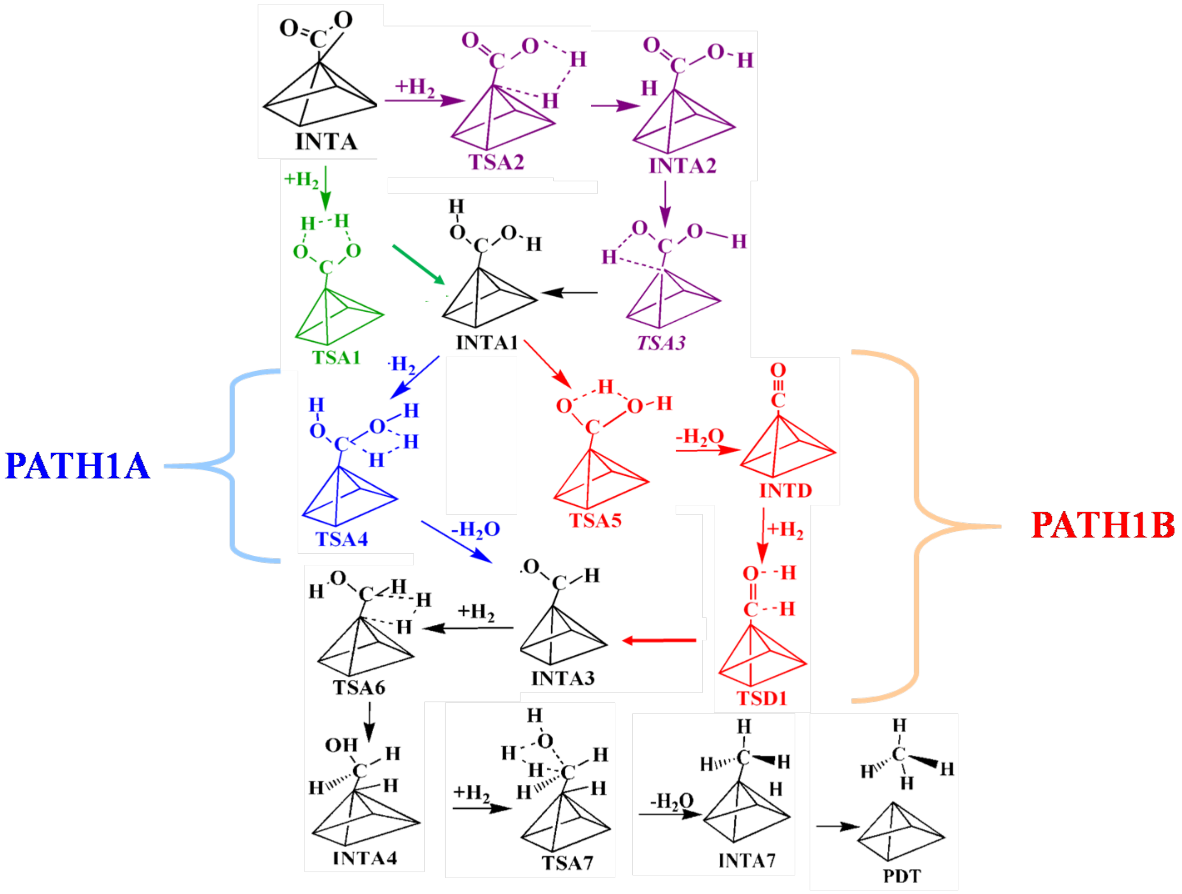

Figure 4.2: Schematic representations of possible pathways for the formation of methane from INTA. Ni(110) surface represented as distorted square geometry in order to show the bonding modes clearly

The first hydrogenation can take place either in a single step (via TSA1) or in two steps (via TSA2 and TSA3) to yield a dihydroxy intermediate (INTA1). Stepwise hydrogenation occurs via hydroxyl carbonyl (INTA2) intermediate, which requires 3.2 kcal mol^{-1} (for TSA2) and 4.73 kcal mol^{-1} (for TSA3) less energy than the concerted pathway, 29.42 kcal mol^{-1} (for TSA1), which shows the higher possibility of stepwise mechanism for first hydrogenation (given in Fig. 4.3)

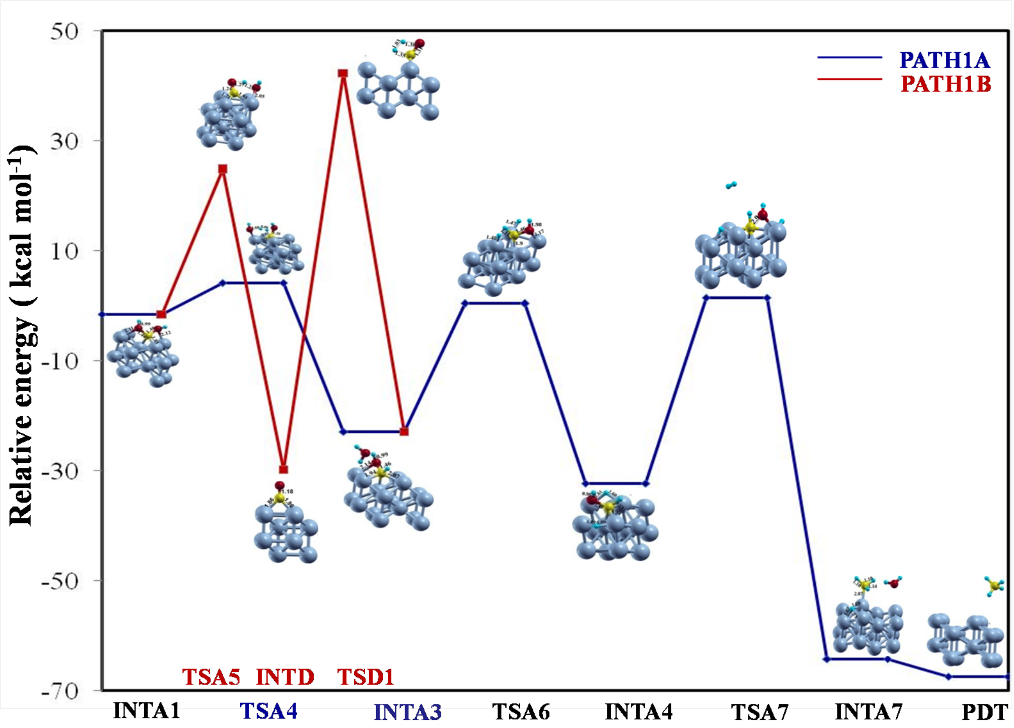

Figure 4.3: Relative energy barriers on Ni(110) surface for the pathways shown in Fig. 4.2

Table 4.1: Relative energy barriers (ΔE in kcal mol^{-1}) on Ni(110) surface for the pathways (PATH1A, PATH1B, PATH2A, and PATH2B). Blue and red lines correspond to PATH1A and PATH1B, respectively.

Species	ΔE	Species	ΔE
Nickel	0.00	INTB	-9.12
INTA	-12.87	INTC	-19.21
TSA1	29.42	TSC1	-8.46
INTA1	-1.51	INTC1	-18.93
TSA4	4.13	TSC2	4.13
INTA3	-22.83	INTC2	-26.58
TSA6	0.42	TSC3	5.86
INTA4	-32.26	INTC3	-25.74
TSA7	1.55	TSC4	-11.90
INTA7	-64.18	TSC4A	-10.10
TSA2	3.2	INTC4	-18.02
INTA2	-3.22	TSC5	23.49
TSA3	4.73	INTC5	-31.97
TSA5	24.78	INTC6	-47.68
INTD	-29.73	-	-
TSD1	42.29	-	-
PDT	-67.39	-	-

It has been already proven that the monohydroxyl carbonyl intermediate (INTA2) can easily be converted to formate (INTC) with a barrier of 9.22 kcal mol^{-1}. [37] However, this experiment did not account for subsequent reaction steps from highly stable formate intermediate (INTC). [37] Hence, we have considered the hydrogenation via dihydroxyl intermediate (INTA1) first, as shown in Fig. 4.2. Nevertheless, the hydrogenation via formate intermediate (INTC) has been studied in the latter section. The computed complete relative energy barriers (see Table 4.1) with the optimized geometries are shown in Fig. 4.3

The dihydroxy intermediate (INTA1) can release a water molecule and form INTA3 via two bifurcated pathways, which are designated as PATH1A (water removal via instantaneous addition of H_2 molecule) and PATH1B (addition of H_2 after the formation of CO). PATH1A passes through TSA4 with 4.13 kcal mol^{-1} to reach the species INTA3 while PATH1B goes through TSA5 (24.78 kcal mol^{-1}), TSD1 (42.29 kcal mol^{-1}) to attain INTA3 (-22.83 kcal mol^{-1}). The INTD (CO) intermediate plays an important role and had been observed as one of the stable species in the Temperature Programmed (TPD) and HREEL spectroscopic studies. [37] Moreover, it has been proven that the CO hydrogenation can yield higher alkanes along with methane. [57] Our calculation shows that the CO intermediate (INTD) is more stable than the CO_2 intermediate (INTA) by 22.83 kcal mol^{-1}. However, in the present study, formation of CO via TSA5 needs higher energy barrier (24.78 kcal mol^{-1}) and further the stable CO moiety also requires huge (42.29 kcal mol^{-1}) energy in order to form monohydroxyl (INTA3) entity. Moreover, we have also checked the possible formation of free carbon from INTD which requires much more energy

(56.3 kcal mol^{-1}) than the formation of hydroxyl intermediate. In addition, the possibility for the direct hydrogenation of C atom in CO (INTD) moiety has been explored and that also requires huge energy (68 kcal mol^{-1}). This proves that the pathways along the oxygen containing intermediate (INTA3) are more feasible than the carbon containing intermediate as observed in the CTK experiment. [57] The complex (INTA3) subsequently passes through TSA6 (0.42 kcal mol^{-1}), INTA4 (-32.26 kcal mol^{-1}), TSA7 (1.55 kcal mol^{-1}), INTA7 (-64.18 kcal mol^{-1}) states and finally results in the product methane (see Fig. 4.3). Interestingly, INTA7 is methyl group where the carbon is coordinated to the Ni surface with the average distance of 2.3 ÅThis leaves room for the production of higher alkanes as found in a few experiments. [57] Overall, these results illustrate that PATH1A entails less energy than PATH1B (see Fig. 4.3).

4.3.3 Hydrogenation of INTC (formate)

As mentioned before, formate (INTC) is another possible intermediate and can be formed from INTA2, INTB and INTA intermediates, and via both ER and LH mechanisms. The second molecular hydrogen addition occurs with a barrier of 8.46 kcal mol^{-1} and leads to INTC1. This (INTC1) follows two pathways, PATH2A and PATH2B resulting in methoxy intermediate (INTC4) (see Fig. 4.4). In PATH2A, INTC1 goes via TSC3 with a barrier height of 5.86 kcal mol^{-1} to form INTC3, while in PATH2B, it requires 4.13 kcal mol^{-1} to form INTC2.

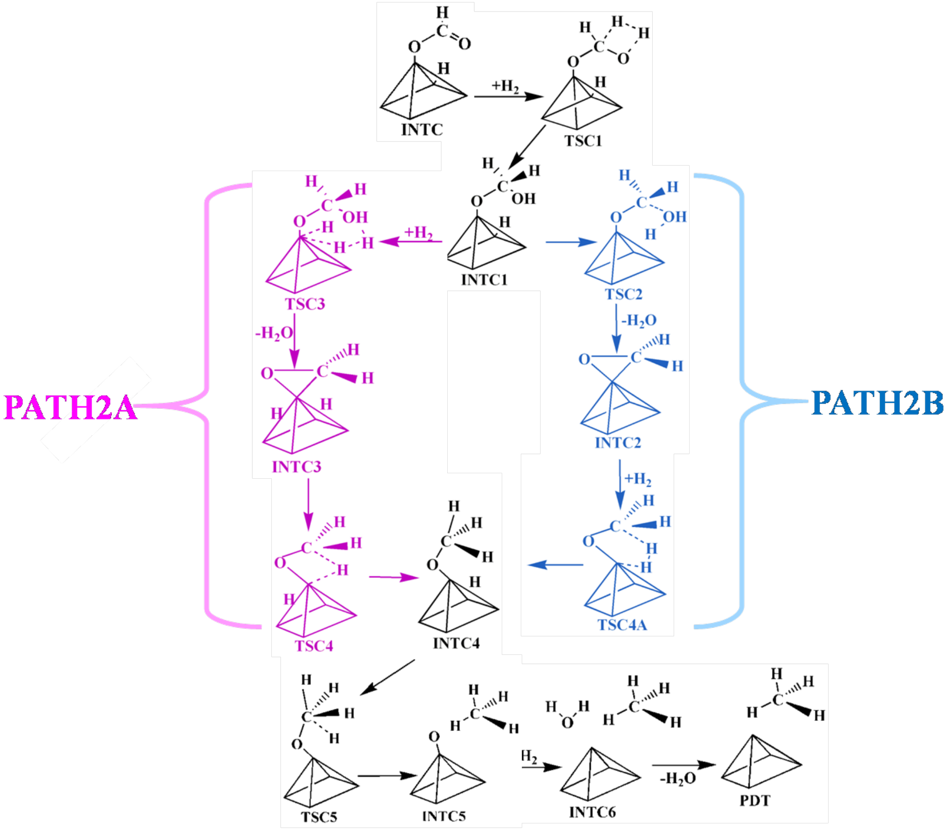

Figure 4.4: Schematic representations of all possible pathways for the formation of methane from INTC via hydrogenation reactions. The Ni(110) surface is represented as distorted square geometry in order to show the bonding modes clearly

The methoxy intermediate forms methane via TSC5 (23.49 kcal mol^{-1}) and leaves oxygen on the nickel catalyst, which is in agreement with the observation of oxygen content in the nickel catalyst in the CTK experiment. As a result, conversion of methoxy to methane becomes the rate determining step. And the formation of methane leaves free oxygen on the surface (INTC5).The corresponding relative free energy profiles are shown in Fig. 4.5 and given in Table 4.1

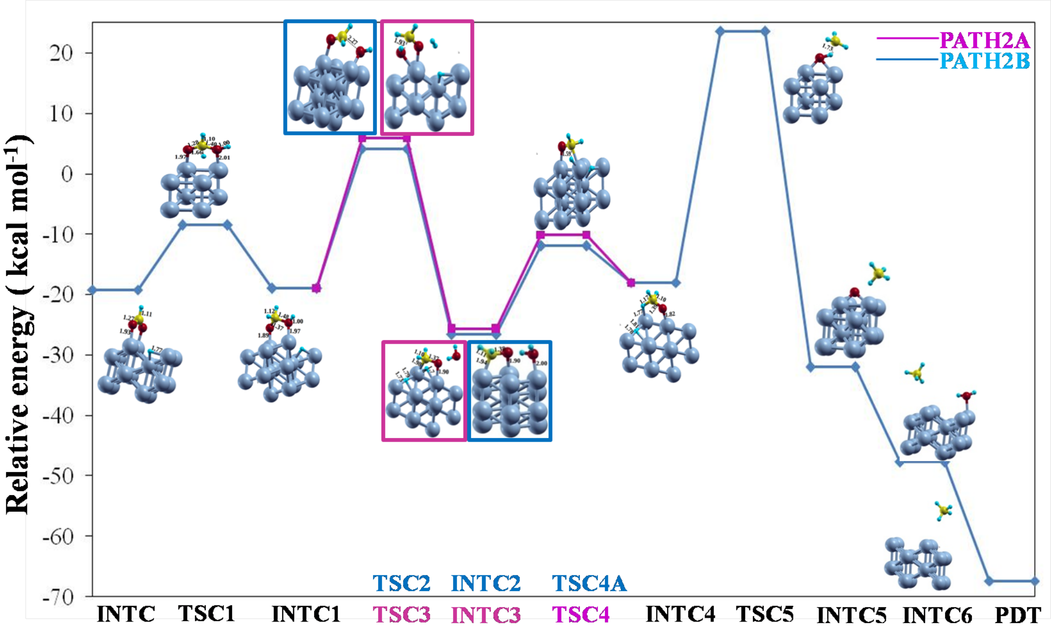

Figure 4.5: Relative energy barriers on Ni(110) surface for the pathways shown in Fig. 4.4

4.4 Conclusions

DFT calculations have been performed to understand the complete hydrogenation mechanisms for CO_2 on Ni(110) surface. Our calculations show that the CO_2 hydrogenation passes via various stable intermediates, namely, carbon monoxide, methoxy, formate and yield the product methane, as observed in various experiments. Our studies show that all three stable (formate (INTC), CO_2 (INTA) or CO (INTD)) intermediates can be hydrogenated to produce methane. The INTA follows PATH1A (4.13 kcal mol^{-1}) or PATH1B (42.29 kcal mol^{-1}) to yield the desired product, where the carbon coordination mode is observed throughout the pathways. On the other hand, the INTC proceeds via PATH2A (5.86 kcal mol^{-1}) or PATH2B (4.13 kcal mol^{-1}) to reach the methoxy product with consistent ‘oxygen ’coordination mode. Further, methoxy to methane conversion requires 23.49 kcal mol^{-1} energy. In short, we find that the CO hydrogenation (PATH1B) needs the highest energy than the other three pathways (PATH1A, PATH2A and PATH2B). Finally, among the four pathways, PATH1A requires less energy than other pathways.

Bibliography

[1] R. York, *Nature Climate Change*, 2012, **2**, 441–443.

[2] S. T. S. M. Raj and L. P. Christopher, *BioEnergy Res.*, 2012, **5**, 515–531.

[3] A. D. B. C. Jiang, J. Ma and J. T. S. Irvine, *Energy Environ. Sci.*, 2012, **5**, 6973–6980.

[4] F. P. E. Scott and J. Sanders, *Appl. Microbiol. Biotechnol.*, 2007, **75**, 751–762.

[5] Y. Amao, *ChemCatChem*, 2011, **3**, 458–474.

[6] N. Armaroli and V. Balzani, *Chemistry An Asian Journal*, 2011, **6**, 768–784.

[7] K. Yu, I. Curcic, J. Gabriel and S. Tsang, *ChemSusChem*, 2008, **1**, 893–899.

[8] J. Kim, C. A. Henao, T. A. Johnson, D. E. Dedrick, J. E. Miller, E. B. Stechel and C. T. Maravelias, *Energy Environ. Sci.*, 2011, **4**, 3122–3132.

[9] K. G. Steinhäuser, S. Richter, P. Greiner, J. Penning and M. Angrick, *Environmental Science and Pollution Research*, **11**, 284–290.

[10] K. Hein and J. Bemtgen, *Fuel Processing Technology*, 1998, **54**, 159–169.

[11] N. V. Gnanapragasam, B. V. Reddy and M. A. Rosen, *International Journal of Hydrogen Energy*, 2010, **35**, 4788–4807.

[12] D. Mignard and C. Pritchard, *International Journal of Hydrogen Energy*, 2007, **32**, 5039–5049.

[13] V. L. K. Z. Jiang, T. Xiao and P. P. Edwards, *Philos.Trans. R. Soc. A*, 2010, **368**, 3343–3364.

[14] T. Conway and P. Tans, *Philos.Trans. R. Soc. A*, 2012.

[15] H. Yang, Z. Xu, M. Fan, R. Gupta, R. B. Slimane, A. E. Bland and I. Wright, *Journal of Environmental Sciences*, 2008, **20**, 14–27.

[16] A. Baiker, *Applied Organometallic Chemistry*, 2000, **14**, 751–762.

[17] G. Centi and S. Perathoner, *Carbon Dioxide Utilization for Global Sustainability Proceedings of 7th International Conference on Carbon Dioxide Utilization*, Elsevier, 2004, vol. 153, pp. 1–8.

[18] W. C. Chueh, C. Falter, M. Abbott, D. Scipio, P. Furler, S. M. Haile and A. Steinfeld, *Science*, 2010, **330**, 1797–1801.

[19] J. Ma, N. Sun, X. Zhang, N. Zhao, F. Xiao, W. Wei and Y. Sun, *Catalysis Today*, 2009, **148**, 221–231.

[20] C. Song, *Catalysis Today*, 2006, **115**, 2–32.

[21] . Hironori Arakawa, . Michele Aresta, . John N. Armor, . Mark A. Barteau, . Eric J. Beckman, . Alexis T. Bell, . John E. Bercaw, . Carol Creutz, . Eckhard Dinjus, . David A. Dixon, . Kazunari Domen, . Daniel L. DuBois, . Juergen Eckert, . Etsuko Fujita, . Dorothy H. Gibson, . William A. Goddard, . D. Wayne Goodman, . Jay Keller, . Gregory J. Kubas, . Harold H. Kung, . James E. Lyons, . Leo E. Manzer, . . Tobin J. Marks, . Keiji Morokuma, . Kenneth M. Nicholas, . Roy Periana, . Lawrence Que, . Jens Rostrup-Nielson, . Wolfgang M. H. Sachtler, . Lanny D. Schmidt, . Ayusman Sen, . Gabor A. Somorjai, . Peter C. Stair, . B. Ray Stults, and W. Tumas, *Chemical Reviews*, 2001, **101**, 953–996.

[22] M. Aresta and A. Dibenedetto, *Dalton Trans.*, 2007, 2975–2992.

[23] E. E. Benson, C. P. Kubiak, A. J. Sathrum and J. M. Smieja, *Chem. Soc. Rev.*, 2009, **38**, 89–99.

[24] G. Centi and S. Perathoner, *Catalysis Today*, 2009, **148**, 191–205.

[25] Daniela Belli Dell'Amico, . Fausto Calderazzo, Luca Labella, Fabio Marchetti, and G. Pampaloni, *Chemical Reviews*, 2003, **103**, 3857–3898.

[26] P. G. Jessop, F. Joó and C.-C. Tai, *Coordination Chemistry Reviews*, 2004, **248**, 2425–2442.

[27] M. R. Kember, A. Buchard and C. K. Williams, *Chem. Commun.*, 2011, **47**, 141–163.

[28] Y.-W. L. Y.-Y. X. J.-L. Z. Wen-Ping Ma, Yu-Long Zhao, *React.Kinet. Catal. Lett.*, 1999, **66**, 217–223.

[29] M. Mikkelsen, M. Jorgensen and F. C. Krebs, *Energy Environ. Sci.*, 2010, **3**, 43–81.

[30] I. Omae, *Catalysis Today*, 2006, **115**, 33–52.

[31] S. N. Riduan and Y. Zhang, *Dalton Trans.*, 2010, **39**, 3347–3357.

[32] . Toshiyasu Sakakura, Jun-Chul Choi, and H. Yasuda, *Chemical Reviews*, 2007, **107**, 2365–2387.

[33] T. Sakakura and K. Kohno, *Chem. Commun.*, 2009, 1312–1330.

[34] D. T. Whipple and P. J. A. Kenis, *The Journal of Physical Chemistry Letters*, 2010, **1**, 3451–3458.

[35] E. Vesselli, L. D. Rogatis, X. Ding, A. Baraldi, L. Savio, L. Vattuone, M. Rocca, P. Fornasiero, M. Peressi, A. Baldereschi, R. Rosei and G. Comelli, *Journal of the American Chemical Society*, 2008, **130**, 11417–11422.

[36] E. Vesselli, J. Schweicher, A. Bundhoo, A. Frennet and N. Kruse, *The Journal of Physical Chemistry C*, 2011, **115**, 1255–1260.

[37] E. Vesselli, M. Rizzi, L. D. Rogatis, X. Ding, A. Baraldi, G. Comelli, L. Savio, L. Vattuone, M. Rocca, P. Fornasiero, A. Baldereschi and M. Peressi, *The Journal of Physical Chemistry Letters*, 2010, **1**, 402–406.

[38] . Sheng-Guang Wang, . Xiao-Yuan Liao, . Dong-Bo Cao, . Chun-Fang Huo, . Yong-Wang Li, . Jianguo Wang, and . . Haijun Jiao*, *The Journal of Physical Chemistry C*, 2007, **111**, 16934–16940.

[39] J. Liu, C. Guo, Z. Zhang, T. Jiang, H. Liu, J. Song, H. Fan and B. Han, *Chem. Commun.*, 2010, **46**, 5770–5772.

[40] D. Jagadeesan, M. Eswaramoorthy and C. Rao, *ChemSusChem*, 2009, **2**, 878–882.

[41] . Sheng-Guang Wang, . Dong-Bo Cao, . Yong-Wang Li, . Jianguo Wang, and . . Haijun Jiao*, *The Journal of Physical Chemistry B*, 2005, **109**, 18956–18963.

[42] D.-B. Cao, Y.-W. Li, J. Wang and H. Jiao, *Surface Science*, 2009, **603**, 2991–2998.

[43] M. Ackermann, O. Robach, C. Walker, C. Quiros, H. Isern and S. Ferrer, *Surface Science*, 2004, **557**, 21–30.

[44] M. Agnelli, M. Kolb and C. Mirodatos, *Journal of Catalysis*, 1994, **148**, 9–21.

[45] M. T. Duignan, E. Grunwald and S. Speiser, *The Journal of Physical Chemistry*, 1983, **87**, 4387–4394.

[46] . Martin P. Rohde, Dominik Unruh, and G. Schaub, *Industrial & Engineering Chemistry Research*, 2005, **44**, 9653–9658.

[47] . Jens Sehested, Søren Dahl, Joachim Jacobsen, and J. R. Rostrup-Nielsen, *The Journal of Physical Chemistry B*, 2005, **109**, 2432–2438.

[48] P. M. Zimmerman, Z. Zhang and C. B. Musgrave, *Inorganic Chemistry*, 2010, **49**, 8724–8728.

[49] W. Leitner, *Angewandte Chemie International Edition in English*, 1995, **34**, 2207–2221.

[50] G. Kresse and J. Hafner, *Surface Science*, 2000, **459**, 287–302.

[51] G. Peng, S. Sibener, G. C. Schatz and M. Mavrikakis, *Surface Science*, 2012, **606**, 1050–1055.

[52] R. Watwe, H. Bengaard, J. Rostrup-Nielsen, J. Dumesic and J. Nørskov, *Journal of Catalysis*, 2000, **189**, 16–30.

[53] W. Xie, W. Sun, W. Chu, C. Jiang and Y. Xue, *Applied Surface Science*, 2012, **258**, 6239–6245.

[54] C. Schild, A. Wokaun, R. A. Koeppel and A. Baiker, *The Journal of Physical Chemistry*, 1991, **95**, 6341–6346.

[55] P. Giannozzi, S. Baroni, N. Bonini, M. Calandra, R. Car, C. Cavazzoni, D. Ceresoli, G. L. Chiarotti, M. Cococcioni, I. Dabo, A. Dal Corso, S. de Gironcoli, S. Fabris, G. Fratesi, R. Gebauer, U. Gerstmann, C. Gougoussis, A. Kokalj, M. Lazzeri, L. Martin-Samos, N. Marzari, F. Mauri, R. Mazzarello, S. Paolini, A. Pasquarello, L. Paulatto, C. Sbraccia, S. Scandolo, G. Sclauzero, A. P. Seitsonen, A. Smogunov, P. Umari and R. M. Wentzcovitch, *Journal of Physics: Condensed Matter*, 2009, **21**, 395502 (19pp).

[56] G. Henkelman, B. P. Uberuaga and H. Jónsson, *The Journal of Chemical Physics*, 2000, **113**, 9901–9904.

[57] A. Bundhoo, J. Schweicher, A. Frennet and N. Kruse, *The Journal of Physical Chemistry C*, 2009, **113**, 10731–10739.

Chapter 5

First Principles Study of Steam Methane Reforming Reaction on Ni (110) and Rh/Ni (110) Surfaces

Contents

5.1 Introduction

With the advent of technology, the consumption of energy is increasing at an unprecedented rate all over the world and to meet the need, fossil fuels have been playing a dominant role as major energy providers since long time. However, the side-effects due to the excessive reliance on fossil fuels including global warming, climate change, and steep hikes in the price of fuels invoke the urgency for the investigation of alternative energy resources. As a possible remedy for the energy solution, hydrogen has been predicted to be the most promising one in the remote future with advantages from its low environmental impact to its durable nature. [1, 2] Production of hydrogen generally transpires through steam reforming of fossil fuels, for which methane is preferable because of its availability and high H/C ratio. [3] In fact, Steam Methane Reforming (SMR) has become the most popular commercial method which contributes around 48 % to the current global hydrogen production. [4] To generate additional hydrogen, water-gas shift reaction (Eq. (5.2)) is performed simultaneously with the SMR (Eq. (5.1)) which evidently reduce the operating costs as well facilitate CO_2 capture at the source.

$$CH_4 + H_2O \rightarrow CO + 3H_2 \left[\Delta H_{298} = +206.1 KJ - mol^{-1}\right] \tag{5.1}$$

$$CO + H_2O \rightarrow CO_2 + H_2 \left[\Delta H_{298} = -41.15 KJ - mol^{-1}\right] \tag{5.2}$$

$$CH_4 + 2H_2O \rightarrow CO_2 + 4H_2 \left[\Delta H_{298} = +165.0 KJ - mol^{-1}\right] \tag{5.3}$$

SMR, being an energy intensive process requires relatively high temperature to proceed. Typically it is carried out at temperatures around $700 - 900^0C$ over Ni-based catalysts in commercial units where the fast turnover rates, lower cost and long-proven performance of nickel are the crucial factors. [4] However, hydrogen generation continues to be the challenging process over Ni catalyst due to the formation of large amount of fibrous carbon, known as carbon whiskers at the high operating temperature of SMR which influence the activity and stability of the catalyst itself and can even damage the reactor. Hence, there is significant interest in searching for the catalyst capable of delivering the similar or better catalytic performance as well inhibit carbon formation during the reaction. [5, 6] In these regards, researchers have proposed that alloying Ni with another transition metals exhibit promising signature towards SMR in terms of activity and stability against coke formation. [7] It is moreover reported that foreign atom substitutions can suppress the coke formation on Ni surface by enhancing the Ni metallic dispersion as well as aggregation of Ni nanoparticles during the high temperature reaction. [8, 9] In most of the applications, precious metal additives are being used. Precioug metals such as Rh, Ru, Pt, and Pd show higher activity in SMR in comparison to Ni but their use is limited by the high cost. [10–17] Though the exact activity order remains a matter of debate, as one of the most active metals for methane steam reforming, rhodium has been extensively recommended as a reforming catalyst by quantum-chemical methods. Chen et. al. [18] thoroughly investigated the effect of substitution of single transition metal atom (Cu, Ru, Rh, Pd, Ag, Pt, Au) on Ni (111) surface and concluded that Rh atom tailored Ni (111) surface is a good candidate for the concerned reaction because of modification in electronic structure. It is very important to understand SMR process at a fundamental level to have a more consistent understanding of the mechanism of the main reactions and as well the competing reactions for carbon formation.

The main aim of the present work is to study theoretically the kinetics of elementary steps of SMR. The stepwise mechanism has been compared and contrasted among Rh monolayer modified Ni (110) surface and clean Ni (110). The motivation for employing the parent surface as 110 is the kinetic measurements performed by Beebe et. al. [19] under high incident flux conditions, which suggested that Ni (110) is the best one amongst Ni (111), Ni (110) and Ni (100) surfaces for methane dissociation reaction but till now no kinetic study has been carried out theoretically. Secondly, single overlayer of Rh has been deposited on Ni (110) surface to detect the role of promoter on catalytic activity and stability over pure Ni (110) surface. Recently, a number of studies have been shown that overlayers (OLs) or near-surface alloys (NSAs) hold very unusual characteristics compared to their parent surfaces and mostly these bimetallic surfaces show better catalytic activity. [20] By metal deposition method, galvanic displacement, less noble metal monolayer deposited at underpotentials can be substituted by foreign metal monolayer. [21, 22] Again due to higher price of noble metal, Rh, only one layer of it has been used to cover up the Ni (110) surface. After investigating kinetics and mechanism for each step of dissociation reaction, interestingly, we found that Rh/Ni(110) surface needs lower activation energy barriers for the corresponding steps and less likely to adsorb elementary carbon on the surface with respect to the Ni(110) surface. Furthermore, we have also performed ab initio microkinetic model for SMR on Ni(110) and Rh/Ni(110) surface to obtain the microscopic insight of the effect of Rh overlayer on Ni(110) surface.

5.2 Computational Details

The quantum-chemical calculations were performed using Quantum Espresso package, in which the wave functions at each k-point are expanded with a plane wave basis set with a kinetic energy cut off up to 400 eV. The approximation, taken into account throughout the density functional theory calculations, was the generalized gradient approximation functional proposed by Perdew, Burke, and Ernzerhof, known as GGA-PBE [23]. Ultrasoft pseudopotentials from the publicly available repository of the QUANTUM ESPRESSO [24] distribution were applied to describe the ionic cores. Brillouin zone sampling was carried out using a Monkhorst-Pack grid for all the calculations and electronic occupations were determined using a Marzari-Vanderbilt scheme [25] with an energy smearing of 0.01 eV. Due to the presence of magnetic element (Ni) in our systems and since accurate quantitative description of the total energies is directly related to surface magnetism, consideration of spin-polarized effects is very essential. Once the difference between the total energy between two consecutive electronic optimization steps were smaller than 10^{-5} eV, the convergence of the electronic degrees of freedom was considered to be attained. The condition for the ionic relaxation was set such that the forces should be less than 10^{-3} eV/ Åfor all the ions. No symmetry constraints were put in force. It is already known that the consideration of van-der Waals interaction is necessary for an accurate quantitative description of the total energies; that is why dispersion corrections were taken into account. [26] The Ni (110) and

Rh/Ni (110) surfaces were represented as a two-dimensional slab in a 3D periodic cell. The Ni (110) model employed in this study consist of four-layer slab with a periodic (3×3) unit cell (1/9 monolayer (ML)); then, the Rh/Ni (110) surface was constructed by replacing the uppermost layer of Ni (110) surface by Rh (110). The computed equilibrium lattice constant for bulk nickel is 3.50 Å, in good agreement with the experimental value (3.52 Å). To circumvent periodic interactions, a vacuum layer of 12 Åwas used along the perpendicular direction to the surface. The optimized geometries have been achieved by considering Hellmann-Feynman forces acting on the atoms of the unit cell. Adsorption energies (ΔE_{ads}) of adsorbates were computed by

$$E = E_{surface+adsorbate} - E_{surface} - E_{adsorbate} \tag{5.4}$$

where $E_{surface+adsorbate}$ is the total energy of the relaxed surface with the adsorbate, $E_{surface}$ is the total energy of the bare relaxed surface and $E_{adsorbate}$ is the total energy of an isolated adsorbate. The first two terms were calculated considering the same parameters (k-point sampling, energy cutoff, etc.) mentioned above, the last term was obtained by performing spin-polarized Γ-point calculation of the isolated adsorbate placed in the middle of an empty box of dimension 20 Å×20 Å× 20 Å. In accordance with this definition, the negative value of adsorption energies implies binding between surfaces and adsorbates. Climbing Image Nudged Elastic Band-method (CI-NEB) [27, 28]method was exploited for determining the transition states of all the reaction pathways which is actually the variant of the nudged elastic band method and has been proven to be a very efficient technique for finding the minimum energy paths of chemical reactions. Convergence of saddle points and minima were considered to be achieved when the maximum force in each degree of freedom was less than 0.03 eV/ Å.

5.3 Results and Discussion

SMR proceess consists of large reaction network. In the present study, the following steps have been included for the conversion of CH_4 to CO_2.

Step 1:

$$CH_4 \rightarrow CH_3^* + H^*$$

Step 2:

$$CH_3^* \rightarrow CH_2^* + H^*$$

Step 3:

$$CH_2^* \rightarrow CH^* + H^*$$

Step 4:

$$CH^* \rightarrow C^* + H^*$$

Step 5:

$$H_2O \rightarrow OH^* + H^*$$

Step 6:

$$OH^* \rightarrow O^* + H^*$$

Step 7:

$$C^* + O^* \rightarrow CO^*$$

Step 8:

$$CO^* + O^* \rightarrow CO_2$$

Step 9:

$$2H^* \rightarrow H_2$$

Steps (1-4) includes the process of CH_4 adsorption and consecutive dissociation reaction to CH_x (x = 0-3) and atomic H on the catalyst surface. In steps (5-6), H_2O molecule dissociates into (OH^* + H^*), followed by (O^* + H^*). In the next steps (7-8), the chemisorbed C atom gets oxidized to CO and then CO_2. In final step (9), the formed H atoms may react together to form H_2 molecule.

Geometry optimizations have been carried out for all the reactants, intermediates and products on the different adsorption surface sites. The lowest energy structures (Fig. 5.1 and 5.2) have been considered for the further investigations of the reaction mechanism over Ni (110) and Rh/Ni (110) surfaces.

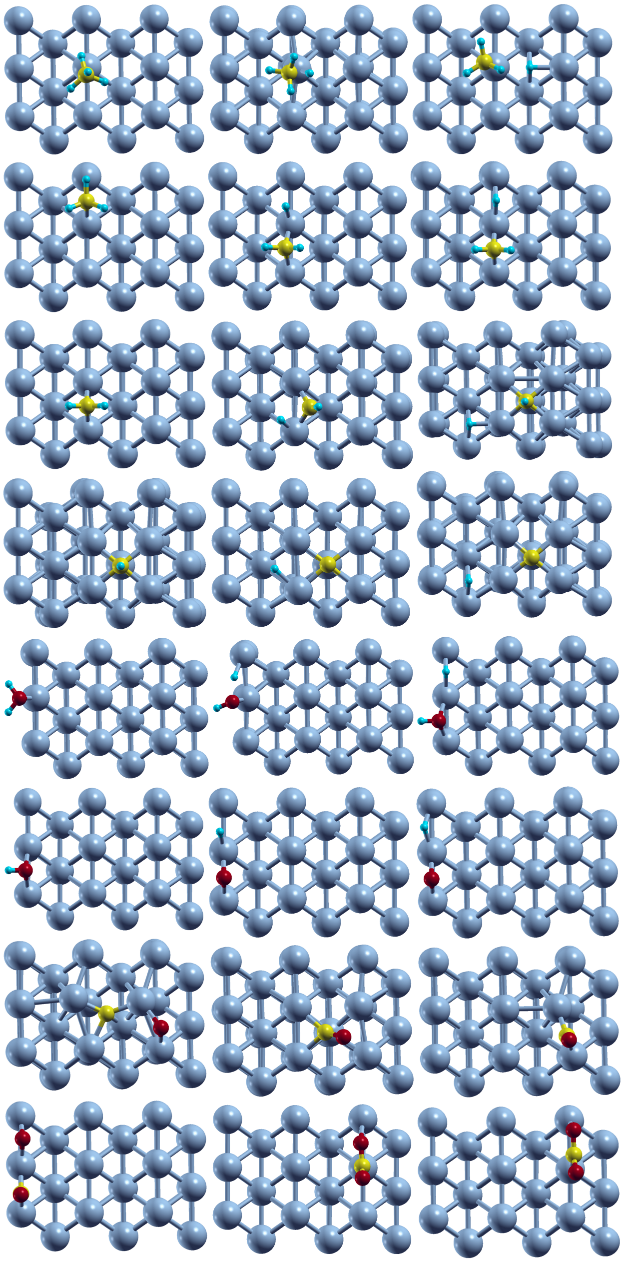

Figure 5.1: Complete process of steam methane reforming reaction on clean Ni (110) surface. Shown are the optimized initial state (left column), transition state (TS) (middle column) and final state (right column) of the successive reaction steps (1-8). Blue, yellow, cyan and red color correspond to Ni, C, H and O atoms, respectively.

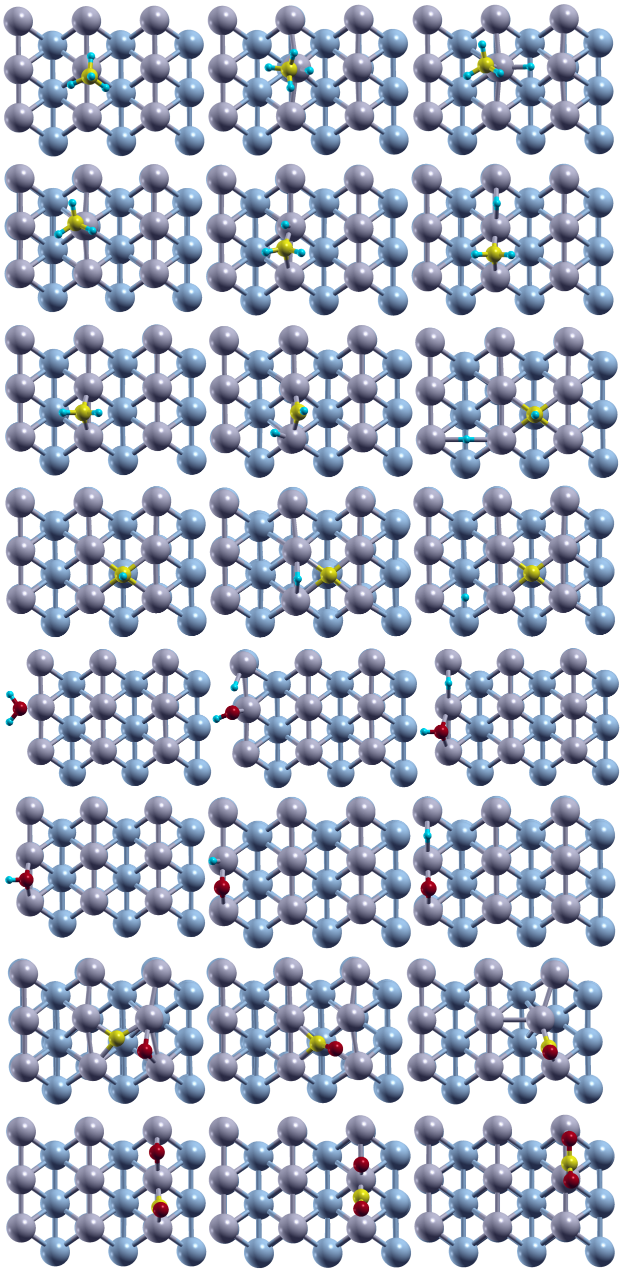

Figure 5.2: Complete process of steam methane reforming reaction on clean Rh/Ni (110) surface. Shown are the optimized initial state (left column), transition state (TS) (middle column) and final state (right column) of the successive reaction steps (1-8). Blue, grey, yellow, cyan and red color correspond to Ni, Rh, C, H and O atoms, respectively.

Table 5.1: Adsorption Energies (E_{ads}, eV) of intermediates on Ni(110) and Rh/Ni(110) surfaces

Surfaces	CH_3*	CH_2*	CH*	C*	OH*	O*	H*	CO*
Ni(110)	-1.98	-3.80	-6.87	-8.56	-3.50	-5.03	-2.39	-2.00
Rh/Ni(110)	-2.12	-4.33	-6.72	-7.62	-3.97	-4.98	-2.18	-1.92

The calculated adsorption energies of the associated intermediates on both the surfaces have been listed in Table 5.1. Difference in adsorption properties between Rh/Ni(110) and pure Ni(110) is due to the strain effect which is related to the modification of surface electronic structure by the variation in overlapping of various orbitals; however, among CH_3*, CH_2*, CH* and C* intermediates, the first two species adsorbs more strongly to Rh/Ni(110) surface which is in contrast to the results obtained by Fan et. al. [18] where single Rh atom addition leads to lowering in adsorption energy of CH_3* and CH_2* fragments than pure Ni(111) surface. This is due to the ligand effect stimulated by the interaction between Rh overlayer and adjacent substrate in the present study. However, CH* and C* show higher binding potency for pure Ni(110) surface in comparison to Rh/Ni(110) surface and this confirms the previous findings of the coke formation propensity on Ni surface. Increase in the adsorption energy, going from CH_3* to C* for both the systems which is consistent with the earlier reported results is due to the increasing number of free valence electrons upon successively reducing the number of H atoms.

5.3.1 Activation Energies for Elementary Steps

Following the study of adsorption behavior i.e. adsorption energies and structures of all the possible intermediates involved in the reaction, we need to find out the plausible minimum energy path (MEP) for the successive dehydrogenation from CH_4 to CO_2. Kinetic analysis of associated reactions on Ni(110) and Rh/Ni(110) surfaces have been investigated in detail. Figure 5.1 portrays the geometries of the initial, transition and final states of each step. The calculated heat of reactions and the activation energy barriers of the corresponding steps (1-9) on Ni(110) and Rh/Ni(110) surfaces are summarized in Table 5.2.

Table 5.2: Reaction energy (ΔE) and actvation energy barrier (E_a) for the elementary steps on Ni (110) and Rh/Ni (110)

Elementary step	System	E_a (eV)	$\Delta E(eV)$
$CH_4{}^* \rightarrow CH_3^* + H^*$	Ni (110)	0.89	0.03
	Rh/Ni (110)	0.46	0.10
$CH_3{}^* \rightarrow CH_2^* + H^*$	Ni (110)	0.80	0.30
	Rh/Ni (110)	0.25	-0.08
$CH_2{}^* \rightarrow CH^* + H^*$	Ni (110)	0.59	-0.88
	Rh/Ni (110)	0.73	-0.21
$CH^* \rightarrow C^* + H^*$	Ni (110)	0.50	-0.04
	Rh/Ni (110)	0.55	-0.15
$H_2O^* \rightarrow OH^*$ +H*	Ni (110)	0.39	-0.56
	Rh/Ni (110)	0.95	0.06
$OH^* \rightarrow O^*$ +H*	Ni (110)	0.61	0.14
	Rh/Ni (110)	0.58	0.50
$C^*+O^* \rightarrow CO^*$	Ni (110)	0.89	-0.60
	Rh/Ni (110)	0.84	-1.04
$CO^*+O^* \rightarrow CO_2$	Ni (110)	1.25	0.72
	Rh/Ni (110)	1.00	0.10
$H^*+H^* \rightarrow H_2$	Ni (110)	0.37	0.37
	Rh/Ni (110)	0.28	0.28

5.3.1.1 Step1: $CH_4{}^* \rightarrow CH_3{}^* + H^*$

Dissociation of methane to methyl and hydrogen is the first step of methane dehydrogenation reaction. The adsorption energy of methane on Ni(110) and Rh/Ni(110) surface are -0.2eV and -0.29 eV, respectively, which indicate the physisorption of saturated tetrahedral methane molecule on the surfaces. To form the product, methane molecule comes closer to the respective surface and accordingly one of the carbon-hydrogen (C-H) bonds gets activated; in the transition state, increase in the C-H bond distance leads to methyl and H fragment which sit together, in slightly tilted fashion, on the same Rh atom of Rh/Ni(110) surface while on Ni(110) surface, CH_3 adsorbs on top position and H on hollow site. The calculated activation energies of this step are 0.89 eV and 0.46 eV for the bare Ni(110) and Rh/Ni(110) surfaces respectively.

5.3.1.2 Step2: $CH_3^* \rightarrow CH_2^* + H^*$

The second step, i.e. the conversion of CH_3^* to CH_2^* and H^* takes place with the energy barriers of 0.80 eV on Ni(110) surface and 0.25 eV on Rh/Ni(110) surface. For Ni(110) surface bridge positions are the most stable site for both the initial and final intermediates of this step, i.e., CH_3^*, CH_2^* and atomic H^*. While dissociation of C-H bond in the transition state CH_3^* has to shift from one bridge site to adjacent one, leaving one bonded H behind, hence in this case (Ni(110)), the relatively heavier group (CH_2^*) has to travel a distance from initial state to final one. On the other hand, on Rh/Ni(110) surface, CH_3^* sits on the top of single Rh atom whereas CH_2^* and H^* prefer nearby bridge sites; therefore in the transition state CH_3^* dissociation occurs on top of the Rh atom itself and budging of CH_2^* slightly places it in bridge position. Therefore, this elementary step is more favorable on Rh/Ni(110) surface over bare Ni(110) surface with lower activation energy barrier.

5.3.1.3 Step3: $CH_2^* \rightarrow CH^* + H^*$

On both the surfaces, the dissociation takes place over the bridge site and results in the methylidyne in a hollow site. The computed values imply that cleavage of H from CH_2^* moiety is difficult step on Rh/Ni(110) surface with rather high activation energy barrier of 0.73 eV. But the transformation of CH_2^* to CH* and atomic H* occurs with relatively lower barrier of 0.59 eV for the Ni(110) surface.

5.3.1.4 Step4: $CH^* \rightarrow C^* + H^*$

The fourth step comprises of the formation of surface C* and atomic H* upon the dissociation of CH*; it needs to overcome the activation energy barriers of 0.48 eV on Ni(110) and 0.57 eV on Rh/Ni(110) surface. It has been found that on both the surfaces, CH* prefers to adsorb on the hollow site and after dissociation, elementary C* stays at the hollow site while H* moves to the bridge site.

5.3.1.5 Step5: $H_2O^* \rightarrow OH^* + H^*$

In the next step, oxidation of H_2O^* to atomic OH* and atomic H* has been considered. Water adsorbs on the top site of both the Ni(110) and Rh/Ni(110) surfaces with adsorption energies of -0.50 eV and -0.80 eV, respectively. The dissociation of H_2O^* to OH* and atomic H* ($H_2O^* \rightarrow OH^* + H^*$) needs considerably lower activation energy barrier of 0.39 eV on Ni(110) in comparison to Rh/Ni(110) surface (0.95 eV). On both the surfaces, dissociated fragments (OH* and atomic H*) get adsorbed on neighbouring bridged position.

5.3.1.6 Step6: OH* → O* + H*

The subsequent step is the dehydrogenation of OH^* to O^* and H^* with almost comparable barrier heights of 0.61 eV and 0.58 eV on Ni(110) and Rh/Ni(110) surfaces, respectively. We found in the previous step that OH* moiety prefers to bind at the bridge position on both the systems considered here. In this step, the O-H bond of OH* cleaves and results into O* and H*. Again, both the fragments (O* and H*) are found to adsorb on the adjacent bridge positions of Ni(110) and as well Rh/Ni(110) surface.

5.3.1.7 Step7: C* + O* → CO*

In this step, we have considered the oxidation of elementary C*, formed at step4, with the O* to form CO*. On both the surfaces, O* from the bridge position moves towards C* which is preferably adsorbed the hollow site and after forming C-O bond, the resultant CO* finally adsorbs at the bridge position. As mentioned earlier, C* adsorbs more strongly on Ni(110) surface and eventually, it needs higher activation energy (0.89 eV) to get oxidised to CO* compared to Rh/Ni(110) surface (0.84 eV).

5.3.1.8 Step8: CO* + O* → CO_2

The next step is the further oxidation of CO* to CO_2* where both the reactants (CO* and O*) are initially at the bridge position and subsequently they react together to form the final product CO_2 which prefers to be adsorbed on the bridge positions of Rh/Ni(110) and as well Ni(110) surfaces, respectively. The barrier height for the associated oxidation reaction is relatively higher on Ni(110) surface by 0.25 eV.

5.3.1.9 Step9: $H^* + H^* \rightarrow H_2$

The final step is the formation of H_2 from the H^* atoms. The corresponding activation energy barriers on Ni (110) and Rh/Ni (110) surfaces are 0.37 eV and 0.28 eV respectively.

In short, we find that the catalytic activity of Rh/Ni(110) system is comparable or better in comparison to Ni(110) surface in terms of kinetics of the reaction (except for the step 3, 4 and 5 where Rh/Ni(110) surface needs higher activation energy barrier than Ni(110) surface). However, for the SMR reaction, the higher barrier height for the reaction step 3 and 4 is favourable in the light of high coke formation tendency of Ni(110) surface. Moreover, comparison of the adsorption energies of C* (Table 5.1) on both the surfaces also recommend that Rh overlayer on Ni(110) surface considerably reduce the binding strength of C*.

5.3.2 Microkinetic Modeling

A kinetic model has been constructed where the flowing gaseous species and stationary surface species are treated using the following CSTR (continuous-stirred tank reactor) formulation

$$\frac{\partial n_i}{\partial t} = A_s \sum_{j=1}^{no.rxns} \nu_{j,i} \left[k_j \prod_{l=a}^{S_R} C_l^{-\nu_{j,i}} - k_j \prod_{l=a}^{S_P} C_l^{\nu_{j,i}} \right] + \gamma_i \left(F_{i,in} - \frac{VC_i}{t_{res}} \right) \qquad (5.5)$$

here, $\nu_{j,i}$ is the stoichiometric coefficient of component i in the reaction j, k is the rate coefficient for the forward (j) and reverse (-j) reactions, C is the concentration of the subscripted component, V is the volume of the reactor, A_s is the total surface area of the catalyst, and γ_i is a variable which is equal to 1 for gaseous species and equal to zero for the surface species.

The molar flow of gas-phase species i into the reactor, F$_{i,in}$, can be defined in terms of the specified reaction time, t$_{res}$,

$$F_{i,in} = \frac{PV}{RT}\frac{y_{i,in}}{t_{res}} \tag{5.6}$$

here P and T represent pressure and temperature in the reactor, R is the universal gas constant and y$_{i,in}$ is the mole fraction of the species i in the feed.

The complete set of time-dependent CSTR equations (one for each gas-phase or surface species) have been solved using ODE15s in MATLAB, time stepping to steady state for a specified residence time. All the DFT-predicted computed values for SMR are put in a microkinetic model. Model parameter considers a catalyst area of 1 m^2. The kinetics of SMR is carried out at 525^{0}C and 1.2 bar pressure with a H_2O/CH_4 ratio of 3.0 and a reactor residence time of 60s. We are mainly interested in finding the effect of Rh overlayer towards the efficiency of CH_4 conversion.

In this regard, our computed values obtained from modeling study suggests 27 % of CH_4 conversion in the presence of Ni (110) surface and this increases to 32 % on Rh/Ni (110) surface. Interestingly, these values are in good ageement with the experimental results obtained by Luna et. al [29].

5.4 Conclusion

We have computed the energetics as well as kinetics of SMR reaction on Ni (110) and Rh/Ni (110) surfaces. It has been found that Rh/Ni (110) surface is more efficient from both the activity as well as stability point of view, since a

Rh overlayer on a Ni (110) surface reduces both the activation energy barriers and the coke formation tendency efficiently in comparison to pure Ni (110) surface. More importantly, we find that the CH_4 conversion efficiency increase by 5 % in the presence of Rh/Ni (110) surface.

In summary, our research provides a novel idea to design highly efficient and economically benign bimetallic catalysts for the SMR reaction by depositing a single layer of foreign metal on a clean surface and the hybrid organization can perform as a very good catalyst for the concerned process with respect to the single crystal surface. Thus, this study suggests that the catalytic properties can be tailored largely by introducing a bimetallic overlayer on the parent metal surface.

Bibliography

[1] K. Blok, R. Williams, R. Katofsky and C. Hendriks, 1997-02-01T00:00:00, **22**, 161–168.

[2] K. Jordal, R. Bredesen, H. Kvamsdal and O. Bolland, *Energy*, 2004, **29**, 1269–1278.

[3] B. D. Solomon and A. Banerjee, *Energy Policy*, 2006, **34**, 781–792.

[4] J. K. Norskov and C. H. Christensen, *Science*, 2006, **312**, 1322–1323.

[5] J. Sehested, *Catalysis Today*, 2006, **111**, 103–110.

[6] H. Bengaard, J. Nørskov, J. Sehested, B. Clausen, L. Nielsen, A. Molenbroek and J. Rostrup-Nielsen, *Journal of Catalysis*, 2002, **209**, 365–384.

---

[7] A. M. Molenbroek*, , J. K. Nørskov and B. S. Clausen, *The Journal of Physical Chemistry B*, 2001, **105**, 5450–5458.

[8] Eranda Nikolla, Adam Holewinski, Johannes Schwank, and S. Linic*, *Journal of the American Chemical Society*, 2006, **128**, 11354–11355.

[9] E. Nikolla, J. Schwank and S. Linic, *Journal of Catalysis*, 2007, **250**, 85–93.

[10] W. An, X. C. Zeng and C. H. Turner, *The Journal of Chemical Physics*, 2009, **131**,.

[11] J. H. Jeong, J. W. Lee, D. J. Seo, Y. Seo, W. L. Yoon, D. K. Lee and D. H. Kim, *Applied Catalysis A: General*, 2006, **302**, 151–156.

[12] D. Li, T. Shishido, Y. Oumi, T. Sano and K. Takehira, *Applied Catalysis A: General*, 2007, **332**, 98–109.

[13] H. Arbag, S. Yasyerli, N. Yasyerli and G. Dogu, *International Journal of Hydrogen Energy*, 2010, **35**, 2296–2304.

[14] Sakae Takenaka, Yukio Shigeta, Eishi Tanabe and Kiyoshi Otsuka*, *The Journal of Physical Chemistry B*, 2004, **108**, 7656–7664.

[15] B. Steinhauer, M. R. Kasireddy, J. Radnik and A. Martin, *Applied Catalysis A: General*, 2009, **366**, 333–341.

[16] M. García-Diéguez, I. Pieta, M. Herrera, M. Larrubia and L. Alemany, *Journal of Catalysis*, 2010, **270**, 136–145.

[17] A. M. Molenbroek*, J. K. Nørskov and B. S. Clausen, *The Journal of Physical Chemistry B*, 2001, **105**, 5450–5458.

[18] C. Fan, Y.-A. Zhu, Y. Xu, Y. Zhou, X.-G. Zhou and D. Chen, *The Journal of Chemical Physics*, 2012, **137**, 014703.

[19] T. P. Beebe, D. W. Goodman, B. D. Kay and J. T. Yates, *The Journal of Chemical Physics*, 1987, **87**, 2305–2315.

[20] A. S. Bandarenka, A. S. Varela, M. Karamad, F. Calle-Vallejo, L. Bech, F. J. Perez-Alonso, J. Rossmeisl, I. E. L. Stephens and I. Chorkendorff, *Angewandte Chemie International Edition*, 2012, **51**, 11642–11642.

[21] S. Brankovic, J. Wang and R. Adžić, *Surface Science*, 2001, **474**, L173–L179.

[22] J. Zhang, M. B. Vukmirovic, Y. Xu, M. Mavrikakis and R. R. Adzic, *Angewandte Chemie International Edition*, 2005, **44**, 2132–2135.

[23] J. P. Perdew, K. Burke and M. Ernzerhof, *Phys. Rev. Lett.*, 1996, **77**, 3865–3868.

[24] P. Giannozzi, S. Baroni, N. Bonini, M. Calandra, R. Car, C. Cavazzoni, D. Ceresoli, G. L. Chiarotti, M. Cococcioni, I. Dabo, A. Dal Corso, S. de Gironcoli, S. Fabris, G. Fratesi, R. Gebauer, U. Gerstmann, C. Gougoussis, A. Kokalj, M. Lazzeri, L. Martin-Samos, N. Marzari, F. Mauri, R. Mazzarello, S. Paolini, A. Pasquarello, L. Paulatto, C. Sbraccia, S. Scandolo, G. Sclauzero, A. P. Seitsonen, A. Smogunov, P. Umari and R. M. Wentzcovitch, *Journal of Physics: Condensed Matter*, 2009, **21**, 395502 (19pp).

[25] N. Marzari, D. Vanderbilt, A. De Vita and M. C. Payne, *Phys. Rev. Lett.*, 1999, **82**, 3296–3299.

[26] S. Grimme, *Journal of Computational Chemistry*, 2006, **27**, 1787–1799.

[27] G. Henkelman, B. P. Uberuaga and H. Jónsson, *The Journal of Chemical Physics*, 2000, **113**, year.

[28] G. Henkelman and H. Jónsson, *The Journal of Chemical Physics*, 2000, **113**, year.

[29] E. C. Luna, A. M. Becerra and M. I. Dimitrijewits, *Reaction Kinetics and Catalysis Letters*, **67**, 247–252.

Chapter 6

Towards Methanol Synthesis from CO_2 and H_2 on Iridium clusters

Contents

6.1 Introduction

Hydrogenation of CO_2 to methanol has attracted attention of many researchers worldwide as a promising route for chemical sequestration of CO_2. [1–5] Methanol, being a clean-burning, cost-competitive potential energy resource, is targeted as a successful replacement of coventional transportation fuel with only minimal modifications to vehicle design. Every year, about 65 million metric tons of methanol is produced and eventually become third-most large-scale chemical product. However, $CO_2 \rightarrow CH_3OH$ is a challenging task due to kinetic and thermodynamic stability of CO_2 (Δ G^0_{298} = -394.36 kJ mol^{-1}); so great deal of efforts have been put towards the development of catalysts for the activation of CO_2 and its corresponding hydrogenation to methanol. [6]

The standard process to synthesize methanol in industrial scale is from mixtures of H_2, CO_2 and CO, at elevated pressures of 50 to 100 atm and temperatures of 450 to 600 K [7]; thereby, methanol is reckoned as one of the few fuels that actively use CO_2 stream in its feedstock. Though a large range of catalysts [8–10] have been experimented for the production of methanol, $Cu/ZnO/Al_2O_3$ [11, 12] is turned out to be choice of industrial catalyst. However, it is found that the low-pressure methanol synthesis leads to significant CO production as a by-product using the conventional $Cu/ZnO/Al_2O_3$ catalyst and that leads to two serious negative impacts in practical use, (i) conversion is kinetically reduced to 15 to 25 % and (ii) CO poisons the Pt catalysts used and thus affects the efficiency of fuel cell. [13] Hence, there is continuous search for new catalysts to advance this field, both experimentally and theoretically. [8, 14] Though majority of them still rely on Cu and Zn, as their main active components [15–17], but modification with various metals have been significantly explored. [18–20] Recently, Studt et al. carried out thorough search on Ni-Ga based catalysts for reduction of CO_2 and reported the discovery of Ni_5Ga_3 as an highly adequate catalyst for methanol formation [21] with much lower CO generation in comparison to traditional $Cu/ZnO/Al_2O_3$ catalysts.

The tremendous efficiency of Ir based catalysts for participating in CO_2 hydrogenation have been very recently exploited after the breakthrough in the current research and that results in renewed attention on iridium complexes. [22–24], In fact, Nozaki and colleagues have been achieved rates as high as 150,000 h^{-1} at 200 °C and a turnover number (TON) of 3,500,000 for CO_2 hydrogenation reaction using Ir pincer complex. [25] The development of a viable method in the past decade for producing nearly monodispersed Ir_4 particles using $Ir_4(CO)_{12}$ complexes [26] as a source of iridium has been a success. Also, the recently reported peculiar catalytic properties of noble and transition metal nanocluster drags the curiosity of the researchers towards the study of iridium nanoparticles. [27–33] Amongst many transition metal clusters [34–37], Iridium metal cluster has been shown to be the most effective catalyst for the automobile catalytic converters due to their ability to remove pollutants, such as, NO_x, by adsorbing it very strongly from exhaust as investigated by density functional theory performed by Endou et al. [38] There are several other catalytic reactions, where iridium shows great promise, for example, biphastic hydrogenation reaction, C-H or Si-H bond activation etc. [39–41] For the hydrogenation of arenes and ketones, no loss of activity has been found after recycling, which makes iridium a very good reusable catalyst. [42]

Even after the significant study of the catalytic activity of Ir till date, the mechanistic details for the methanol formation from CO_2 hydrogenation on Ir nanoparticles remain unclear and speculative. This lack of information impedes further development in the production of methanol using the Ir nanoparticles. In fact, this motivates us to study the thorough mechanism of CO_2 to CH_3OH conversion on three different sized Ir clusters, Ir_7, Ir_{13} and Ir_{55}, aiming to understand the size-dependent catalytic activity of Ir clusters towards methanol synthesis. In short, on one hand, our study provides better understanding of the reaction mechanism of methanol synthesis and size-dependent activity of the Ir clusters; on the other hand, it also helps to predict possible new catalyst which might be appropriate candidate for CO_2 to CH_3OH transformation using only hydrogen and carbon dioxide.

6.2 Computational Details

All the calculations are carried out via density functional theory with plane wave basis set as implemented in Quantum Espresso.[43].The Perdew-Burke-Ernzerhof (PBE)[44] generalized gradient approximation (GGA) correction formalism is employed for the exchange-correlation functional. The ionic cores have been described by ultrasoft pseudopotential[45]. The Rappe-Rabe-Kaxiras-Joannopoulos (RRKJ) ultrasoft pseudopotential for Ir, C, H, O have been taken from the publicly available repository of the Quantum Espresso distribution. The clusters were placed in a simple cubic box of size 20Å×20Å×20Åso that the interaction between the cluster and neighbouring replica is minimal. Only the gamma (Γ) point (k=0) is considered while sampling over the Brillouin zone. The wave-functions were expanded with a plane wave basis set with a kinetic energy cutoff of 30 Ryd. All the clusters are fully relaxed until the interatomic forces are smaller than 10^{-3} eV/Å. To aid the convergence, electronic occupancies were allowed by using Marzari-Vanderbilt scheme with energy smearing value of 0.005 Ryd. The adsorption energies for the adsorbates are calculated as,

$$E = E_{cluster+adsorbate} - E_{cluster} - E_{adsorbate} \tag{6.1}$$

where $E_{cluster+adsorbate}$, $E_{cluster}$ and $E_{adsorbate}$ are the total energies of the adsorbate adsorbed on cluster, the bare cluster and the adsorbate, respectively. For the calculation of the activation barriers climbing-image nudged elastic (CI-NEB) band method [46–49] is used and the activation energy barriers are denoted as E_a. All the three clusters have been shown in Fig. 6.1.

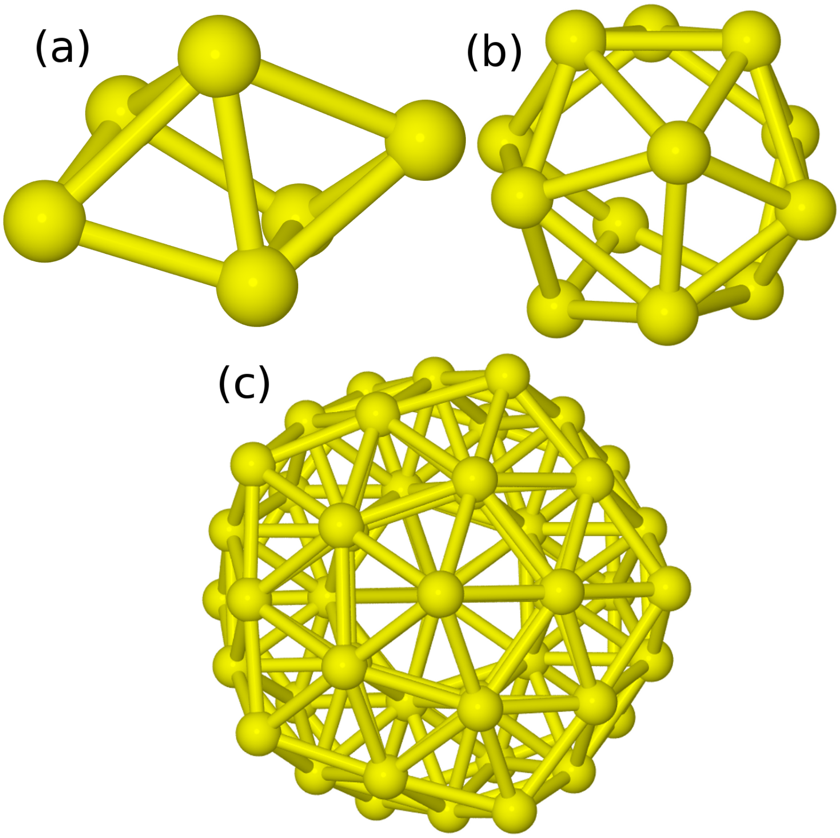

Figure 6.1: Optimized structures of Ir clusters, (a) Ir_7, (b) Ir_{13} and (c) Ir_{55} clusters. Yellow: Ir

6.3 Results and discussion

6.3.1 Adsorption behavior of CO_2 and H_2 on Ir clusters

For the heterogeneous catalysis, the binding strength of reactants plays a key role on the catalytic activity of the catalyst.[50] Hereby, we first investigate the adsorption behavior of CO_2 and H_2 on Ir_7, Ir_{13} and Ir_{55} clusters.

Adsorption of CO_2 can be simply assigned by the bending of the $\angle$ OCO and the C−O bond distances, as these are well-known descriptors for the activation of CO_2. The degree of changes in bond length and angle in adsorbed state with respect to the equilibrium state of an isolated CO_2 molecule indicates the strength of adsorption. Our DFT calculations yield V-shaped CO_2 molecule after adsorption on Ir clusters. The bond lengths of each $C = O$ double bond are elongated to 1.22 Åand 1.33 Å.(isolated CO_2 has bond length of 1.16 Å) irrespective of the size of the clusters. $\angle$ OCO bond angle alters from 180 °C to 127 °C and this is certainly responsible for the observed V-shape. (see Figure 6.2) Longer bond distances and smaller bond angle indicate transfer of charge from the Ir to CO_2 antibonding orbital. The calculated CO_2 adsorption energies are Ir_7 (-0.70 eV); Ir_{13} (-1.43 eV) and Ir_{55} (-0.80 eV).

The next step is computing the interaction of H_2 molecule with Ir catalyst, a very relevant step for the hydrogenation of CO_2 to CH_3OH. H_2 can be dissociatively adsorbed on the Ir clusters producing a reservoir of H atoms with negligible kinetic barriers of 0.007 eV (Ir_7); 0.003 eV (Ir_{13}) and 0.010 eV (Ir_{55}). Fig. 6.2 and Fig. 6.3 displays the corresponding structures of H_2 adsorbed Ir clusters.

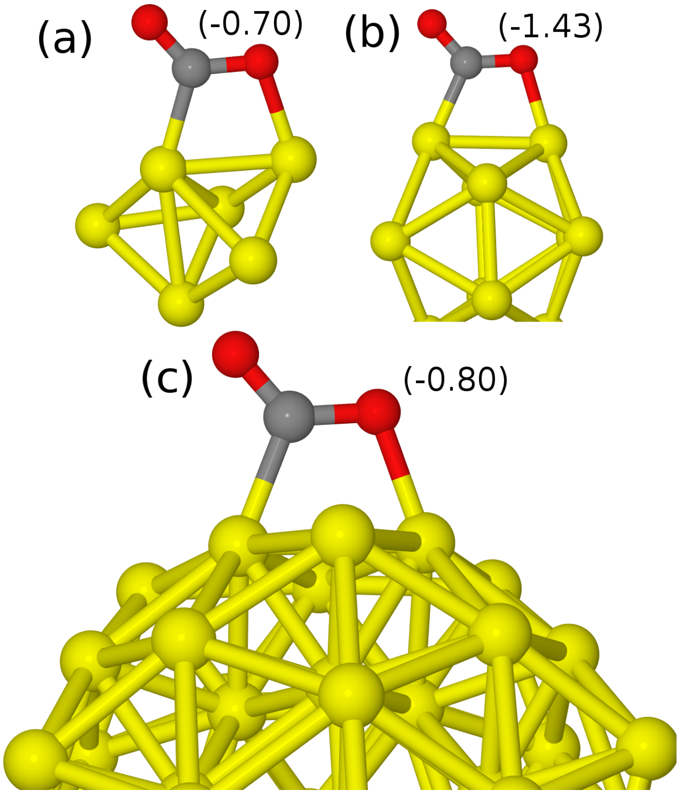

Figure 6.2: Optimized structures of CO_2 adsorbed on Ir clusters, (a) Ir_7, (b) Ir_{13} and (c) Ir_{55} clusters. Adsorption energies in eV are shown in parenthesis. Yellow: Ir; Grey: C; Red: O

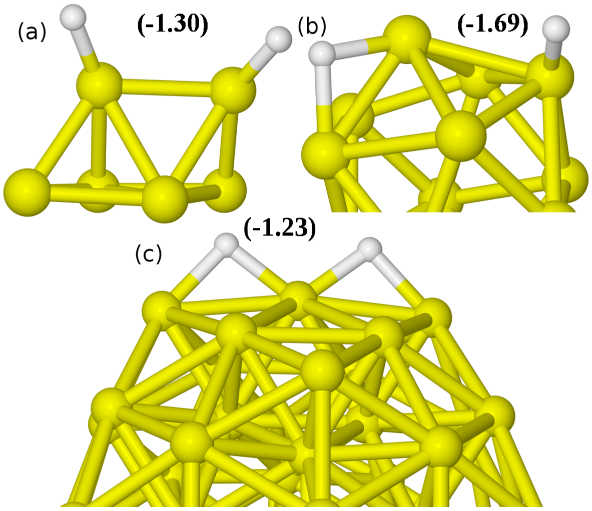

Figure 6.3: Optimized structures of H_2 adsorbed on Ir clusters, (a) Ir_7, (b) Ir_{13} and (c) Ir_{55} clusters. Adsorption energies in eV are shown in parenthesis. Yellow: Ir; White: H

The corresponding energies for the adsorption are Ir_7 (-1.30 eV); Ir_{13} (-1.69 eV) and Ir_{55} (-1.56 eV).

6.3.2 Mechanistic Study

To investigate the catalytic activity, various reaction routes are investigated for the CO_2 conversion to methanol on Ir clusters, which is discussed below in detail. The following four possible reaction pathways for the conversion of CO_2 to CH_3OH have been extensively addressed in the literature: Path (a) is the direct CO_2 dissociation route which involves the direct dissociation of the CO_2 into the adsorbed CO molecule and O atom, then followed by the hydrogenation of CO;[13] path (b) also involves the generation and hydrogenation of CO. Differently, CO is formed through the reverse water gas shift reaction (RWGS, $CO_2 + H_2 \rightarrow CO + H_2O$). [5] In another two pathways, CO_2 is directly hydrogenated to methanol through different intermediates without the formation of CO. As shown in Fig. 6.4, path (c) requires the formation of formate intermediate, thus denoted as formate route, whereas formic acid is formed in path (d), thus named as formic acid route.

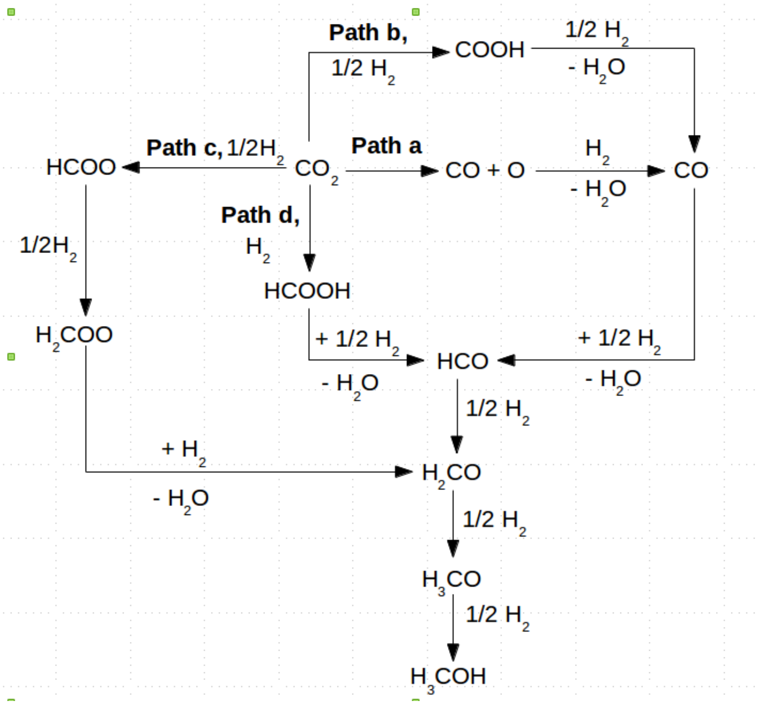

Figure 6.4: Schematic diagram of possible routes of methanol formation from CO_2 hydrogenation

6.3.3 The route with the Direct CO_2 dissociation and the Reverse water-gas shift route

The direct CO_2 dissociation route and the RWGS route, both involve the splitting of CO_2 leading to the formation of CO, then followed by the hydrogenation of CO. The production of CO from the mixture of CO_2 and H_2 during the methanol synthesis is experimentally noted but the exact origin remains elusive. [51]

In the present case, it is found that due to the strong adsorption of CO_2 on Ir clusters, dissociation of activated CO_2 (CO_2*) to CO* and O* is favourable with low kinetic energy barrier (Fig. 6.5); the computed activation energies are 0.2 eV, 0.27 eV, and 0.47 eV for Ir_7, Ir_{13} and Ir_{55} clusters respectively.

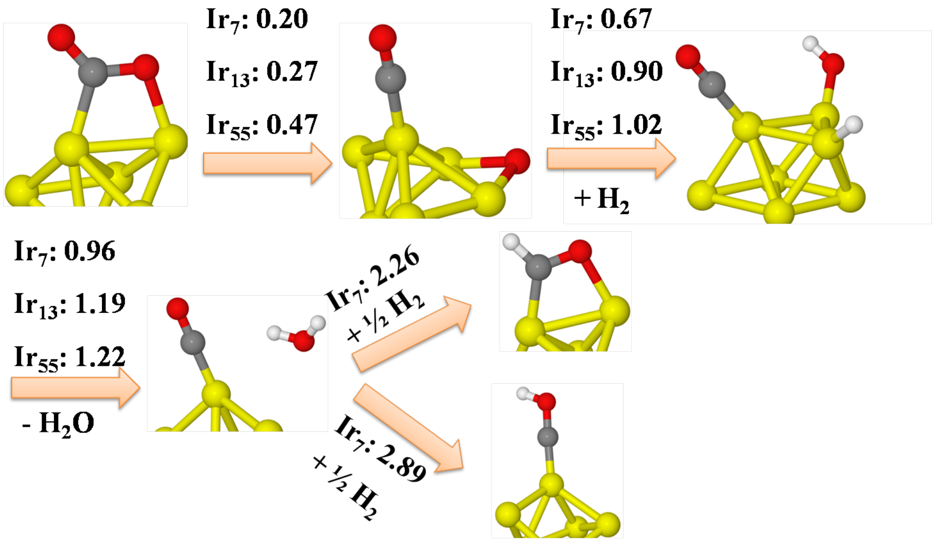

Figure 6.5: Optimized structures of some reaction intermediates involved in methanol synthesis through direct CO_2 dissociation route on Ir cluster. The corresponding activation energies (in eV) are shown for each step. The color code is same as previously mentioned.

Moreover, the reactions are exothermic with energy values Ir_7 (0.52 eV), Ir_{13} (0.35 eV) and Ir_{55} (0.85 eV). The relatively lower barrier for CO_2 dissociation in the presence of Ir catalysts in comparison to conventional catalysts is quite intereseting. However, in the light of the activity of CO_2 dissociation on Ir clusters, Ir_7 cluster is found to be the most active, followed by Ir_{13} and Ir_{55} clusters. The resulting atomic O* is removed from the Ir clusters by the formation of H_2O in the consecutive two steps, (i) $O^* + H^* \rightarrow OH^*$ and (ii) $OH^* + H^* \rightarrow H_2O(g)$. The corresponding activation energy values for the two steps are, Ir_7 (0.67 eV, 0.96 eV); Ir_{13} (0.90 eV, 1.19 eV); Ir_{55} (1.02 eV, 1.22 eV). The very next step towards the final product, methanol, through CO-aided hydrogenation is the formation of adsorbed HCO* or its isomer COH* intermediate from the adsorbed CO*. There exists convincing evidence for the CO-mediated hydrogenation reactions through a formyl intermediate (HCO*) which plays the significant role as a H-carrier. The exhaustive research [52] on the mechanism of methanol synthesis on Cu through CO_2 and CO hydrogenation suggests that barrier (0.99 eV) for CO* to HCO* is always lower than direct hydrogenation steps, hence ($CO^* + H^* \rightarrow HCO^*$) is recognized as one of the key steps in CO hydrogenation mechanism on the Cu surface inspite of its (HCO*) very low stability and surface concentration. Recent study by Liu et al. shows that on the modified model Mo_6S_8 cluster, [53] reduction of CO* to HCO* requires very less energy barrier than the conventional pure Cu system. On the contrary, over the supported Pd_4 cluster (Pd_4/In_2O_3) [54] and Cu/ZnO composite system, CO* has to cross comparatively higher energy barriers of 1.20 eV and 1.44 eV respectively to be hydrogenated to HCO*. [55]

Our DFT calculations suggest that in the presence of Ir catalysts, the hydrogenation reactions of CO* are highly unfavourable with barriers of 2.26 eV and 2.89 eV (Ir_7) for the formation of HCO* and COH* respectively; so the $CO^* + H^* \rightarrow HCO^*/COH^*$ path is kinetically precluded. The corresponding barriers are > 3 eV for Ir_{13} and Ir_{55} clusters. Consequently, the apparent high activation barrier effectively blocks the possibilities of the methanol synthesis through CO-mediated path on Ir clusters.

Another majorly studied mechanism for the $CO_2 \rightarrow CO$ conversion is reverse water-gas shift (RWGS) reaction: $CO_2 + H_2 \rightarrow CO + H_2O$; in general, the reaction is mediated through hydrocarboxyl (COOH) intermediate, followed by dissociation of C−O bond, leading to CO and OH. As mentioned earlier, the starting materials for the methanol synthesis reaction include CO, CO_2 and H_2; therefore, the conversion of CO_2 and H_2 into CO and H_2O via

RWGS reaction has been frequently observed under experimental condition. On Ir clusters, the H-assisted CO_2* dissociation to CO* and OH* (CO_2 + H* → CO* + OH*) is the most preferential one via ER mechanism with activation energy barriers of 0.15 eV (Ir_7), 0.22 eV (Ir_{13}) and 0.31 eV (Ir_{55}). However, the further hydrogenation of CO* to CH_3OH follows the same pathway as that of previous CO route via HCO* and that is limited by the high activation energy barrier which has been already discussed in detail.

6.3.4 Formate route

Formate route is one of the most frequently invoked path for the CO_2 hydrogenation reaction and the resulting formate species is experimentally found, probable key intermediate during methanol synthesis. [56–59] However, the specific role of the formate intermediate towards methanol production is exclusively determined by the catalyst present in the process.

In the present work, to detect the mechanism of surface HCOO* species formation on Ir clusters, two possible pathways initiated with the CO_2* and H* have been taken into account (i) direct combination of CO_2* and H* and (ii) indirect combination of CO_2* and H* via a carbonate (CO_3*) intermediate. (i) The former one, i.e. the direct combination of CO_2* and H* to the formate (HCOO*) is the most commonly detected approach in various experimental and theoretical studies. [60–64] After dissociative adsorption of H_2 on Ir clusters, CO_2 directly interacts with the atomic H* to form HCOO* intermediate; the adsorbed HCOO* species binds to the top sites of Ir clusters in bidentate configuration (Fig. 6.6) through the oxygen atoms, in consistent with the previously observed HCOO* configuration by a combined IR/TPD study on Cu/SiO_2.

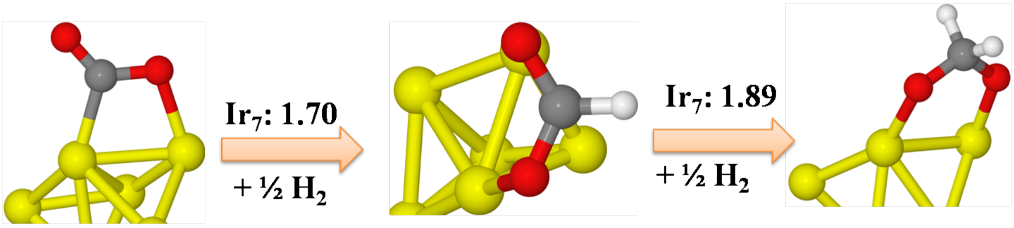

Figure 6.6: Optimized structures of some reaction intermediates involved in methanol synthesis through formate route on Ir cluster. The corresponding activation energies (in eV) are shown for each step. The color code is same as previously mentioned.

The reaction is endothermic by 0.70 eV with an activation energy barrier of 1.70 eV for Ir_7 indicating that this step is energetically not persuadable. However, for the other two Ir clusters (Ir_{13} and Ir_{55}), the reaction is more unfavourable with barrier heights > 2 eV. (ii) Various experimental and theoretical methods, viz. polarization modulation infrared reflection absorption spectroscopy (PM-IRRAS), electron energy loss spectroscopy (EELS), temperature programmed spectroscopy (TPD), X-ray photoelectron spectroscopy (XPS) and DFT, corroborates that path to methanol can proceed through a carbonate (CO_3^*) intermediate [59, 62, 65–67] which acts as a medium to indirectly combine CO_2^* and H*. On Cu deposited Pt (111) surface CO_2^* dissociates into CO* and atomic O* followed by a facile reaction between CO_2^* and resulting O* atom produces carbonate species (CO_3^*). [68] Nevertheless, the basic requirement for the formation of CO_3^* is the presence of preadsorbed oxygen. Though on the iridium clusters, the generation of surface O* is feasible with relatively low barriers ($CO_2^* \rightarrow CO^* + O^*$) as discussed previously, the energy needed to produce CO_3^* is very high 2.30 eV(Ir_7); 2.95 eV(Ir_{13})

and 3.05 eV (Ir_{55}) and an endothermicity of sin 1.80 eV. Hence, on account of the theoretical study, the formation of methanol via formate intermediate is excluded from our proposed mechanism as the concerned path is neither kinetically nor thermodynamically feasible in both the direct or indirect routes.

6.3.5 Formic Acid route

The synthesis of methanol from CO_2 and H_2 via HCOOH is rarely observed path on conventional catalysts. To the best of our knowledge, very few catalysts for example, $Cu/ZnO/Al_2O_3$ and recently studied Co and Rh doped Mo_6S_8 cluster,[53] have suggested HCOOH* as an active reaction mediator for ($CO_2 + H_2 \rightarrow CH_3OH$) reaction. Otherwise, isotopic labelling and FTIR studies report that CH_3OH is not synthesized by the protonation of HCOO* or HCOOH* on Cu/ZrO_2;[69, 70] similar conclusion has been arrived by the MS-IR experiments [71] and kinetic modelling performed on the Cu/SiO_2 or pure Cu catalysts.[72] Often, due to negligible interaction between HCOOH* and catalytic surfaces, the former one dissociates back to more stable formate species, (HCOO* + H*) with lower kinetic energy barrier. [61, 64] In fact, there is no direct experimental evidence of the existence of HCOOH*, instead the reverse dehydrogenation reaction to HCOO* is well-reported on Cu surfaces.[73, 74] Two other competitive dissociative reactions, though less studied, ($HCOOH^* \rightarrow HCO^* + OH^*$) and ($HCOOH^* \rightarrow HCOH^* + O^*$) are specified in the literature where HCOOH* acts as a precursor of C-O bond cleavage, a necessary step for methanol formation. However, if the activation energy barriers for the mentioned dehydrogenation reactions are considerably higher than the adsorption energies of HCOOH*, it has been noticed that

HCOOH prefers to desorb out of the surface rather dissociation as found on Cu/ZnO or Pd_4/In_2O_3 [54] catalysts.

In the present study, first we have examined the interaction of HCOOH* with Ir clusters. Interestingly, HCOOH* adsorbs dissociatively via cleaving of C-O bond on all the three clusters and generates formyl and hydroxyl, (HCO* + OH*) species. The adsorption energies of the (HCO* + OH*) are Ir_7 (-1.90 eV); Ir_{13} (-2.00 eV); Ir_{55} (-2.31 eV) indicate strong interactions and thereby the probability of the desorption of HCOOH as a gaseous molecule from the Ir clusters can be excluded. To detect the most possible path that destine to (HCO* + OH*) from CO_2 and H_2, the following mechanisms have been gone through, (i) via hydrogenation of formate (HCOO*) and (ii) via direct hydrogenation of CO_2*. (i) Inspite of the fact that formate pathway has already been discarded from our reaction scheme due to hindered energy barrier for ($CO_2 + H \rightarrow$ HCOO*) step, hydrogenation of HCOO* is studied to identify the substantial formation mechanism of (HCO* + OH*). Nevertheless, it is found that the bi-HCOO reacts with surface atomic H* via ER mechanism and forms (HCO* + OH*) with huge barrier of 1.97 eV, supporting our result that Ir clusters do not favour the formate pathway for methanol formation. (ii) The second approach of (HCO* + OH*) formation is through the direct hydrogenation of CO_2*; the process includes adsorbed CO_2, which has favorable binding energies on the Ir clusters, as calculated earlier, and H_2 molecule in gaseous state. Subsequently, following the LH mechanism, H_2 attacks on CO_2* and triggers the H-assisted C-O bond dissociation of CO_2* resulting in HCO* and OH*. This is concerted step involving formation of C-H and O-H bond with a simultaneous C-O bond breaking event. The corresponding reaction is highly exothermic (-1.20 eV (Ir_7); -0.90 eV (Ir_{13}); and -1.47 eV (Ir_{55}) with activation energy barriers of 0.1 eV (Ir_7), 0.38 eV (Ir_{13}) and 0.15 eV (Ir_{55}) recommending the second pathway as the plausible one for HCO* formation on Ir clusters. However, the other probable reactions, (HCOOH* → HCOO* + H*) and (HCOOH* → HCOH* + O*), have to overcome huge barriers of 1.94 eV and 2.90 eV for the respective dissociation along with high endothermicity of 2.56 eV and 3.1 eV on Ir_7 cluster. The much higher barriers are needed for these reactions on other clusters; hence most unlikely to happen on the Ir cluster.

The residual OH* is removed from the catalysts via water (H_2O) formation as discussed previously. It has been discussed in the previous literatures that HCO* is not very stable species and dissociates back into CO* and H* (HCO* → CO* + H*) on Cu surface as the backward reaction is easily accessible from thermodynamic (exothermic with energy of -0.73 eV) and kinetic (energy barrier of 0.15 eV) point of view. [75] But, interestingly in the present work, we have not found the tendency of HCO* to be dehydrogenated back; might be because of the favorable binding energies of HCO* on Ir cluster of -2.64 eV and very high activation energy barrier of 1.50 eV for the decomposition reaction. The immediate process is the hydrogenation of HCO* with surface atomic H* to form H_2CO^* via ER mechanism, (HCO* + H* → H_2CO^*); H_2CO^* binds to the Ir clusters via O and C atoms with moderate binding energies of Ir_7 (-2.45 eV); Ir_{13} (-2.50 eV); Ir_{55} (-2.40 eV). These values are inconsistent with the previous results on Cu (111) surface which report that adsorption energy of H_2CO is very low, in the range of -0.10 eV; even in some cases H_2CO desorbs out of the catalytic surfaces due to negligible interaction with the adsorbate.

---

[52] On the other hand, in agreement with our study, isotope labelling study over Cu/ZrO_2 concludes that CH_3OH is exclusively formed through H_2CO^*, not from $HCOO^*$.[69] However, according to Sabatier Principle, the moderate binding energy of H_2CO^* is required as an intermediate to carry out the reaction towards product highlighting the efficiency of Ir clusters as proficient catalyst for methanol synthesis. The kinetic energy barriers for H_2CO formation from HCO^* and H^* are Ir_7 (0.60 eV); Ir_{13} (0.75 eV) and Ir_{55} (0.87 eV) with endothermicity of 0.40 eV for all the three systems. Another approved path of H_2CO formation is via cleaving of C-O bond of H_2COO. Though the existence of H_2COO species is questionable and experimentally not confirmed, H_2COO^* has been widely assumed as an active intermediate for the methanol synthesis in quite a few number of studies. [5, 16, 65, 76] Our calculations show that hydrogenation of $HCOO^*$ to H_2COO^* is highly endothermic with kinetically restricted barrier height of 1.89 eV. Recent studies have also reported the high energy barriers of 1.20 eV and 1.60 eV for the ($HCOO^* + H^* \rightarrow H_2COO^*$) reaction by Zhao et al. and Liu and coworkers respectively; [53, 75] thus, the possibility of formation of H_2COO^* can be excluded in the present study.

The further hydrogenation step of H_2CO^* can be bifurcated into two final reaction intermediates, methoxy ($H_2CO^* + H^* \rightarrow H_3CO^*$) or H_2COH^* ($H_2CO^* + H^* \rightarrow H_2COH^*$); indeed, these are two isomers differing in the formation of C-H or O-H bonds exclusively. The activation energy barriers and reaction energies for ($H_2CO^* + H^* \rightarrow H_3CO^*$) step, i.e., C-H bond making are Ir_7 (E_a = 0.78 eV, E = 0.20 eV); Ir_{13} (E_a = 0.91 eV, E = 0.40 eV); Ir_{55} (E_a = 0.76 eV, E = 0.55 eV) and for ($H_2CO^* + H^* \rightarrow H_2COH^*$) step, i.e., O-H bond making are Ir_7 (E_a = 0.13 eV, E = -0.70 eV); Ir_{13} (E_a = 0.18

eV, E = -0.58 eV); Ir_{55} (E_a = 0.30 eV, E = -0.46 eV). So, the DFT results reflect that H_2COH^* path via LH-mechanism dominate both kinetically and thermodynamically dominates over OCH_3^* pathway on Ir clusters. Finally, hydrogenation of both the isomers (OCH_3^* and CH_2OH^*) converge into very same product, methanol, which is evidently the ultimate reduction step of CO_2 to methanol conversion process. The energy values of the corresponding step are as follows: for the protonation of OCH_3^* (Ir_7, E_a = 0.91 eV, E = 0.45 eV; Ir_{13}, E_a = 0.97 eV, E= 0.65 eV; Ir_{55}, E_a = 1.53 eV, E = 1.02 eV) and for the H_2COH hydrogenation (Ir_7, E_a = 0.60 eV, E = 0.23 eV; Ir_{13}, E_a = 0.86 eV, E = 0.47 eV; Ir_{55}, E_a = 1.00 eV , E = 0.51 eV). Both the elementary steps are endothermic, but H_2COH pathway is significantly more favourable than CH_3O pathway to form methanol. In fact, a large number of experimental and theoretical studies have been discussed in connection with the competition between OCH_3 and CH_2OH paths. An in situ FTIR study prescribed that CH_3O^* hydrogenation is the rate-limiting step on Cu/ZnO and Cu/ZnO/Cr_2O_3 catalyst in the course of methanol synthesis. [77] The corresponding activation energy barrier of 1.17 eV has been proposed for this step by Grabow et al. [52] which agrees with the high barrier calculated in the present situation for methoxy hydrogenation. The complete potential energy surface has been represented in Fig. 6.7, Fig. 6.8 and Fig. 6.9 for Ir_7, Ir_{13} and Ir_{55} respectively.

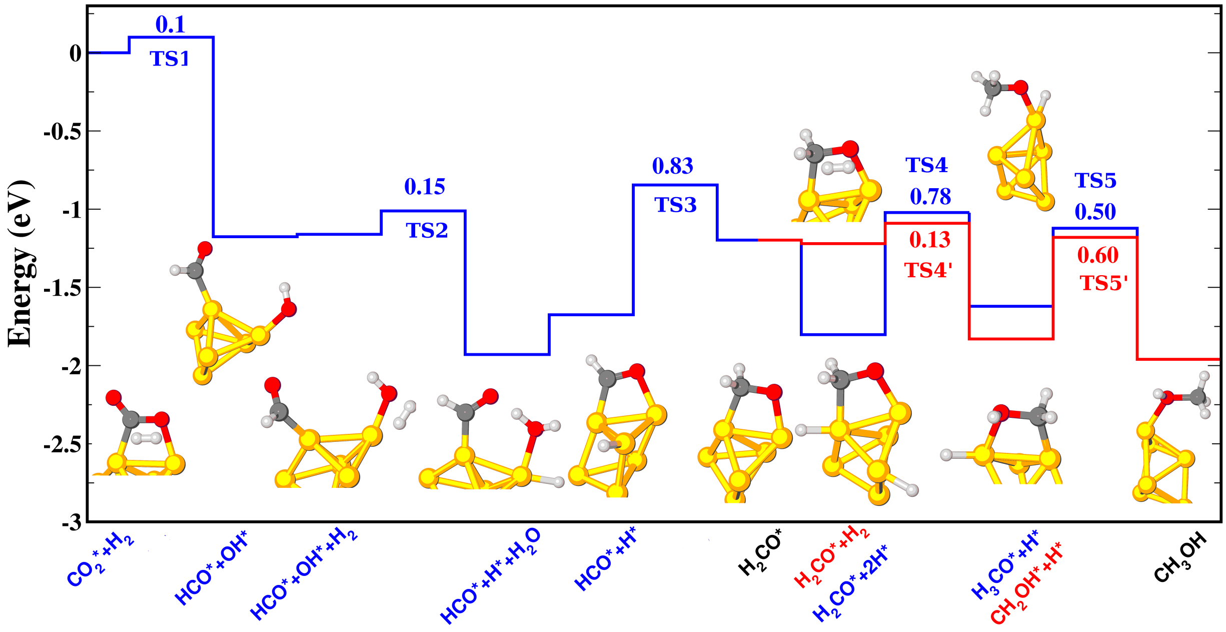

Figure 6.7: Potential energy profile of methanol synthesis by Ir_7 cluster

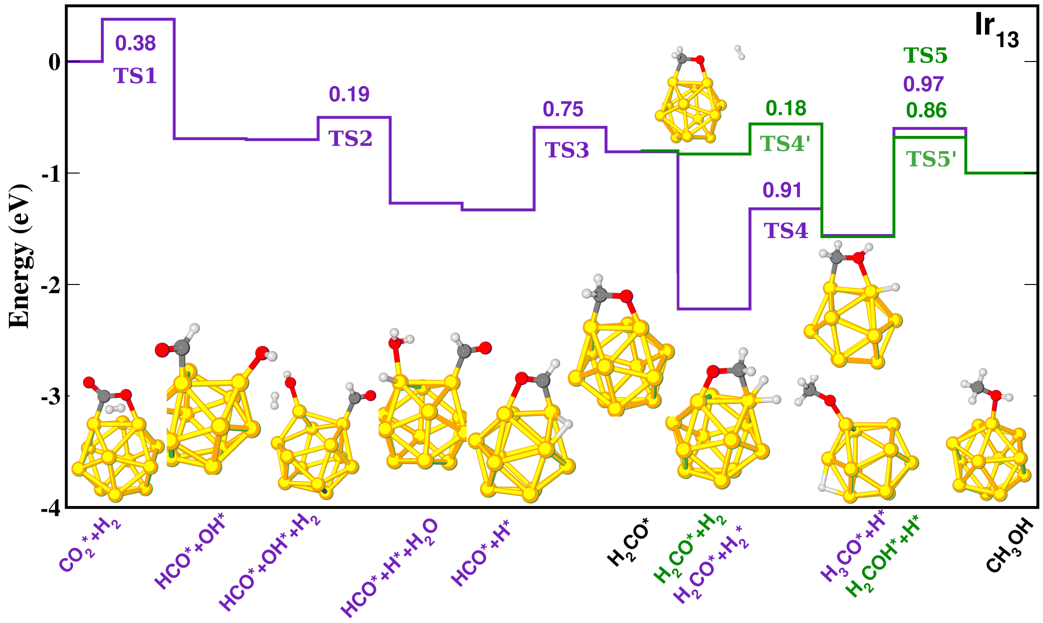

Figure 6.8: Potential energy profile of methanol synthesis by Ir_{13} cluster

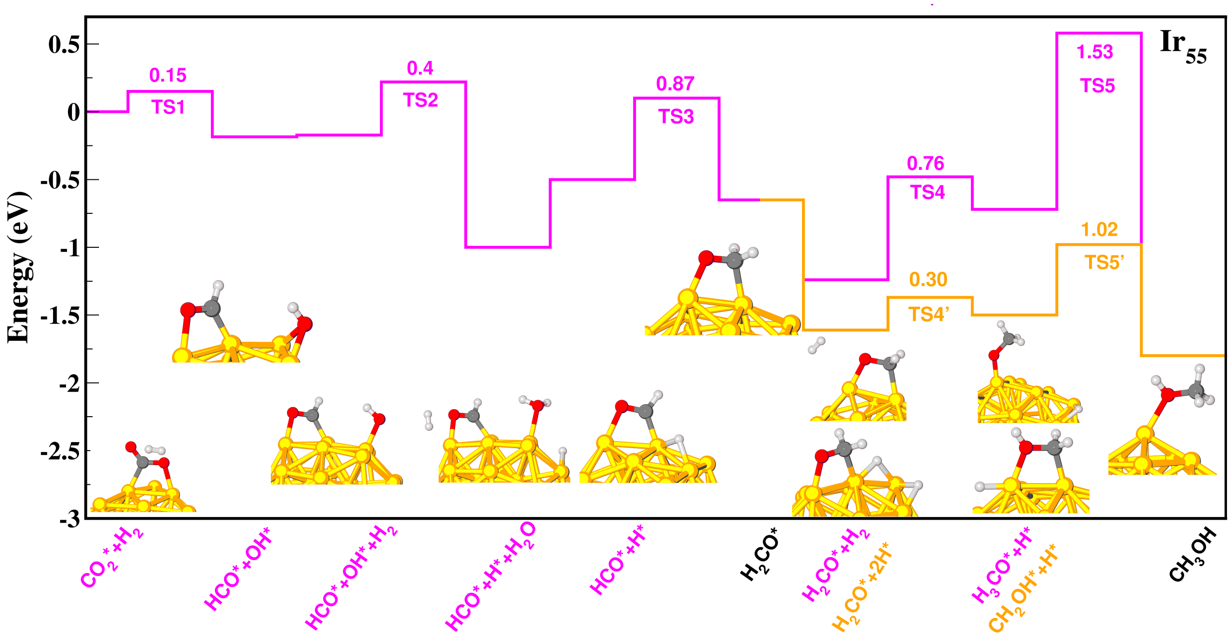

Figure 6.9: Potential energy profile of methanol synthesis by Ir_{55} cluster

Since water is a reaction product of methanol synthesis, the impact of water on the calculated reaction kinetics and energetics of the rate determining step has been investigated and surprisingly, the role of water in facilitating the reaction is noteworthy, in consistent with the previous findings. [55] As the conversion of methoxy to methanol is the highest energy path on Ir clusters, we have added one water molecule to this rate limiting step containing methoxy to see the effect of water in the overall kinetics of the reaction mechanism. (Fig. 6.10)

After optimisation, the attractive interaction between H_2O and adsorbed CH_3O^* promotes the hydrogen transfer process from water to methoxy by dramatically diminishing the the barrier height to 0.30 eV for Ir_7; 0.34 eV for Ir_{13} and 0.46 eV for Ir_{55} clusters. The reaction is slightly endothermic in the range of 0.06 eV, suggesting that the effect of water makes the reaction both

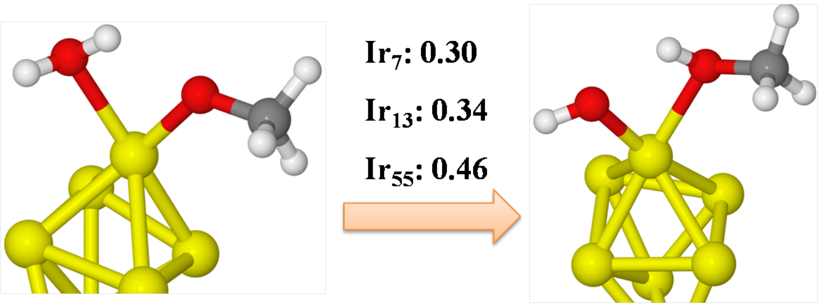

Figure 6.10: Optimized structures of some reaction intermediates involved in methanol synthesis through water mediated formic acid route on Ir cluster. The corresponding activation energies (in eV) are shown for each step. The color code is same as previously mentioned.

kinetically and thermodynamically feasible and acts efficiently as the H atom source for further hydrogenation. However, the water mediated reaction step follows, ($OCH_3^* + H_2O \rightarrow CH_3OH + OH^*$); the resulting products consist of methanol and hydroxyl, where the hydroxyl species can be removed from the surface in the form of water, as already discussed.

Our computational study shows that all the three Ir_7, Ir_{13} and Ir_{55} clusters follow the same HCOOH pathway to form methanol from CO_2 and H_2. However, there is significant difference in energetics along the reaction path and this can be attributed to the size of the Ir clusters. In general, the dependence of size on the catalytic activity has been ascribed to coordination number, quantum size, electron promotion etc. In short, smaller the size, more the number of the surface atoms and that means, presence of more number of coordinatively unsaturated sites which are indeed one of the major factors for the drastic change in the overall activity of a catalytic reaction. Interestingly, it has been perceived that the smallest Ir_7 cluster effectively brings down the activation energy barrier for each elementary steps of ($CO_2 + H_2 \rightarrow CH_3OH$) reaction in comparison to Ir_{13} and Ir_{55} clusters. Hence, these results clearly illustrate the need to consider the effect of catalyst particle-size in methanol synthesis reaction.

6.4 Conclusion

In summary, our work presents an extensive set of self-consistent density functional theory calculations to map out the three entire reaction network of CO_2 hydrogenation to methanol on Ir_7, Ir_{13} and Ir_{55} clusters. The result suggests that the formation of CO* from CO_2 can proceed either through direct C-O bond cleavage or via H assisted CO_2 dissociation reaction, i.e. RWGS route; both the routes are found to be competitive on Ir clusters with feasible kinetic and thermodynamic parameters. However, the further hydrogenation of CO* to HCO* or COH* is unlikely due to restricted activation energy barriers; hence it can be inferred that in the presence of Ir clusters, CO* does not participate in the process of $CO_2 \rightarrow CH_3OH$ conversion. Furthermore, a very high barrier height for the formation of formate (HCOO*) from CO_2 and H precludes HCOO*, H_2COO* species as key intermediates for the methanol synthesis. According to our computational study, CO_2 can be converted into CH_3OH through HCOOH intermediate which forms via direct hydrogenation of CO_2* following LH-mechanism. In fact, it has been found that HCOOH spontaneously dissociates on Ir clusters by splitting off its OH group and results in HCO* intermediate, which plays a crucial role to advance the reaction towards the product, methanol. The further hydrogenation of HCO* preferentially leads to H_2CO* intermediate. The present work finds that Ir clusters fulfil the basic criteria of adsorbing the key intermediates, e.g., HCO* and

H_2CO^* quite strongly so that these species can move the reaction to forward direction. Finally, H_2CO^* to CH_3OH path has been bifurcated into two ways, H_2COH^* and H_3CO^*; the former track is turned out to be more favorable due to lower hydrogenation barrier. However, we demonstrate an important role of H_2O in the methanol synthesis, particularly for the $H_3CO^* \rightarrow CH_3OH$ step where H_2O effectively reduces the kinetic energy barrier through hydrogen transfer process, i.e., by donating one of its proton to the surface methoxy. Our findings show that Ir_7 cluster display higher activity in CH_3OH production than Ir_{13} and Ir_{55} clusters with low activation energy barriers for the elementary steps. The observed tailoring of the properties of small metal clusters by alteration of the size of the cluster can render some clues to the development of novel Ir cluster- based catalysts for the improvement of the CO_2 hydrogenation performance.

Bibliography

[1] G. A. Olah, G. K. S. Prakash and A. Goeppert, *J. Am. Chem. Soc.*, 2011, **133**, 12881–12898.

[2] A. Goeppert, M. Czaun, J. P. Jones, G. K. Surya Prakash and G. A. Olah, *Chem. Soc. Rev.*, 2014, **43**, 7995–8048.

[3] G. A. Olah, A. Goeppert and G. K. S. Prakash, *J. Org. Chem.*, 2009, **74**, 487–498.

[4] W. Wang, S. Wang, X. Ma and J. Gong, *Chem. Soc. Rev.*, 2011, **40**, 3703–3727.

[5] T. Askgaard, J. Norskov, C. Ovesen and P. Stoltze, *J. Catal.*, 1995, **156**, 229–242.

[6] D. Cheng, F. R. Negreiros, E. Apra and A. Fortunelli, *ChemSusChem*, 2013, **6**, 944–965.

[7] K. C. Waugh, *Catal. Today*, 1992, **15**, 51 – 75.

[8] G. Meitzner and E. Iglesia, *Catal. Today*, 1999, **53**, 433 – 441.

[9] A. Bansode and A. Urakawa, *J. Catal.*, 2014, **309**, 66 – 70.

[10] P. Szuromi, *Science*, 2014, **345**, 526–527.

[11] M. Behrens, F. Studt, I. Kasatkin, S. Kuhl, M. Havecker, F. Abild-Pedersen, S. Zander, F. Girgsdies, P. Kurr, B. Kniep, M. Tovar, R. W. Fischer, J. K. Norskov and R. Schlogl, *Science*, 2012, **336**, 893–897.

[12] M. Behrens, *J. Catal.*, 2009, **267**, 24 – 29.

[13] X. M. Liu, G. Q. Lu, Z. F. Yan and J. Beltramini, *Ind. Eng. Chem. Res.*, 2003, **42**, 6518–6530.

[14] Q. Tang, Q. Hong and Z. Liu, *J. Catal.*, 2009, **263**, 114 – 122.

[15] Y. Choi, K. Futagami, T. Fujitani and J. Nakamura, *Appl. Catal., A*, 2001, **208**, 163 – 167.

[16] C. Ovesen, B. Clausen, J. Schiotz, P. Stoltze, H. Topsoe and J. Norskov, *J. Catal.*, 1997, **168**, 133 – 142.

[17] A. J. Medford, J. Sehested, J. Rossmeisl, I. Chorkendorff, F. Studt, J. Norskov and P. Moses, *Journal of Catalysis*, 2014, **309**, 397 – 407.

[18] *Appl. Catal., B*, 2014, **152153**, year.

[19] J. Toyir, P. R. de la Piscina, J. Llorca, J. G. Fierro and N. Homs, *Phys. Chem. Chem. Phys.*, 2001, **3**, 4837–4842.

[20] T. Fujitani, M. Saito, Y. Kanai, T. Kakumoto, T. Watanabe, J. Nakamura and T. Uchijima, *Catal. Lett.*, 1994, **25**, 271–276.

[21] A.-P. F. E. C. F. H. J. S. D. S. C. I. N. J. K. Studt Felix, Sharafutdinov Irek, *Nat. Chem.*, 2014, **6**, 1755–4330.

[22] F. J. Fernandez-Alvarez, M. Iglesias, L. A. Oro and V. Polo, *ChemCatChem*, 2013, **5**, 3481–3494.

[23] H. et all., *Nat. Chem.*, 2012, **4**, 383–388.

[24] S. Sato, T. Morikawa, T. Kajino and O. Ishitani, *Angew. Chem. Int. Ed.*, 2013, **52**, 988–992.

[25] R. Tanaka, M. Yamashita and K. Nozaki, *J. Am. Chem. Soc.*, 2009, **131**, 14168–14169.

[26] S. E. Deutsch, G. Mestl, H. Knozinger and B. C. Gates, *J. Phys. Chem. B*, 1997, **101**, 1374–1384.

[27] A. Uzun, D. A. Dixon and B. C. Gates, *ChemCatChem*, 2011, **3**, 95–107.

[28] C. Kerpal, D. Harding, G. Meijer and A. Fielicke, *EPJ D*, 2011, **63**, 231–234.

[29] C. Bussai, S. Kruger, G. N. Vayssilov and N. Rosch, *Phys. Chem. Chem. Phys.*, 2005, **7**, 2656–2663.

---

[30] V. Stevanovic, Z. Sljivancanin and A. Baldereschi, *J. Phys. Chem. C*, 2010, **114**, 15653–15660.

[31] T. Pawluk, Y. Hirata and L. Wang, *J. Phys. Chem. B*, 2005, **109**, 20817–20823.

[32] J. Du, X. Sun, J. Chen and G. Jiang, *J. Phys. Chem. A*, 2010, **114**, 12825–12833.

[33] M. Chen and D. A. Dixon, *J. Phys. Chem. A*, 2013, **117**, 3676–3688.

[34] B. K.G.Caultont, M.G.Thomas and E.L.Muettertiest, *Proc. Natl. Acad. Sci. USA*, 1976, **73**, 4274–4276.

[35] L. P.-A. G. Y. K. N. J. H. Li, H.; Li and X. C. Zeng, *Nano Lett.*, **15**, 682–688.

[36] Y. Gao, N. Shao, Y. Pei, Z. Chen and X. C. Zeng, *ACS Nano*, 2011, **5**, 7818–7829.

[37] L. Li, Y. Gao, H. Li, Y. Zhao, Y. Pei, Z. Chen and X. C. Zeng, *J. Am. Chem. Soc.*, 2013, **135**, 19336–19346.

[38] A. Endou, N. Ohashi, K. Yoshizawa, S. Takami, M. Kubo, A. Miyamoto and E. Broclawik, *J. Phys. Chem. B*, 2000, **104**, 5110–5117.

[39] J. Lu, P. Serna, C. Aydin, N. D. Browning and B. C. Gates, *J. Am. Chem. Soc.*, 2011, **133**, 16186–16195.

[40] G. P. Petrova, G. N. Vayssilov and N. Rosch, *Catal. Sci. Technol.*, 2011, **1**, 958–970.

[41] Y. Motoyama, M. Taguchi, N. Desmira, S.-H. Yoon, I. Mochida and H. Nagashima, *Chem Asian J*, 2014, **9**, 71–74.

[42] C. A. Stowell and B. A. Korgel, *Nano Lett.*, 2005, **5**, 1203–1207.

[43] P. Giannozzi, S. Baroni, N. Bonini, M. Calandra, R. Car, C. Cavazzoni, D. Ceresoli, G. L. Chiarotti, M. Cococcioni, I. Dabo, A. Dal Corso, S. de Gironcoli, S. Fabris, G. Fratesi, R. Gebauer, U. Gerstmann, C. Gougoussis, A. Kokalj, M. Lazzeri, L. Martin-Samos, N. Marzari, F. Mauri, R. Mazzarello, S. Paolini, A. Pasquarello, L. Paulatto, C. Sbraccia, S. Scandolo, G. Sclauzero, A. P. Seitsonen, A. Smogunov, P. Umari and R. M. Wentzcovitch, *J. Phys. Condens. Matter*, 2009, **21**, 395502 (19pp).

[44] J. P. Perdew, K. Burke and M. Ernzerhof, *Phys. Rev. Lett.*, 1996, **77**, 3865–3868.

[45] D. Vanderbilt, *Phys. Rev. B*, 1990, **41**, 7892–7895.

[46] G. Henkelman, B. P. Uberuaga and H. Jonsson, *J. Chem. Phys.*, 2000, **113**, 9901–9904.

[47] G. Henkelman and H. Jonsson, *J. Chem. Phys.*, 2000, **113**, 9978–9985.

[48] P. Maragakis, S. A. Andreev, Y. Brumer, D. R. Reichman and E. Kaxiras, *J. Chem. Phys.*, 2002, **117**, 4651–4658.

[49] G. Mills and H. Jónsson, *Phys. Rev. Lett.*, 1994, **72**, 1124–1127.

[50] J. K. Norskov, F. Abild-Pedersen, F. Studt and T. Bligaard, *Proc. Natl. Acad. Sci. USA*, 2011, **108**, 937–943.

[51] P. L. Hansen, J. B. Wagner, S. Helveg, J. R. Rostrup-Nielsen, B. S. Clausen and H. Topsoe, *Science*, 2002, **295**, 2053–2055.

[52] L. C. Grabow and M. Mavrikakis, *ACS Catal.*, 2011, **1**, 365–384.

[53] C. Liu and P. Liu, *ACS Catal.*, 2015, **5**, 1004–1012.

[54] J. Ye, C. Liu, D. Mei and Q. Ge, *J. Catal.*, 2014, **317**, 44 – 53.

[55] Q.-L. Tang, W.-T. Zou, R.-K. Huang, Q. Wang and X.-X. Duan, *Phys. Chem. Chem. Phys.*, 2015, **17**, 7317–7333.

[56] G. J. Millar, C. H. Rochester and K. C. Waugh, *Catal. Lett.*, 1992, **14**, 289–295.

[57] M. Bowker, R. A. Hadden, H. Houghton, J. N. . K. Hyland and K. C. Waugh, *J. Catal.*, 1988, **109**, 263 – 273.

[58] G. C. Chinchen, M. S. Spencer, K. C. Waugh and D. A. Whan, *J. Chem. Soc., Faraday Trans. 1*, 1987, **83**, 2193–2212.

[59] I. A. Fisher and A. T. Bell, *J. Catal.*, 1997, **172**, 222 – 237.

[60] T. Yatsu, H. Nishimura, T. Fujitani and J. Nakamura, *J. Catal.*, 2000, **191**, 423 – 429.

[61] T. Fujitani, Y. Choi, M. Sano, Y. Kushida and J. Nakamura, *J. Phys. Chem. B*, 2000, **104**, 1235–1240.

[62] G. J. Millar, C. H. Rochester, C. Howe and K. . C. Waugh, *Mol. Phys.*, 1992, **76**, 833–849.

[63] H. Nakano, I. Nakamura, T. Fujitani and J. Nakamura, *J. Phys. Chem. B*, 2001, **105**, 1355–1365.

[64] H. Nishimura, T. Yatsu, T. Fujitani, T. Uchijima and J. Nakamura, *J. Mol. Catal. A: Chem.*, 2000, **155**, 3 – 11.

[65] K. C. Waugh, *Solid State Ionics*, 2004, **168**, 327 – 342.

[66] A. B. Ilva, K. Wolfgang and T. Fritz, *Surf. Sci.*, 1994, **307-309**, 177 – 181.

[67] A. F. Carley, M. W. Roberts and A. J. Strutt, *J. Phys. Chem.*, 1994, **98**, 9175–9181.

[68] N. Schumacher, k. Andersson, L. Grabow, M. Mavrikakis, J. Nerlov and I. Chorkendorff, *Surf. Sci.*, 2008, **602**, 702 – 711.

[69] E. Ortelli, J. Weigel and A. Wokaun, *Catal. Lett.*, 1998, **54**, 41–48.

[70] J. Weigel, R. A. Koeppel, A. Baiker and A. Wokaun, *Langmuir*, 1996, **12**, 5319–5329.

[71] Y. Yang, C. A. Mims, R. S. Disselkamp, J.-H. Kwak, C. H. F. Peden and C. T. Campbell, *J. Phys. Chem. C*, 2010, **114**, 17205–17211.

[72] P. Taylor, P. Rasmussen and I. Chorkendorff, *J. Chem. Soc., Faraday Trans.*, 1995, **91**, 1267–1269.

[73] B. Hayden, K. Prince, D. Woodruff and A. Bradshaw, *Surf. Sci.*, 1983, **133**, 589 – 604.

[74] M. Bowker and R. Madix, *Surf. Sci.*, 1981, **102**, 542 – 565.

[75] Y.-F. Zhao, Y. Yang, C. Mims, C. H. F. Peden, J. Li and D. Mei, *J. Catal.*, 2011, **281**, 199 – 211.

[76] P. Rasmussen, P. Holmblad, T. Askgaard, C. Ovesen, P. Stoltze, J. Norskov and I. Chorkendorff, *Catal. Lett.*, 1994, **26**, 373–381.

[77] J. F. Edwards and G. L. Schrader, *J. Catal.*, 1985, **94**, 175 – 186.

Chapter 7

7(a):Conversion of CO_2 to HCOOH on Ni(100) Surface

7(b):Effect of Support for the Conversion of HCOOH to CO_2 on $AgPd_{13}$ cluster

Contents

7.1 Conversion of CO_2 to HCOOH

The chemical transformation of CO_2 into useful feedstock and chemicals becomes an important strategy that not only removes greenhouse gas from the atmosphere, but also reduces the dependence on fossil fuels. In this context, considerable progress has been made in past few decades and several processes have been commercialized. However, human activity throughout the world contributes about 35GT of CO_2 to the atmosphere per year and there is an evident gap between the amount of CO_2 produced and the amount consumed. Hence, ideally a multitude of chemical products should be derived from CO_2 to mitigate this gap.[1, 2] Among many, a very important one is formic acid, since it may be used as chemical feedstock and as well as fuel.[3–5] It is one of the very useful chemicals which is widely used in making animal feeds, in tanning, dyeing leather, textiles, as a food preservative etc. Nevertheless, formation of formic acid from direct CO_2 hydrogenation is a difficult process because of the high kinetic and thermodynamic stability of CO_2. In fact, due to an entropic contribution, the gas phase reaction has a positive ΔG value (ΔG_0 = +33KJmol^1).[6]

Several catalysts have been proposed for this particular process of CO_2 conversion to HCOOH. Marvikakis and co-workers [7, 8]investigated hydrogenation of CO_2 on Cu(111) and Pt(111) surfaces in the framework of their studies of water gas shift(WGS) reaction and its reverse reaction. It has been found that formate, one of the intermediates involved in formic acid production, acts as a spectator species for WGS reaction. The corresponding activation energy barriers are 1.02 eV and 1.39 eV on Cu(111) and Pt(111)surafces, respectively. Recently, it was found that CO_2 can be hydrogenated to formate on Ni(110) surface under ultrahigh-vacuum (UHV) conditions, but the further hydrogenation of HCOO to HCOOH was not observed.[9] So, the nature of the involved intermediates and feasibility of the formation of the final product are directly related to the catalyst used for a particular reaction. Hence, a complete microscopic understanding of the reaction pathway and its associated energetics for hydrogenation of CO_2 to HCOOH is of great interest.

The computational investigation of CO_2 hydrogenation on Ni(111)[10] and Ni(110)[11] surfaces has been thoroughly accomplished. However, to the best of our knowledge, there is no theoretical study present which shows the tendency of Ni(100) surface towards ($CO_2 + H_2 \rightarrow HCOOH$) reaction as a catalyst. In this study, we are going to focus on the CO_2 hydrogenation with H adsorbed on Ni(100) surface. The detailed reaction mechanism and potential energy surface for the CO_2 hydrogenation to formate(HCOO)/carboxyl(COOH) intermediate and further to the final product, formic acid has been explored. The competition between the formate or carboxyl mediated hydrogenation pathway on Ni(100) surface has been discussed.

7.1.1 Computational Details

All the calculations have been performed using the Quantum Espresso code [12] based on spin-polarized density functional theory. Throughout the work, the generalized gradient approximation (GGA-PBE) was used to describe the exchange-correlation functional.[13] The ionic cores have been taken care by the ultrasoft pseudopotentials obtained from the publicly available repository of the Quantum Espresso distribution. The electron wave functions were expanded with plane waves with an energy cutoff of 400 eV. The Ni(100) surface was modeled by a five-layer slab with a (3×3) surface unit cell separated from its image in the z-direction by a vacuum of 12 Å. vacuum to avoid any spurious interactions. Brillouin zone sampling was used with Monkhorst-Pack scheme and the k-point grid of 4×4×1 have been chosen for all the calculations.[14] The two bottom-most Ni(100) layers were kept fixed during relaxation. All structures were completely relaxed until the HellmannFeynman forces acting on the atoms were less than 0.05 eV/. The climbing image nudged elastic band (CI-NEB) method [15] was employed to calculate the activation energy barriers for the various elementary steps considered. The binding energy (Δ) is defined as

$$\Delta = E_{ads} - E_{clean} - E_{gas} \tag{7.1}$$

where E_{ads}, E_{clean}, and E_{gas} are the calculated total energies of the slab with adsorbate, the clean slab, and the adsorbate species in the gas phase, respectively. All the calculations were spin polarized and a ferromagnetic phase was adopted for Ni(100). The calculated lattice constant of Ni is 3.52 Å, in good agreement with the experimental value of 3.524 Å.

7.1.2 Results and discussion

7.1.2.1 Adsorption and Coadsorption of H and CO_2

First, we studied the adsorption and co-adsorption of CO_2 and atomic H(H) on Ni(100) surface. For H adsorption, The fcc hollow site is found to be the most favourable site for a hydrogen atom to be adsorbed with binding energy of -0.56 eV. Next, stable site is the bridge site which is less stable by 0.1 eV compared to fcc hollow site. For CO_2, it has been found that the most favourable adsorption site is 3-fold hollow site with exothermic chemisorption energy of -0.13 eV. The corresponding adsorbed CO_2 moiety has a bent structure with $\angle$ OCO of about 135^0 and the C-O bonds are elongated to 1.264 Åand 1.257 Å. On the other hand, the binding energies of CO_2 at 2-fold bridge site and 2-fold long-bridge site are slightly positive (0.10 eV and 0.02 eV, respectively) indicating thermally neutral chemisorption of CO_2. For H and CO_2 co-adsorption, the interaction energy has been found to be very low (0.06 eV) between these two adsorbed species.

7.1.2.2 CO_2 hydrogenation with surface H

After identifying the adsorbed and co-adsorbed structures of H and CO_2, we move to the hydrogenation of CO_2 on Ni(100) surface. There are two possible routes for the hydrogenation of CO_2 to formic acid; either via (i) formate route (HCOO) where hydrogenation occurs at carbon atom of CO_2 or via (ii) carboxylic route (COOH), where one of the oxygen atom of CO_2 gets hydrogenated. Our calculations indicate that formate intermediate in its most stable bidentate form (with two O atoms of HCOO** bound to the two surface

Ni atoms at atop site) is energetically more favourable than the most stable trans configuration of COOH intermediate (with H atom of COOH pointing towards the surface) by 0.7 eV. However, this is opposite to what is observed for gas phase structures of these species, where COOH is found to be more stable than HCOO species by 0.4 eV. [16] We first investigate the hydrogenation of CO_2 to formate. The associated potential energy surface of $CO_2 \rightarrow HCOOH$ conversion via HCOO intermediate is shown in Fig. 7.1.

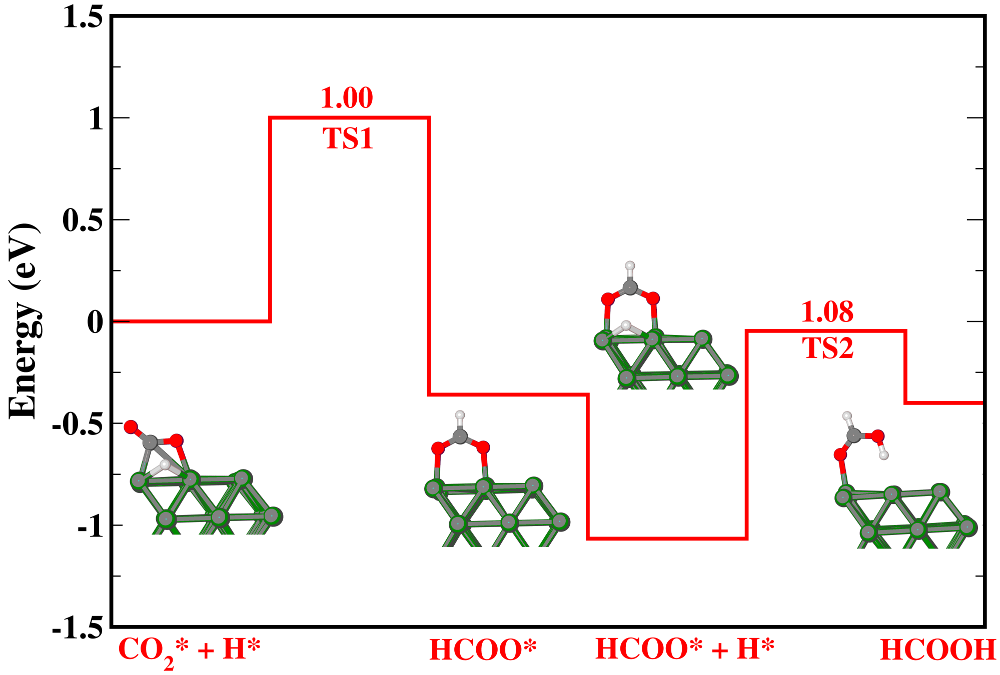

Figure 7.1: Potential energy surface (PES) of hydrogenation of CO_2 to formic acid (HCOOH) via formate intermediate (HCOO) with adsorbed H on Ni(100) surface. The atomic structures of reactants, intermediates and products are depicted in the respective insets. H, C, O and Ni atoms are represented by white, grey, red and green color, respectively.

The very first hydrogenation step of CO_2 to HCOO is exothermic by 0.36 eV and has been characterized by an activation energy barrier of 1 eV. The minimum energy path involves the approach of atomic H towards C of adsorbed CO_2 for forming H-C bond, followed by a 90^0 rotation of HCOO intermediate. It should be noted that the barrier height for the formate formation on Ni(100) (1 eV) surface is higher than that for the similar reaction on Ni(111) (0.62 eV) and Ni(110) (0.41 eV) surfaces. We then consider the further hydrogenation of formate to produce formic acid, the desired final product. The most stable site for the formic acid adsorption is atop. The activation energy barrier for HCOO → HCOOH conversion on Ni(100) surface is 1.03 eV, which is nearly identical to the previous hydrogenation step ($CO_2 \rightarrow$ HCOO). Nevertheless, unlike previous case, the associated process is endothermic by 0.6 eV. According to the previous studies, on Ni(110) and Ni(111) surfaces, this H-addition step is characterized by activation energy barriers of 1.03 eV and 0.83 eV respectively. [10, 11] The respective reaction coordinate for the following reaction involves HCOO rotation toward H and diffusion of atomic H to the neighbouring bridge site to form the final O-H bond of HCOOH.

Next, we consider the alternative route for hydrogenation of CO_2 via carboxyl (COOH) intermediate on Ni(100) surface. Our computation suggests that on Ni(100) surface, COOH intermediate prefers to be adsorbed on bridge site. The complete potential energy surface for the hydrogenation of CO_2 to HCOOH via COOH intermediate has been shown in Fig. 7.2.

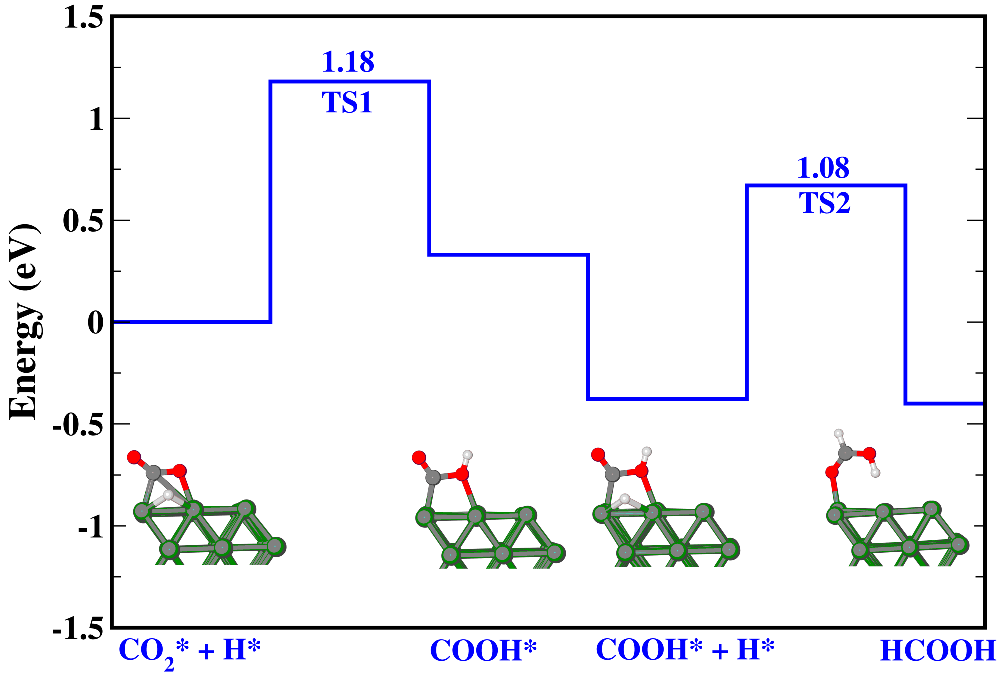

Figure 7.2: Potential energy surface (PES) of hydrogenation of CO_2 to formic acid (HCOOH) via carboxyl intermediate (COOH) with adsorbed H on Ni(100) surface. The atomic structures of reactants, intermediates and products are depicted in the respective insets. H, C, O and Ni atoms are represented by white, grey, red and green color, respectively.

The activation energy barrier for the carboxyl formation is 1.17 eV which is evidently 0.17 eV higher than the respective barrier for the $CO_2 \rightarrow HCOO$ conversion. Moreover, this reaction is endothermic by 0.33 eV. The inferior thermochemical stability and higher barrier height for the formation of carboxyl intermediate compared to formate prescribes that the hydrogenation route via formate is more preferable on Ni(100) surface. However, the subsequent hydrogenation reaction ($COOH \rightarrow HCOOH$) follows hydrogen diffusion step with energy barrier of 1.08 eV and the associated reaction is exothermic by 0.02 eV.

7.1.3 Conclusions

In summary, we presented a periodic, self-consistent DFT study for hydrogenation of CO_2 to HCOOH on Ni(100) surface. The first hydrogenation of CO_2 needs activation energy barrier of 1 eV to form formate, whereas the alternative route for CO_2 hydrogenation is characterized by relatively larger barrier (1.17 eV). Hence, our calculations show that hydrogenation of CO_2 to formate is more favourable than that of carboxyl intermediate. The second hydrogenation process from both the intermediates, i.e., HCOO → HCOOH or COOH → HCOOH require nearly identical amount of activation energy (1.08 eV) to reach the final product. Our results give useful insights into the probable path for CO_2 hydrogenation on Ni(100) surface which might have potential implications for the other catalytic reactions.

7.2 Conversion of HCOOH to CO_2

Hydrogen is widely expected to perform a crucial role in the future energy landscape to satisfy the increasing demand for a sustainable and clean energy supply. [17] Though many possible ways exist for obtaining hydrogen from both renewable and non-renewable sources on a large industrial scale, but the practical implementation of completely hydrogen-powered society is still beyond the horizon. Since, H_2 exists in a gaseous state at normal temperature and pressure, hydrogen storing process suffers from significant concerns, e.g. safety issues, low energy densities and a loss of hydrogen. A promising direction for solving these issues is to develop a technique where H_2 which is stored in a chemical form as a liquid organic compound can be extracted on-demand at room temperature.

A suitable hydrogen storage compound should possess high hydrogen content with the characteristic of convenient hydrogen release. In this aspect, formic acid (HCOOH), a major by-product of biomass processing, has been identified as an assuring candidate for hydrogen storage. Formic acid is a liquid at room temperature which contains 4.4 % (w/w) of hydrogen with a volumetric capacity of 53.4 g/L at standard temperature and pressure (STP).[4, 18] Moreover, it is also found to be relatively low in toxicity, with a LD50 (oral, rat) value of 1100 mg/kg. Precisely, HCOOH is one of the best options which is good in transportation, refilling, and safety issues; thus fulfils all the criteria of a promising hydrogen storage material. [3, 19]

Stored H_2 of HCOOH can be produced via decomposition reaction which can follow two possible pathways:

$$HCOOH \rightarrow CO_2 + H_2 : \Delta G = -48.4kJmol^{-1} \tag{7.2}$$

$$HCOOH \rightarrow CO + H_2O : \Delta G = -28.5kJmol^{-1} \tag{7.3}$$

Evidently, for direct applications in fuel cells, HCOOH should be decomposed via former pathway, i.e., dehydrogenation pathway (equation(7.2)), rather than dehydration pathway (equation(7.3)) to selectively get a high quantity of H_2 and CO_2 at ambient conditions and prevent any CO formation that can poison the catalysts. Interestingly, the preference of the pathway is highly dependent on the catalyst used for the reaction. A wide range of both homogeneous and heterogeneous catalysts have been proposed for the decomposition of formic acid. In terms of heterogenous catalysts, bimetallic catalysts have been proposed to be more active than their single component counterparts for the dehydrogenation of HCOOH. Among many transition metals,[20–23] Ag, Pd, and their bimetallic nanoparticles, e.g., AgPd alloy, AgPd coreshell, and monodisperse AgPd alloy NPs are considered to be the most effective catalysts for this reaction.[24–27] It has been shown that coreshell nanoparticles consisting of an ultrathin Pd shell on a Ag core dramatically enhance the hydrogen production, but with no CO contamination from formic acid in an aqueous phase at ambient temperature. This is due to the large difference between the work function of Ag and Pd which gives rise to strong electron promotion to the Pd shell and that results in the highest activity of Ag-Pd core-shell nanoparticle. Most recently, Sen and co-workers have confirmed the high activity of AgPd alloy NPs supported on Ketjen carbon towards this reaction at 323 K.[27] Zhou et al. have recommended that Pd/Ag alloys supported on activated carbon are promising catalyst for the decomposition of aqueous solutions of formic acid containing sodium formate at low temperature (365 K). [24] However, it has been also demonstrated experimentally that catalytic property is not merely a function of a metal, it also highly depends on support which acts as a host of the catalyst. Actually, the electronic and/or geometric properties of a catalyst can be substantially modified by a suitable support. That is why an intensive research was devoted to determine a proper support towards obtaining better activity and selectivity of a catalyst. [28–31] In view of these findings, it seems very attractive to obtain further insight in this controversial issue, and to also gain a complete picture on how different supports tailor the activity and selectivity of a catalyst for a specific reaction. In this work, using DFT calculations, we have systematically investigated the detailed mechanism for the dehydrogenation and dehydration pathways of HCOOH decomposition on $AgPd_{13}$ cluster. To illustrate the effect of support on the catalytic property, we study the HCOOH decomposition reaction on bare, graphene and BN supported $AgPd_{13}$ cluster. We demonstrate that the support can dramatically alter the activity and/or selectivity of the $AgPd_{13}$ cluster for formic acid decomposition. The results are expected to understand the influence of support on the mechanism of HCOOH oxidation over $AgPd_{13}$ cluster at the molecular level which can serve as a foundational prototype to probe into the complex HCOOH oxidation on other catalyst systems.

7.2.1 Computational Details

Geometry optimization and total energy calculations have been carried out with density functional theory (DFT) framework as implemented in Quantum Espresso [12]. Throughout the work we used generalized gradient approximation (GGA) using PW91.[32] functional. The ionic cores were described by the ultrasoft pseudopotentials taken from the publicly available repository of the Quantum Espresso distribution. Brillouin zone sampling was performed with Monkhorst-Pack scheme [14] and the k-point grid of 3×3×1 have been used for all the calculations. The Kohn-Sham wave-functions were expanded with a plane wave basis sets with a kinetic energy cutoff of 30 Ryd. Electronic occupancies were allowed by using an energy smearing of 0.01 Ryd of Marzari-Vanderbilt scheme. Both the graphene and BN monolayers, which are used as substrates in the present study were modeled as periodic (5×5) unit cells to place $AgPd_{13}$ cluster. To describe the isolated cluster, the distance between two periodic images of the clusters have been maintained almost 10 Åwith vacuum of 15 Åin the direction perpendicular to the slab for avoiding any fictitious interactions among the nighbouring images. Adsorption calculations have been performed with adsorbate species adsorbed on only one side of the system. All of the atomic coordinates of considered systems were optimized until the forces on each atom become less than 0.001 eV/Ang. The binding energy (Δ) is defined as

$$\Delta = E_{total} - E_{clean} - E_{gas} \tag{7.4}$$

where E$_{total}$, E$_{clean}$, and E$_{gas}$ are the calculated total energies of the slab with adsorbate, the clean slab, and the adsorbate species in the gas phase, respectively. The atomic structures of bare, graphene and BN supported AgPd$_{13}$ cluster have been schematically illustrated in Fig. 7.3.

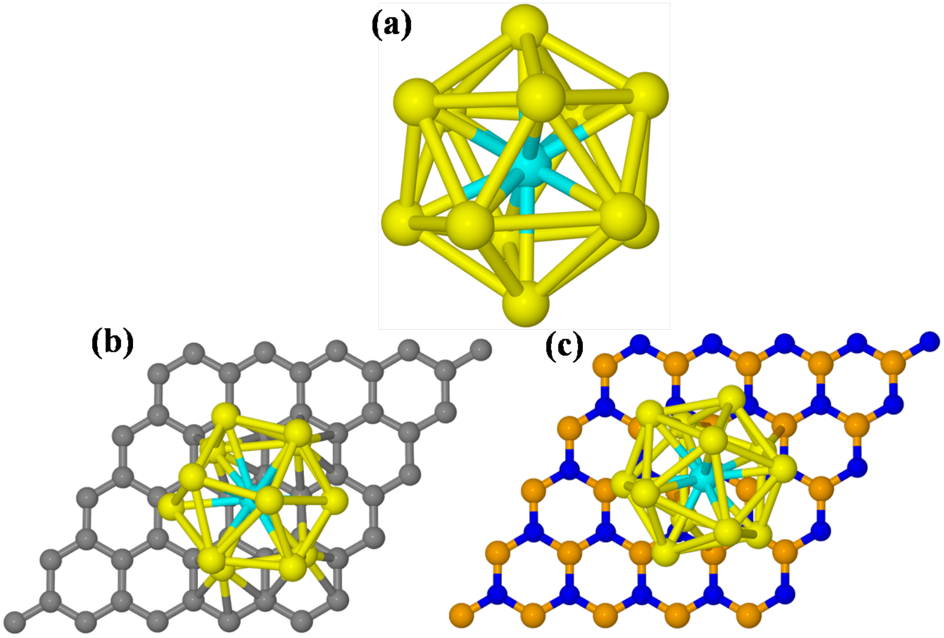

Figure 7.3: Optimized structures of (a) bare AgPd$_{13}$ cluster, (b) graphene supported AgPd$_{13}$ cluster and (c) BN supported AgPd$_{13}$ cluster. Ag, Pd, C, B and N atoms are shown as cyan, yellow, grey, orange and blue spheres, respectively.

7.2.2 Results and Discussion

To see the stability of the cluster on graphene and BN monolayers, we start by calculating the binding energies of AgPd$_{13}$ cluster on these supports. The exothermic binding energies of AgPd$_{13}$ cluster on both the supports indicate the favourable adsorption of the cluster on graphene and BN monolayers. However, the adsorption is found to be much stronger on graphene(-1.89 eV) in

Table 7.1: Binding energies (eV) of HCOOH, HCOO, COOH, CO, OH, O, C and H on bare AgPd$_{13}$ cluster, graphene supported AgPd$_{13}$ cluster and BN supported AgPd$_{13}$ cluster.

Model structure	HCOOH	HCOO	COOH	CO	OH	O	C	H
Bare AgPd$_{13}$	-0.27	-3.02	-2.67	-2.17	-3.39	-1.55	-5.60	-0.50
Graphene/AgPd$_{13}$	-0.55	-3.14	-2.75	-2.01	-4.00	-1.61	-5.66	-0.66
BN/AgPd$_{13}$	-0.39	-3.34	-2.88	-1.97	-3.67	-1.65	-5.70	-0.67

comparison to BN(-1.60 eV) system by almost 0.30 eV.

Next, we have considered the tendency of adsorption of all the reaction species involved in the complete process of formic acid decomposition. The corresponding binding energies of HCOOH*, HCOO*, COOH*, CO*, OH*, C*, O* and H* are listed in Table 7.1. The considerable negative values of the binding energies clearly suggest that the adsorbates get chemisorbed on the AgPd$_{13}$ cluster(both, bare and supported). However, we did not find any general trend of the adsorbates for preferentially strong or weak binding on an individual system considered. It can be seen from the binding energy values that except OH*, the difference in binding of all the other adsorbates on bare or supported AgPd$_{13}$ is less than or within 0.1-0.2 eV.

Scheme 1: The Reaction Mechanism of Formic Acid Decomposition

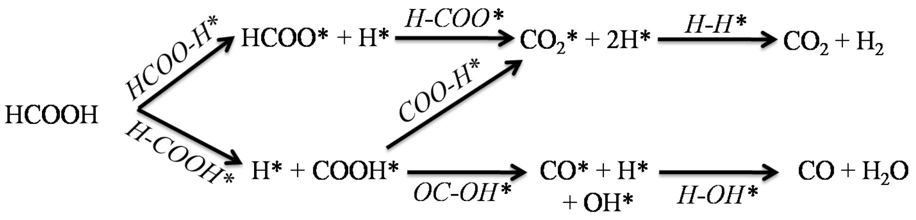

In scheme 1, the mechanism of formic acid decomposition, considered in the present study, has been outlined. We have mainly investigated the two pathways, i.e., formate and carboxyl pathway, for the dissociation reaction which are initiated by activating either O-H or C-H bond of HCOOH to form formate (HCOO*) or carboxyl (COOH*) intermediate, respectively. The further dissociation of HCOO can lead to CO_2 or CO via either C-H bond breaking or simultaneous cleaving of C-H and one of the C-O bonds of HCOO*. In similar way, the CO_2 or CO can be generated through the cleaving of O-H or C-O bonds of COOH intermediate, respectively. In short, there were, in total, four pathways taken into account for HCOOH* decomposition which can produce ($CO_2 + H_2$) (via dehydrogenation pathway) and ($CO + H_2O$) (via dehydration pathway) as products.

Table 7.2: Reaction energy (ΔE) and activation energy barrier (E_a) for the elementary steps on bare $AgPd_{13}$ cluster, graphene supported $AgPd_{13}$ cluster and BN supported $AgPd_{13}$ cluster.

Elementary step	System	E_a (eV)	$\Delta E(eV)$
$HCOOH^* \rightarrow HCOO^* + H^*$	$AgPd_{13}$	0.54	-1.00
	graphene/$AgPd_{13}$	0.20	-1.18
	BN/$AgPd_{13}$ cluster	0.35	-1.26
$HCOO^* \rightarrow CO_2^* + H^*$	$AgPd_{13}$	1.05	0.00
	graphene/$AgPd_{13}$	1.86	-1.00
	BN/$AgPd_{13}$ cluster	0.99	0.09
$HCOOH^* \rightarrow COOH^* + H^*$	$AgPd_{13}$	0.47	-0.66
	graphene/$AgPd_{13}$	0.70	-0.40
	BN/$AgPd_{13}$ cluster	0.37	-1.19
$COOH^* \rightarrow CO_2^* + H^*$	$AgPd_{13}$	0.84	-0.34
	graphene/$AgPd_{13}$	1.00	-0.87
	BN/$AgPd_{13}$ cluster	0.60	-0.40
$COOH^* \rightarrow CO^* + OH^*$	$AgPd_{13}$	0.81	-0.27
	graphene/$AgPd_{13}$	1.36	-0.58
	BN/$AgPd_{13}$ cluster	0.85	-0.16
$H^* + H^* \rightarrow H_2$	$AgPd_{13}$	1.09	1.09
	graphene/$AgPd_{13}$	1.00	1.00
	BN/$AgPd_{13}$ cluster	0.90	0.90
$H^* + OH^* \rightarrow H_2O$	$AgPd_{13}$	0.72	0.23
	graphene/$AgPd_{13}$	0.67	0.38
	BN/$AgPd_{13}$ cluster	0.63	0.56

7.2.2.1 Formate Pathway

As discussed, in formate-mediated pathway, the very first step of dehydrogenation of adsorbed HCOOH* involves breaking of O-H bond which forms HCOO* (HCOOH* → HCOO* + H*). This elementary step is found to be exothermic on all the three present systems. However, as seen in Table 7.2., the reaction energy becomes the most exothermic on BN supported $AgPd_{13}$ system with the value of 1.26 eV. The corresponding activation energy barriers for this step are 0.54 eV, 0.20 eV and 0.35 eV on bare, graphene and BN supported $AgPd_{13}$ cluster, respectively. The computed values suggest that HCOOH* → HCOO* + H* step is quite facile on all the three systems from both kinetic and thermodynamic point of view.

Once the O-H bond is broken, the next possible step is splitting of C-H bond of HCOO* to form CO_2 and H* (HCOO* → CO_2 + H*). This step is found to be thermoneutral on bare $AgPd_{13}$ cluster with 0.0 eV of reaction energy. However, upon addition of graphene as a support of $AgPd_{13}$ cluster, the very same reaction turns exothermic with reaction energy value of 1.00 eV. On the other hand, this step is slightly endothermic by 0.09 eV in the presence of BN supported $AgPd_{13}$ cluster. The considerably high activation energies of 1.05 eV (bare $AgPd_{13}$ cluster), 1.86 eV (graphene supported $AgPd_{13}$ cluster) and 0.99 eV (BN supported $AgPd_{13}$ cluster) for the conversion of HCOO* to (CO_2 + H*) make the elementary step kinetically demanding.

The reason for the difference in energy between the two consecutive elementary steps, HCOOH* → HCOO* + H* and HCOO* → CO_2 + H*, is might be governed by the stabilization of the intermediates on the systems. It is well-known that formic acid is a closed shell species and that is weakly bound to the existent systems (e.g., in the present case, binding energies vary in the range of -0.27 eV to -0.55 eV), whereas, it's decomposition produces strongly bound HCOO* intermediate (binding energies vary in the range of -3.02 eV to -3.34 eV). Hence, from conventional wisdom, it can be easily understood that why formic acid activation to HCOO* is energetically accessible. On the other hand, when the second step is considered, HCOO* → CO_2 + H*, H* is found to be weakly adsorbed with binding energy values lie within -0.50 eV to -0.67 eV. So, HCOO* gets stabilized to a greater degree than H* over the systems studied, leading the dehydrogenation of the former species energetically difficult to occur.

7.2.2.2 Carboxyl Pathway

An alternative route to the formate pathway is carboxyl-mediated pathway, in which the very first step of dehydrogenation of adsorbed HCOOH* has been carried out via C-H bond breaking to form COOH* (HCOOH* → COOH* + H*). The elemenatry step is exothermic on bare, graphene and BN supported $AgPd_{13}$ cluster and the associated reaction energies are 0.66 eV, 0.40 eV and 1.19 eV, respectively. Similar to the former formate-mediated pathway, on BN supported $AgPd_{13}$ cluster, COOH* formation is the most exothermic process with substantial reaction energy of 1.19 eV. This means that conversion of HCOOH* to COOH* thermodynamically most favourable on BN supported $AgPd_{13}$ cluster. Moreover, it also needs the lowest energy of 0.37 eV to overcome the kinetic energy barrier for HCOOH* to COOH* transformation on BN supported $AgPd_{13}$ cluster. However, the barrier height almost gets doubled (0.70 eV) for the same course of the reaction when $AgPd_{13}$ cluster sits over a graphene monolayer. Notably, without any of the supports, i.e., bare $AgPd_{13}$ cluster needs relatively lower activation energy barrier (0.47 eV) than that of with the graphene supported one.

Next, we move towards the step that directs the dissociation of COOH* and as mentioned earlier, that can be bifurcated into two pathways, either via ($COOH^* \rightarrow CO_2 + H^*$) or through ($COOH^* \rightarrow CO^* + OH^*$). The energetics of these two different reaction pathways (Table 7.2) recommend that both the processes are exothermic over all the systems studied. However, it should be noted that in the presence of graphene supported $AgPd_{13}$ cluster, these two decomposition reactions are the most exothermic ones with the reaction energy values of 0.87 eV (for $CO_2 + H^*$) and 0.58 eV (for $CO^* + OH^*$). Subsequently, to check the kinetic feasibility, we calculated the activation energy barriers for the proposed pathways. Decomposition of COOH* turns out to be the energetically most demanding on graphene supported $AgPd_{13}$ cluster with kinetic energy barrier of 1.36 eV for $COOH^* \rightarrow CO^* + OH^*$ and that of 1.00 eV for $COOH^* \rightarrow CO_2 + H^*$. It means that though COOH* dissociation processes were the most exothermic ones on the graphene supported $AgPd_{13}$ cluster but the barrier heights are quite challenging for these reactions to overcome over the similar system. However, compared to the graphene supported $AgPd_{13}$ cluster, the activation energy barriers are lower for both the COOH* dissociation reactions in the presence of the another two systems. For example, in the case of ($COOH^* \rightarrow CO^* + OH^*$), the required energies are 0.81 eV for bare $AgPd_{13}$ cluster and that of 0.85 eV for BN supported $AgPd_{13}$ cluster. Moving to the next option for the dissociation reaction ($COOH^* \rightarrow CO_2 + H^*$), it should be noticed from Table 2 that the bare $AgPd_{13}$ cluster needs almost identical amount of energy (0.84 eV) for the formation of (CO_2 + H*) as in the previous step (COOH* → CO* + OH*). However, interestingly the barrier height gets significantly reduced on BN supported $AgPd_{13}$ cluster and the activation energy value is 0.60 eV which is indeed the lowest value till now for the formation of final product among all the three systems.

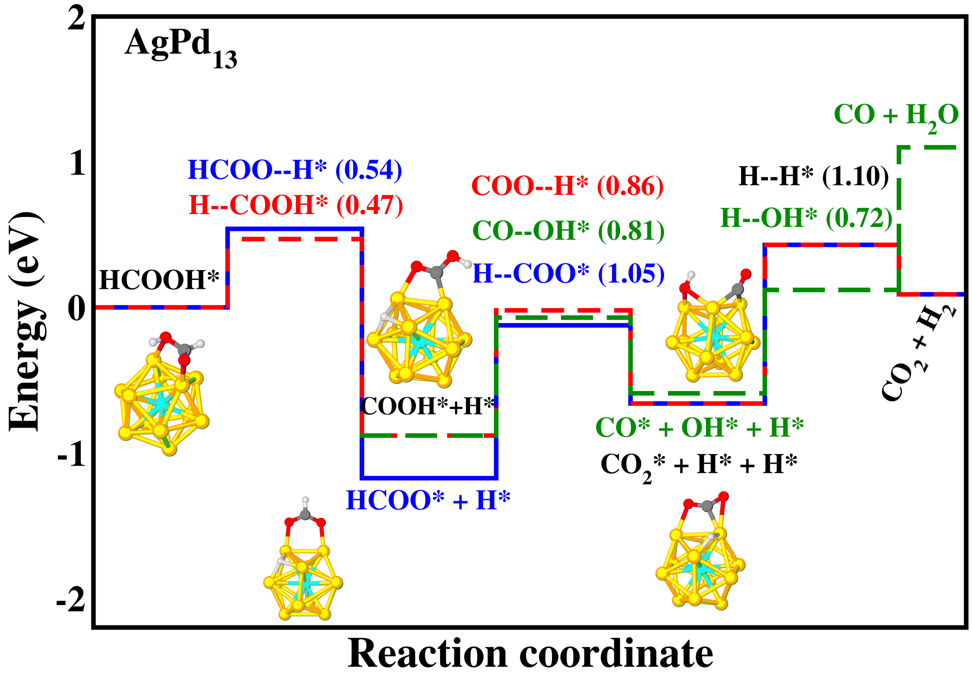

Figure 7.5: Potential Energy Surface for formic acid decomposition on bare $AgPd_{13}$ cluster. The blue solid line corresponds to formate pathway. The carboxyl pathway followed by the formation of CO_2 and CO are represented by red and green dashed line, respectively. Ag, Pd, C, O and H atoms are shown as cyan, yellow, grey, red and white color, respectively.

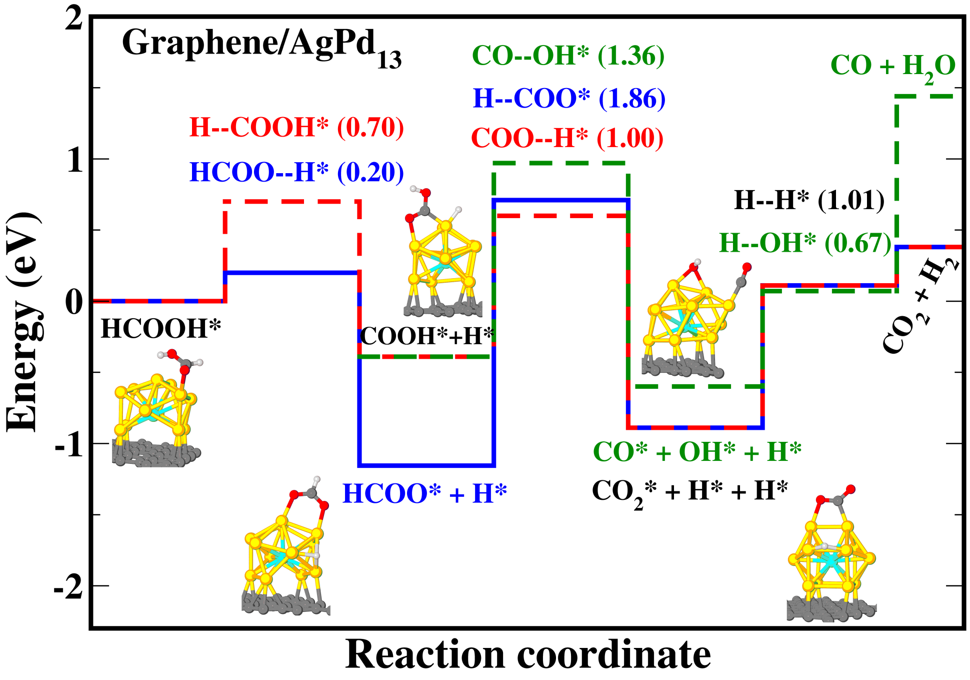

Figure 7.6: Potential Energy Surface for formic acid decomposition on graphene supported $AgPd_{13}$ cluster. The blue solid line corresponds to formate pathway. The carboxyl pathway followed by the formation of CO_2 and CO are represented by red and green dashed line, respectively. Ag, Pd, C, O and H atoms are shown as cyan, yellow, grey, red and white respectively.

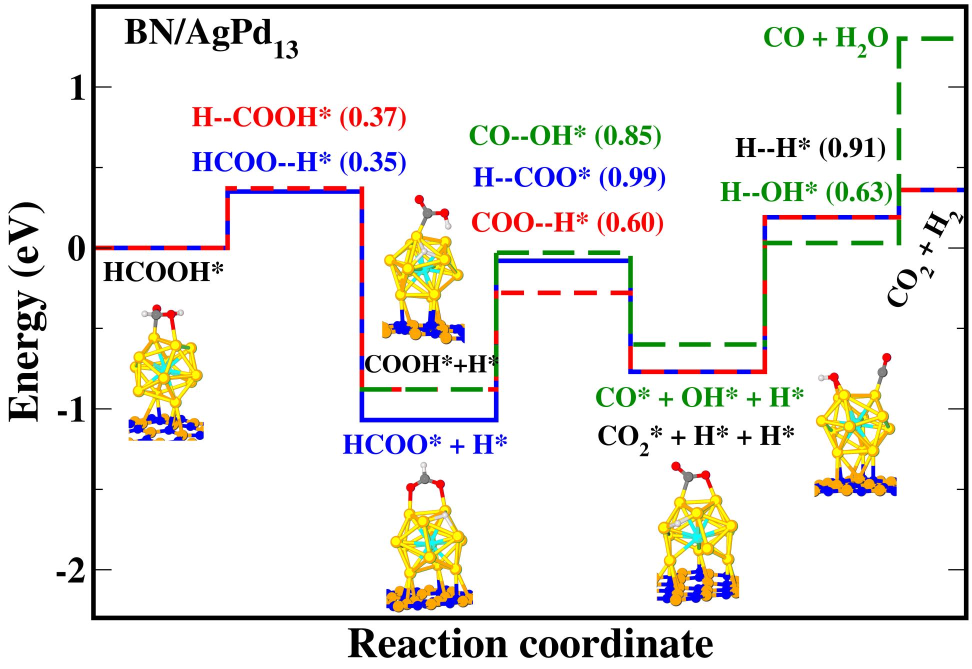

Figure 7.7: Potential Energy Surface for formic acid decomposition on BN supported $AgPd_{13}$ cluster. The blue solid line corresponds to formate pathway. The carboxyl pathway followed by the formation of CO_2 and CO are represented by red and green dashed line, respectively. Ag, Pd, B, N, C, O and H atoms are shown as cyan, yellow, orange, blue, grey, red and white respectively.

The complete potential energy surface for the corresponding reaction have been shown in Figure 7.5, 7.6 and 7.8 for bare $AgPd_{13}$ cluster, graphene supported $AgPd_{13}$ cluster and BN supported $AgPd_{13}$ cluster. Based on the all of the computed energies, it can be deduced that the binding energy of HCOO* is evidently higher than that of COOH* on all the three studied system. However, formation of HCOO* and COOH* from HCOOH* dissociation are quite comparable on bare and BN supported $AgPd_{13}$ cluster in terms of energy barriers, whereas on graphene supported $AgPd_{13}$ cluster, the formation of HCOO* is easier than COOH* with the difference in activation energy barrier of 0.50 eV. Further decomposition of HCOO* is energetically more difficult in compared to COOH* for all the considered systems. This suggests that though HCOO* might not be the intermediate on the active pathway to the dehydrogenation, but, rather it may play the role of spectator species which occupy a large portion of catalytic surface. This might explain the experimental observation of formate accumulation on the surface. However, among all the systems, BN supported $AgPd_{13}$ cluster demands relatively lower energy barrier of 0.99 eV for the dehydrogenation of HCOO* to CO_2. The alternative route, i.e., dissociation of COOH*, can lead to two different products, CO_2 and as well as CO. On bare $AgPd_{13}$ cluster, formation of both the products might be equally probable since the activation energy barriers needed for the associated conversions are almost identical. However, on the graphene supported $AgPd_{13}$ cluster, it is difficult to proceed to form both CO_2 and CO through COOH* dissociation owing to have very high barrier height. However, between these two processes, CO_2 formation is favoured over CO since the former requires less energy barrier (by 0.36 eV). On BN supported $AgPd_{13}$ cluster, it has been found that CO_2 production is preferred to CO. In fact, in the present study, BN monolayer can be regarded as the most suitable support of $AgPd_{13}$ cluster for the complete conversion of $HCOOH^* \rightarrow CO_2 + 2H^*$ with considerably favourable reaction energies and activation energy barriers which directly influences the thermodynamics and kinetics of the overall process. Scheme 2. details the complete reaction, ($HCOOH^* \rightarrow CO_2 + 2H^*$) over BN supported $AgPd_{13}$ cluster with computed reaction energies and activation energy barriers.

Scheme 2: The Reaction Mechanism of Formic Acid Decomposition on BN supported $AgPd_{13}$ cluster. The values in italics and parentheses are the corresponding activation energy barriers and reaction energies for the corresponding reaction steps.

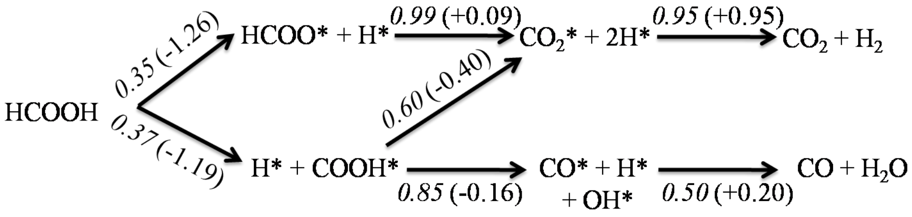

7.2.3 Conclusion

Periodic, self-consistent, density functional theory calculations have been performed to explore HCOOH decomposition reaction on bare, graphene and BN supported $AgPd_{13}$ cluster through formate and carboxyl intermediates. The probable elementary reaction steps and the associated reaction energetics and kinetics have been thoroughly investigated. We find that the HCOO* formation is almost comparable to COOH* formation on bare and BN supported $AgPd_{13}$ cluster; however the same is not true for graphene supported $AgPd_{13}$ cluster where HCOO* formation is preferred over COOH*. For the second dehydrogenation step, it has been found that, for all the cases, dehydrogenation of HCOO* needs high activation energy barrier and that is kinetically precluded. Similarly, both the dehydrogenation and dehydration processes of COOH* are hindered by the large barrier height on graphene supported $AgPd_{13}$ cluster. In comparison, bare and graphene supported $AgPd_{13}$ cluster needs lower amount of energy to form both the dehydrated as well as dehydrogenated products. However, though bare $AgPd_{13}$ cluster needs identical amount of energy for the two dissociation pathways of COOH*, dehydrogenation reaction can be selected to be better in comparison to dehydration path over BN supported $AgPd_{13}$ cluster. In conclusion, our study prescribes that BN supported $AgPd_{13}$ cluster is probably the most effective catalyst amongst all, which follows dehydrogenation mechanism and needs considerably lower activation energy barriers throughout the course of the reaction. The most important finding of this study is the fact that identical $AgPd_{13}$ cluster on different supports leads to different activities for HCOOH decomposition. This clearly demonstrates that there is a strong influence of the metal-support interaction on the catalytic properties. In short, our work suggests that the complete reaction pathway, feasibility of intermediate or product formation is highly dominated by the support of the catalyst.

Bibliography

[1] L. Dietz, S. Piccinin and M. Maestri, *The Journal of Physical Chemistry C*, 2015, **119**, 4959–4966.

[2] M. Aresta and A. Dibenedetto, *Dalton Trans.*, 2007, 2975–2992.

[3] S. Enthaler, J. von Langermann and T. Schmidt, *Energy Environ. Sci.*, 2010, **3**, 1207–1217.

[4] M. Grasemann and G. Laurenczy, *Energy Environ. Sci.*, 2012, **5**, 8171–8181.

[5] F. Jo, *ChemSusChem*, 2008, **1**, 805–808.

[6] P. G. Jessop, T. Ikariya and R. Noyori, *Nature*, 1994, 231–233.

---

[7] L. C. Grabow, A. A. Gokhale, S. T. Evans, J. A. Dumesic, and M. Mavrikakis*, *The Journal of Physical Chemistry C*, 2008, **112**, 4608–4617.

[8] A. A. Gokhale, J. A. Dumesic, and M. Mavrikakis*, *Journal of the American Chemical Society*, 2008, **130**, 1402–1414.

[9] E. Vesselli, L. D. Rogatis, X. Ding, A. Baraldi, L. Savio, L. Vattuone, M. Rocca, P. Fornasiero, M. Peressi, A. Baldereschi, R. Rosei and G. Comelli, *Journal of the American Chemical Society*, 2008, **130**, 11417–11422.

[10] G. Peng, S. J. Sibener, G. C. Schatz, S. T. Ceyer and M. Mavrikakis, *The Journal of Physical Chemistry C*, 2012, **116**, 3001–3006.

[11] G. Peng, S. Sibener, G. C. Schatz and M. Mavrikakis, *Surface Science*, 2012, **606**, 1050 – 1055.

[12] P. Giannozzi, S. Baroni, N. Bonini, M. Calandra, R. Car, C. Cavazzoni, D. Ceresoli, G. L. Chiarotti, M. Cococcioni, I. Dabo, A. Dal Corso, S. de Gironcoli, S. Fabris, G. Fratesi, R. Gebauer, U. Gerstmann, C. Gougoussis, A. Kokalj, M. Lazzeri, L. Martin-Samos, N. Marzari, F. Mauri, R. Mazzarello, S. Paolini, A. Pasquarello, L. Paulatto, C. Sbraccia, S. Scandolo, G. Sclauzero, A. P. Seitsonen, A. Smogunov, P. Umari and R. M. Wentzcovitch, *Journal of Physics: Condensed Matter*, 2009, **21**, 395502 (19pp).

[13] J. P. Perdew, K. Burke and M. Ernzerhof, *Phys. Rev. Lett.*, 1996, **77**, 3865–3868.

[14] H. J. Monkhorst and J. D. Pack, *Phys. Rev. B*, 1976, **13**, 5188–5192.

[15] G. Henkelman, B. P. Uberuaga and H. Jonsson, *J. Chem. Phys.*, 2000, **113**, 9901–9904.

[16] M. J. Lakin, D. Troya, G. C. Schatz and L. B. Harding, *The Journal of Chemical Physics*, 2003, **119**, 5848–5859.

[17] J. A. Turner, *Science*, 2004, **305**, 972–974.

[18] A. Boddien, F. Grtner, C. Federsel, P. Sponholz, D. Mellmann, R. Jackstell, H. Junge and M. Beller, *Angewandte Chemie International Edition*, 2011, **50**, 6411–6414.

[19] M. Felderhoff, C. Weidenthaler, R. von Helmolt and U. Eberle, *Phys. Chem. Chem. Phys.*, 2007, **9**, 2643–2653.

[20] D. A. Bulushev, S. Beloshapkin and J. R. Ross, *Catalysis Today*, 2010, **154**, 7 – 12.

[21] F. Solymosi, . Kos, N. Liliom and I. Ugrai, *Journal of Catalysis*, 2011, **279**, 213 – 219.

[22] J. A. Herron, J. Scaranto, P. Ferrin, S. Li and M. Mavrikakis, *ACS Catalysis*, 2014, **4**, 4434–4445.

[23] J. S. Yoo, F. Abild-Pedersen, J. K. Nrskov and F. Studt, *ACS Catalysis*, 2014, **4**, 1226–1233.

[24] X. Zhou, Y. Huang, W. Xing, C. Liu, J. Liao and T. Lu, *Chem. Commun.*, 2008, 3540–3542.

[25] K. Mori, M. Dojo and H. Yamashita, *ACS Catalysis*, 2013, **3**, 1114–1119.

[26] Y. Ping, J.-M. Yan, Z.-L. Wang, H.-L. Wang and Q. Jiang, *J. Mater. Chem. A*, 2013, **1**, 12188–12191.

[27] S. Zhang, . Metin, D. Su and S. Sun, *Angewandte Chemie International Edition*, 2013, **52**, 3681–3684.

[28] M. Hattori, H. Einaga, T. Daio and M. Tsuji, *J. Mater. Chem. A*, 2015, **3**, 4453–4461.

[29] F. Solymosi and A. Erdhelyi, *Journal of Catalysis*, 1985, **91**, 327 – 337.

[30] A. Gazsi, T. Bnsgi and F. Solymosi, *The Journal of Physical Chemistry C*, 2011, **115**, 15459–15466.

[31] D. A. Bulushev, M. Zacharska, E. V. Shlyakhova, A. L. Chuvilin, Y. Guo, S. Beloshapkin, A. V. Okotrub and L. G. Bulusheva, *ACS Catalysis*, 2016, **6**, 681–691.

[32] J. P. Perdew, J. A. Chevary, S. H. Vosko, K. A. Jackson, M. R. Pederson, D. J. Singh and C. Fiolhais, *Phys. Rev. B*, 1992, **46**, 6671–6687.